

# **Seismic Energy Propagation in Highly Scattering Environments and Constraints on Lunar Interior Structure from the Scattered Signals of the Apollo Passive Seismic Experiment**

by

Jean-François Blanchette-Guertin

B.Sc., The University of British Columbia, 2008

A THESIS SUBMITTED IN PARTIAL FULFILLMENT OF  
THE REQUIREMENTS FOR THE DEGREE OF

DOCTOR OF PHILOSOPHY

in

The Faculty of Graduate and Postdoctoral Studies

(Geophysics)

THE UNIVERSITY OF BRITISH COLUMBIA

(Vancouver)

August 2014

© Jean-François Blanchette-Guertin 2014

# Abstract

Meteoroid impacts over hundreds of millions to billions of years can produce a highly fractured and heterogeneous megaregolith layer on planetary bodies such as the Moon that lack effective surface recycling mechanisms. The energy from seismic events occurring on these bodies undergoes scattering in the fractured layer(s) and this process generates extensive coda wave trains that follow major seismic wave arrivals. These long coda trains can obscure the secondary crustal, mantle or core phases that are often crucial in assessing the interior structure of these planetary bodies when using more traditional seismological analyses. However, the decay properties of these codas are affected by the interior velocity, intrinsic attenuation and scattering structure of the planet or moon. As such, these decay properties can contain valuable information regarding these aspects of interior structure. This thesis provides the first systematic analysis of scattering in the Apollo Passive Seismic Experiment dataset, demonstrating that scattering in the Moon occurs over a wide range of frequencies, and dominantly in the near-surface megaregolith that comprises many more small scale heterogeneities than large ones. I also present a new numerical modeling technique (referred to as PHONON1D) that models seismic energy propagation and integrates high levels of scattering. Using this method, I investigate the effects of various velocity, scattering and intrinsic attenuation structures on the scattered coda. Results show that the main controls on the coda generation and decay times are the seismic velocity profile, attenuation levels, and the number density of scatterers. Thus these properties can be assessed by comparing predicted synthetic seismic coda with those observed in the Apollo Passive Seismic Experiment data. Finally, I use the PHONON1D method to show that locations within young and large impact basins, away from the edges, have the potential to minimize the scattering observed in the recorded seismic signals. These locations would be ideal for the emplacement of future seismic surveys on the lunar surface.

# Preface

This thesis comprises four complementary studies that have been prepared to be individually published in peer-reviewed scientific journals. Consequently, some background information is repeated in the introductory sections of each chapter.

A version of Chapter 2<sup>1</sup> is published in *Journal of Geophysical Research – Planets* [Blanchette-Guertin et al., 2012]. The co-authors are Jean-François Blanchette-Guertin, Catherine L. Johnson, and Jesse F. Lawrence. I was the lead investigator for this study, responsible for all data selection and analysis, as well as for the majority of the manuscript composition. Both Catherine Johnson and Jesse Lawrence provided extensive feedback for the data analysis method and interpretations, as well as invaluable editorial comments for all drafts prior to publication.

A version of Chapter 3 is in revision for publication in a major geophysical research journal. The co-authors are Jean-François Blanchette-Guertin (first author), Catherine L. Johnson, and Jesse F. Lawrence. The modified phonon method used in this study is a refinement and extension of a similar method presented in Shearer and Earle [2004]. Jesse Lawrence provided me with the basic FORTRAN code, which I have extensively improved and modified to implement isotropic scattering, user-defined scatterer scale-lengths distribution, as well as frequency-dependent and phase-dependent intrinsic attenuation. I am also responsible for the code benchmarking, for the model selections, for the data analysis, as well as for the majority of the manuscript composition. Jesse Lawrence provided support for the code modifications as well as feedback and comments during the data analysis and writing stages. Catherine Johnson provided continuous support for the code modifications and data analysis as well as editorial comments on all drafts before submission. All computations of the synthetic seismograms were performed on the

---

<sup>1</sup>Reprinted from *Journal of Geophysical Research – Planets*, ©2012, with permission from John Wiley and Sons.

## *Preface*

---

CEES HPC facility at Stanford University, for which access was provided by Jesse Lawrence. All post-processing and analysis of the synthetics was done in-house at UBC.

A version of Chapter 4 will be submitted to a major geophysical research journal. The co-authors are Jean-François Blanchette-Guertin (first author), Catherine L. Johnson, and Jesse F. Lawrence. I selected the models and ran the analyses, and I am responsible for most of the manuscript. Catherine Johnson and Jesse Lawrence provided insightful comments and feedback during the data analysis and interpretation stages, as well as editorial comments for the manuscript.

A version of Chapter 5 is ready for submission to a major geophysical research journal. The co-authors are Jean-François Blanchette-Guertin (first author), Catherine L. Johnson, and Jesse F. Lawrence. I am responsible for the code development, the analyses and for writing most of the manuscript. Catherine Johnson and Jesse Lawrence provided feedback and editorial comments for all drafts prior to submission.

# Table of Contents

<b>Abstract</b> . . . . .	ii
<b>Preface</b> . . . . .	iii
<b>Table of Contents</b> . . . . .	v
<b>List of Tables</b> . . . . .	viii
<b>List of Figures</b> . . . . .	ix
<b>Acknowledgements</b> . . . . .	xi
<b>Dedication</b> . . . . .	xiii
<b>1 Introduction</b> . . . . .	1
1.1 Motivation . . . . .	1
1.2 Scientific Context and Background . . . . .	6
1.3 Thesis Structure . . . . .	13
<b>2 Investigation of Scattering in Lunar Seismic Coda</b> . . . . .	16
2.1 Introduction . . . . .	16
2.2 Data . . . . .	21
2.3 Methodology . . . . .	21
2.3.1 Data Processing Steps . . . . .	21
2.3.2 Analytical Solutions for the Coda Decay . . . . .	24
2.4 Results . . . . .	27
2.4.1 Decay Parameters Measured on the Long-Period Channels (LP) . . . . .	29

---

*Table of Contents*

---

2.4.2	Decay Parameters Measured on the Short-Period Channel (SPZ) . . . . .	34
2.4.3	Dependence of Decay Parameters on $\alpha$ . . . . .	37
2.5	Implications . . . . .	37
2.5.1	Shallow Events (SMQ, NI and AI) . . . . .	40
2.5.2	Deep Moonquakes . . . . .	46
2.6	Conclusions . . . . .	48
<b>3</b>	<b>Modeling Seismic Energy Propagation in Highly Scattering Environments</b> . . . . .	51
3.1	Introduction . . . . .	51
3.2	Methodology . . . . .	54
3.2.1	Model Geometry . . . . .	55
3.2.2	Velocity Profiles . . . . .	57
3.2.3	Seismic Source . . . . .	59
3.2.4	Scattering Layers . . . . .	60
3.2.5	Regular Velocity Interfaces . . . . .	62
3.2.6	Surface Recorders . . . . .	64
3.2.7	Intrinsic Attenuation . . . . .	66
3.3	Modeling Method Benchmarking . . . . .	66
3.4	Modeling Approach . . . . .	67
3.4.1	Processing of Synthetics . . . . .	71
3.5	Results and Discussion . . . . .	73
3.5.1	Two Distinct Decay Regimes . . . . .	76
3.5.2	Effects of Interior Structure on Coda Decay Times . . . . .	82
3.6	Conclusions . . . . .	90
<b>4</b>	<b>Constraints on Lunar Interior Structure from the Scattered Signals of the Apollo Passive Seismic Experiment</b> . . . . .	93
4.1	Introduction . . . . .	93
4.2	Apollo Passive Seismic Experiment Data . . . . .	95
4.3	Methodology . . . . .	97
4.3.1	Modeling Ambient Noise and APSE Instrument Effects .	101

---

*Table of Contents*

---

4.3.2	Analysis of Synthetic Seismograms . . . . .	104
4.4	Results . . . . .	106
4.4.1	Results from Modeling of Seismic Noise and APSE-Instrument Effects . . . . .	106
4.4.2	Modeling Results . . . . .	107
4.5	Discussion . . . . .	109
4.6	Conclusions . . . . .	112
<b>5</b>	<b>Effects of Lateral Variations in Megaregolith Thickness on Recorded Seismic Signals . . . . .</b>	<b>114</b>
5.1	Introduction . . . . .	114
5.2	Methodology . . . . .	116
5.3	Results . . . . .	116
5.4	Discussion and Conclusions . . . . .	120
<b>6</b>	<b>Conclusions . . . . .</b>	<b>123</b>
6.1	Summary . . . . .	124
6.2	The Science Questions Answered . . . . .	126
6.3	Future Work . . . . .	127
<b>Bibliography</b>	. . . . .	<b>130</b>

**Appendix**

<b>A</b>	<b>Coefficients for Solid-Solid, Free Surface and Solid-Liquid Interfaces</b>	<b>140</b>
A.1	P-SV at Free Surface . . . . .	140
A.2	Solid-Solid Interfaces . . . . .	142
A.3	Solid-Liquid Interfaces . . . . .	143

# List of Tables

2.1	Occurrence time and location of events used in Chapter 2’s study . . . . .	19
2.2	Frequency bands investigated in Chapter 2’s analysis . . . . .	24
2.3	Decay least-squares fits results . . . . .	30
3.1	Models investigated in Chapter 3’s study . . . . .	70
4.1	Decay least-squares fits results from APSE data . . . . .	96
4.2	Models investigated in Chapter 4’s study . . . . .	98
4.3	Median epicentral distances and signal-to-noise ratios measured on the APSE signals . . . . .	102

# List of Figures

1.1	Lunar internal structure . . . . .	2
1.2	Lateral variations in crustal thickness . . . . .	3
1.3	Lunar vs. terrestrial seismic signals . . . . .	4
1.4	Map showing the locations of the four APSE receivers . . . . .	7
1.5	Examples of lunar seismic signals . . . . .	8
1.6	Schematic diagram of the APSE unit . . . . .	9
1.7	Schematic cross-section of the megaregolith . . . . .	11
2.1	Map showing the locations of the APSE stations and the epicenters of seismic events used in this work . . . . .	18
2.2	Instrument response and frequency response curves of bandpass filters used in the analysis . . . . .	22
2.3	APSE Data processing steps . . . . .	26
2.4	Natural impact and shallow moonquake S-rise times for the long period bands . . . . .	28
2.5	Measured $\tau_d$ for all types of events on the LP channels . . . . .	31
2.6	Measured $Q_c$ for all types of events on the LP channels . . . . .	32
2.7	Measured $\tau_d$ for all types of events on the SPZ channel . . . . .	35
2.8	Measured $Q_c$ for all types of events on the SPZ channel . . . . .	36
2.9	Comparison between terrestrial and lunar $Q_c^{-1}$ values . . . . .	38
2.10	Schematic representation of seismic energy propagation showing the effect of epicentral distance on $\tau_d$ . . . . .	41
2.11	Schematic representation of seismic energy propagation in the scattering layer . . . . .	44
2.12	$\tau_d$ and $Q_c$ values for DMQ events in the A001 source region . . .	47

---

*List of Figures*

---

3.1	Model geometry 1-D . . . . .	56
3.2	Model geometry 2-D . . . . .	58
3.3	Source functions used in the PHONON1D modeling . . . . .	60
3.4	Scatterer length-scale probability distribution . . . . .	61
3.5	Scattered ray path example . . . . .	63
3.6	Time correction applied to phonons that do not hit the surface directly beneath the receivers . . . . .	65
3.7	Model benchmarking . . . . .	68
3.8	1-D velocity and density profiles used in this study . . . . .	72
3.9	$Q_i(f)$ styles used in the modeling work . . . . .	73
3.10	Examples of synthetic traces for all models presented in this study	75
3.11	Decay times as a function of epicentral distances for selected models	77
3.12	Regime 1 vs. Regime 2 . . . . .	79
3.13	Average $\tau_d$ , maximum S-coda amplitudes and $Q_c$ values for Regimes 1 and 2 . . . . .	81
3.14	Average $\tau_d$ values for each models and frequency bands, for surface impacts and deep events . . . . .	83
3.15	Effect of $Q_i(f)$ on $\tau_d$ and $Q_c(f)$ . . . . .	88
4.1	$Q_i(z)$ styles used in this modeling work . . . . .	99
4.2	$Q_i(f)$ styles used in this modeling work . . . . .	100
4.3	APSE instrument effect implementation steps . . . . .	103
4.4	Examples of summary $\tau_d$ measurements . . . . .	105
4.5	Comparison between noise-free and APSE-corrected synthetic signals . . . . .	107
4.6	Median $\tau_d$ values on the LP bands . . . . .	108
4.7	Intercepts and slopes on the SP bands . . . . .	110
5.1	Synthetic seismograms: Impact versus deep event in small basins .	118
5.2	Synthetic seismograms: Thick megaregolith and large basins . .	119
A.1	Notations used in the transmission and reflection coefficient equations. . . . .	141

# Acknowledgements

As it turns out, completing a PhD thesis is quite the endeavour. And as it also turns out, it would not have been as fruitful, or even sometimes as enjoyable, without the support (technical, professional, moral or otherwise) of many, many people. The list below is far from exhaustive. So to those of you I do not mention, but with whom I have crossed paths during these past few years of graduate school, please know that you also bask in the warm glow of my sincere gratitude.

So, in no specific order, and first in French:

Un merci tout absolument spécial à ma famille: Mariève, Amélie, Alexandra, Danièle, Michel, Michèle, Micheline, Gaston et Ellen (ainsi que les beaux-frères et les neveux!). Ce qui ne devait être que quatre ans à Vancouver est subtilement devenu un séjour de près de dix ans. Votre support continu et sans équivoque pendant les bons et moins bons moments de ma carrière universitaire m'ont permis de naviguer dans les eaux parfois tumultueuses de ces dernières années. Je vous aime.

Philippe, Gabrièle et Laurence. Tout d'abord, vous êtes beau, belles et magnifiques! Votre amitié m'a aidé à conserver les pieds fortement ancrés et la tête bien haute, et ce, même à plus de 5000 km de distance. Merci. Je vous aime, aussi.

To my current and past Vancouver family: Ariel, Carolina, Gina, Shelley, Jenn, Marianne, Holly, Ayesha, Lush, Jon, Hannah, Geoff, Nicola, A.J., Farley, and of course Lilu, to only name a few. Thank you a thousand times. You have made these past few years a bundle of unforgettable memories. Love, always.

To the UBC crew: Jenn Fohring, Marianne Haseloff, Reka Winslow, Kathi Unglert, Shelley Oliver, Ayesha Ahmed, Kirsten Halverson, Lucy Porritt, Leanne Smar, Shawn Hood, Claire Poulton, Vicky Liu, Andreas Ritzer, Hideharu Uno, Surdas Mohit, among many others. Thank you for sharing this experience and for making it that much better through your support, friendship, or otherwise. A

## Acknowledgements

---

special thank you to Reka for being my partner in academic crime for a few years. I admire your strong analytical mind, professional work ethics, and unfaltering perseverance. I am looking forward to the day our paths will cross again and when we will both work on the same fun and fantastic planetary exploration mission.

To the members of my committee: Michael Bostock, Jesse Lawrence and Mark Jellinek. Michael, I really appreciate you humouring my surprise office calls and all your help with my often unclear and poorly constructed questions. Your help and experience proved invaluable at many steps during this project. Jesse, first of all, many thanks to you and your most fabulous family for hosting me on my many visits to Stanford. Your down-to-earth and genial approach to life made these trips of course useful, but mostly fun. Also, thank you for ALL your support, comments, advice, and for the few motivational (for me!) discussions we had throughout this PhD. I am grateful for the circumstances that made us work together on this project. Mark, I cannot thank you enough for your help, analytical acumen, and knowledge of what seems to be all things. Our discussions forced me to think about new and better things, and for that I am grateful. You bring a breath of fresh air to science! I remember a time before I even started this thesis when you told me in a very serious voice that everyone going through the PhD process leaves it a different person. I had doubts then, I believe you now.

And of course, my thesis advisor, Catherine Johnson.

Catherine, you have been witness to quite the wide range of professional and personal struggles, during which you have always made your full support clear. I will always be extremely grateful for that support, for your academic mentorship, for your ever apparent faith in my abilities, for your unfailing professionalism, and, most of all, for your *ferocious* and highly contagious passion for all things science. Passion without which I would most assuredly be on a drastically different career path today. (Absolutely) No regrets! I could expand on this for a long while, but you know me well enough by now to know what I am trying to convey with this simple thank you. Catherine, Merci.

Finally, this work was generously funded by the Natural Sciences and Engineering Research Council of Canada, a University of British Columbia PhD Four-Year Fellowship, a Lorntzsen Scholarship, the department of Earth, Ocean and Atmospheric Sciences and by the Faculty of Science.

Pour Danièle.

• • •

# Chapter 1

## Introduction

### 1.1 Motivation

The Moon is the only Solar System object, other than the Earth (and the Sun, if one considers helioseismology), for which we have seismic data. The four seismometers installed at the start of the Apollo Passive Seismic Experiment (APSE, 1969-1977) returned over seven years of continuous seismic recordings. More than 40 years of analyses of the APSE data have yielded important discoveries regarding the inner structure and properties of the Moon. These include a better understanding of interior seismic velocities to depths of  $\sim$ 1000 km (e.g., Nakamura [1983]; Lognonné et al. [2003]; Gagnepain-Beyneix et al. [2006]; Garcia et al. [2011]), as well as constraints (albeit limited ones) on the depths of the major compositional layers forming the Moon’s interior (e.g., Vinnik et al. [2001]; Weber et al. [2011]). A series of orbital missions and earth-based radar studies have also provided us with a more extensive knowledge of surface topography (e.g., Smith et al. [2010]), lateral variations in relief at the crust-mantle interface (e.g., Wieczorek et al. [2013]), crustal composition (e.g., Jolliff et al. [2000]; Klima et al. [2011]), and other geophysical properties such as crustal magnetic anomalies (e.g., Hood et al. [2001]). The resulting understanding of the first order interior structure of the Moon is shown in Figures 1.1 and 1.2. The presence of a small metallic lunar core is supported by gravity, seismic and magnetic studies. Volumetrically the Moon is dominated by the silicate mantle and crustal rocks (Figure 1.1). The current best-estimate for the globally-averaged crustal thickness is about 40 km [Khan and Mosegaard, 2002; Lognonné et al., 2003; Gagnepain-Beyneix et al., 2006; Wieczorek et al., 2013], however crustal thickness varies geographically as seen in Figure 1.2.

Four different types of seismic events were identified in the APSE data: arti-

### 1.1. Motivation

---

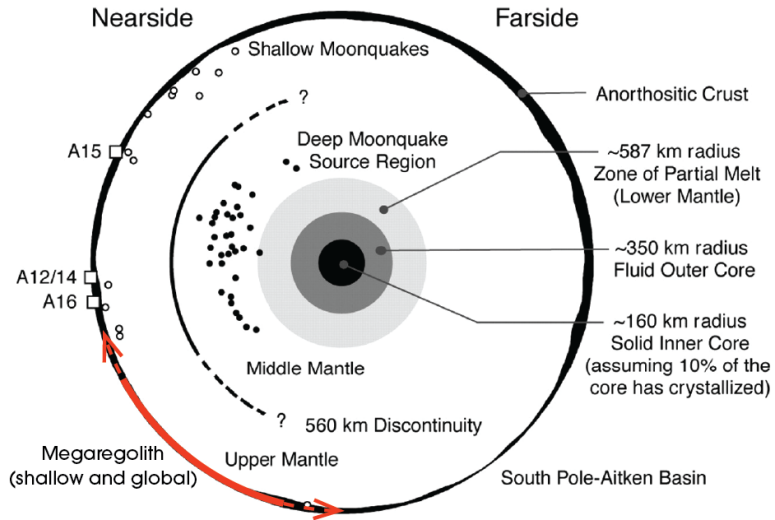


Figure 1.1: Cross-section of the lunar interior showing the main compositional layering and the approximate depths of tectonic sources. Schematic is modified from Wieczorek [2009], with permission from the *Mineralogical Society of America*.

ficial impacts, natural impacts, deep moonquakes and shallow moonquakes. The signals are atypical of the majority of events recorded daily on Earth, suggesting inherently different properties of the lunar and terrestrial interiors. Some of the characteristics of the lunar seismograms are: long durations ( $\sim 60$  minutes or more), low amplitudes, lack of identifiable secondary wave arrivals, gradual build up of energy from the onset of the events, and a slow amplitude decay from the maximum amplitude to the end of the event (when the signal amplitude reaches the background noise level, see Figure 1.3). These aspects of the lunar seismic recordings, combined with the low number of stations and the APSE network poor geographical coverage (Figure 1.4), mean that some well-established seismic data analysis techniques used routinely in terrestrial studies cannot be easily applied to the lunar data set. For example, the locations of moonquakes typically have an uncertainty of  $>100$  km (e.g., Nakamura et al. [1979]; Lognonné et al. [2003]), which is an order of magnitude or more larger than typical uncertainties of terrestrial teleseismic events.

A long-standing proposed explanation for the unusual characteristics of the

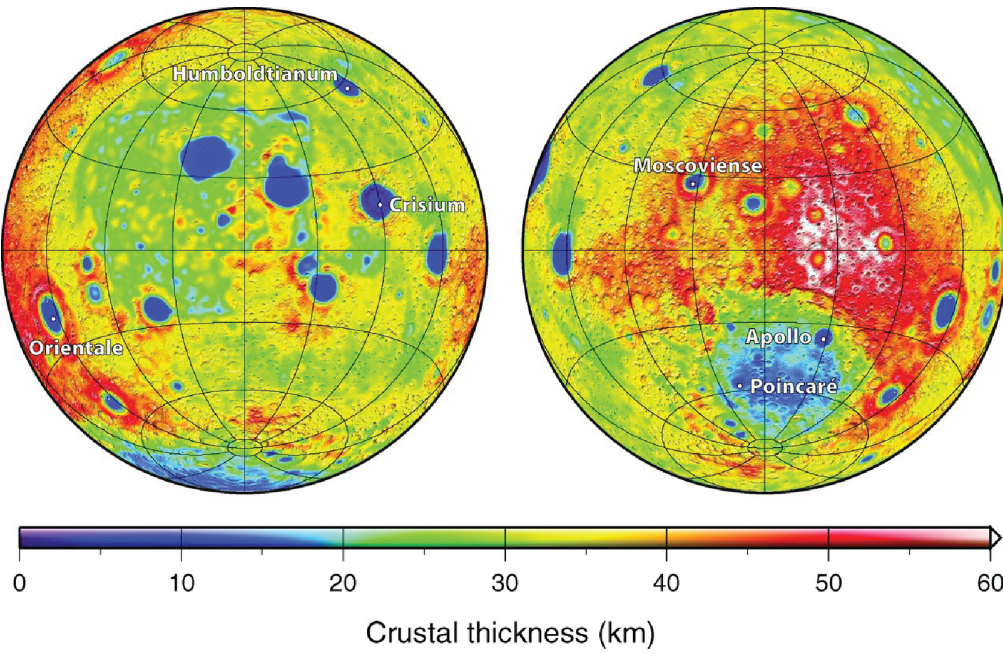


Figure 1.2: Lateral variation in lunar crustal thickness derived from the Gravity Recovery and Interior Laboratory (GRAIL) and Lunar Reconnaissance Orbiter (LRO) data. Figure is reprinted from Wieczorek et al. [2013], with permission from *Science*.

### 1.1. Motivation

---

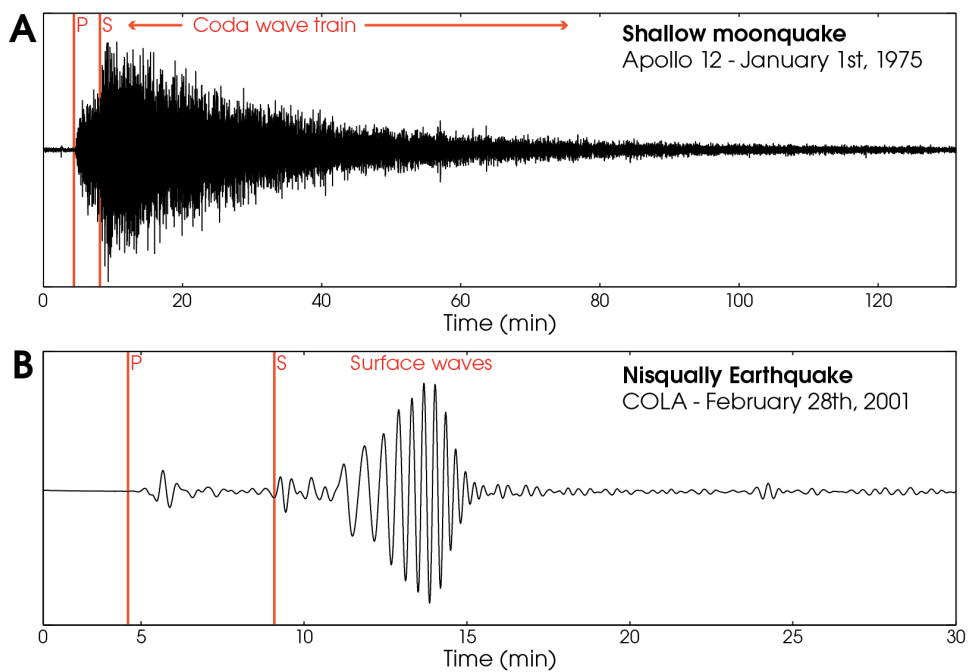


Figure 1.3: Lunar moonquake signal (A) and typical terrestrial signal (B), showing the main wave arrivals in red. Note the different scales for the time axes. The shallow moonquake signal shows the very long duration, emergent body wave arrivals, and very long decaying coda train that are typical of lunar seismic signals.

### *1.1. Motivation*

---

APSE data is that the seismic energy propagates in a highly scattering layer characterized by a very low intrinsic attenuation [Nakamura, 1977; Latham et al., 1970a]. This scattering layer is thought to comprise the very fine-grained surface regolith layer and the underlying highly fractured layer known as the megaregolith [Hörz, 1991]. Because the Moon has no surface recycling mechanism (e.g., plate tectonics), these layers are global and may extend to depths of several tens of km. The small- to large-scale heterogeneities in these layers cause coherent wave fronts to randomly spread in a process known as seismic scattering. The concentration and size distribution of the scatterers will control the intensity of the scattering and the frequencies that are affected. The lunar seismic data exhibit intense scattering over the whole range of recorded frequencies (approximately 0.25 to 10 Hz).

Although scattering has been inferred to be the cause of the long lunar seismic coda, a systematic study of these signals was never undertaken, and so a potentially important resource for understanding the structure of the near-surface megaregolith layer, as well as the interior structure of the Moon, has hitherto never been explored fully. The main goal of my research has been to investigate the scattering and attenuation structure of the Moon and to build understanding of the processes governing the transmission of seismic energy in highly scattering environments through modeling. The general questions I aim to address with this research work are:

- Q1:** What constraints on the interior structure of the Moon or of other highly scattering bodies can we infer from analyzing the scattered coda of recorded seismic signals?
- Q2:** What are the effects of seismic velocity, intrinsic attenuation and scattering structures on the scattered coda of seismic signals?
- Q3:** Are there locations on the lunar surface that could minimize the intensity of scattering in recorded signals, and maximize science returns of future seismic surveys?

To answer these questions, I have first analyzed the scattering properties of the Apollo Passive Seismic Experiment data to gain insight into the first-order scattering and attenuation structures of the Moon. However, the interpretations from this study were limited by the lack of understanding of how seismic energy propagates

## *1.2. Scientific Context and Background*

---

in highly scattering environments. To address this, a major part of my research work has been to develop a new synthetic seismogram modeling capability that can incorporate the types of scattering expected on planets and moons with highly fractured megaregolith layers. Using this method, I have investigated the effects of several scattering and intrinsic attenuation structures on the coda of scattered signals. I have also used this new method, together with the data constraints provided by the initial study, to identify a suite of lunar interior models that reproduce the scattered characteristics observed in the APSE dataset.

As well as shedding light on the scattering structure of the Moon, this research is important for understanding the limitations of the APSE data, as well as the limits and potential of any future seismic survey on highly scattering bodies. In Chapter 5 we examine whether future seismometer deployments in large lunar basins would record less scattering than the APSE seismic stations. The research presented in this thesis thus not only gives new insight into the mechanisms controlling the propagation of seismic energy in the Moon, but it also allows us to make predictions regarding the characteristics of the seismic signals that could one day be recorded on other Solar System objects (e.g., asteroids and Mars).

## **1.2 Scientific Context and Background**

The Apollo Passive Seismic Experiment consisted of a network of four seismometer packages forming a nearly triangular array with Apollo stations 12 and 14 at one corner, and stations 15 and 16 each about 1100 km away (Figure 1.4). Each seismometer package comprised a three component long-period seismometer (two horizontal channels, LPX and LPY, and one vertical channel, LPZ) and a vertical short-period instrument (SPZ). The LP components had an instrument response ranging from 0.004 to  $\sim$ 2 Hz and could be operated in one of two modes: flat mode, more sensitive to lower frequency signals (natural frequency of 0.07 Hz), and peak mode, with a sharp peak in ground motion sensitivity at 0.45 Hz, but with a reduced sensitivity to low-frequency signals ( $< 0.45$  Hz). The SP instrument response ranged from 0.05 to 20 Hz, peaking at approximately 8 Hz. The APSE package weighed approximately 11.5 kg, only about a third of the typical terrestrial single-axis seismometer at the time, and was wrapped in insulating aluminized

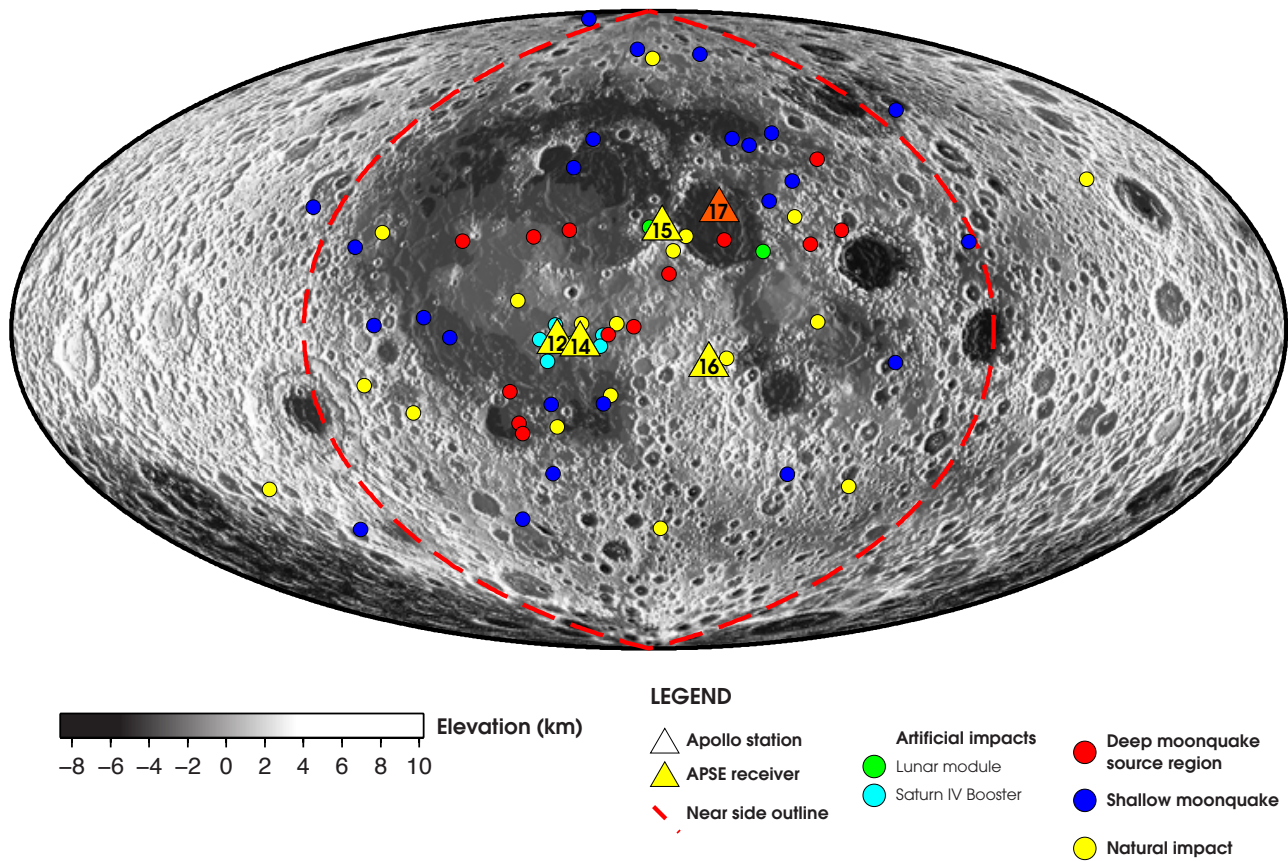


Figure 1.4: Map showing the locations of the four APSE receivers (Apollo stations 12, 14, 15 and 16), and the epicenters of the seismic events used in the study presented in Chapter 2. Most located events in the APSE dataset occurred on the lunar near side (outlined by the red dashed line). The location of Apollo station 17, where an active seismic experiment studied near-surface seismic velocity structure, is also shown. Station 17, however, was not part of the APSE network. The background is a shaded relief map of the surface topography, acquired by the LOLA instrument aboard the Lunar Reconnaissance Orbiter. This is a Hammer projection centered on longitude  $0^{\circ}$  showing the entire lunar surface.

## 1.2. Scientific Context and Background

---

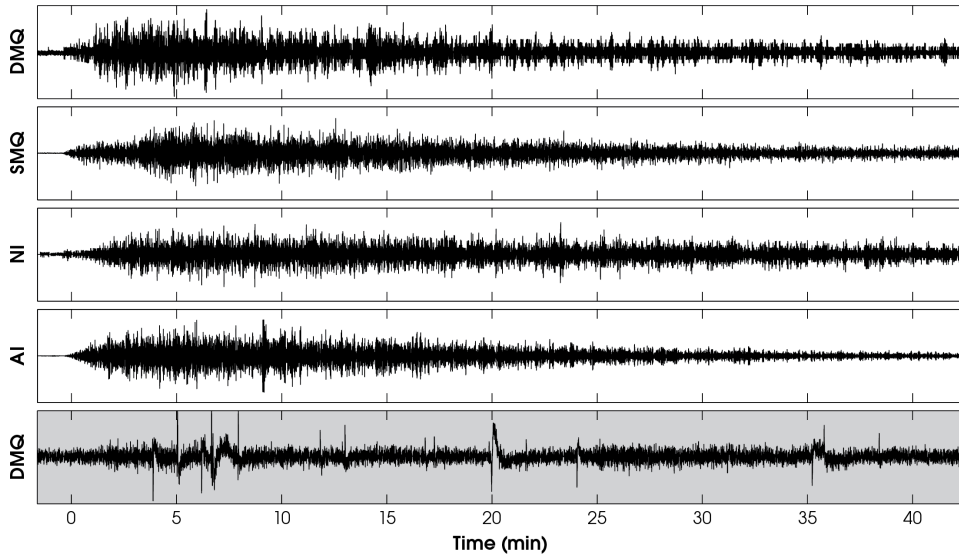


Figure 1.5: Examples of good quality signals: deep moonquake (DMQ), shallow moonquake (SMQ), natural impact (NI), and artificial impact (AI). P-wave arrivals are fairly easily identified visually. S-wave arrivals are not as clear and are partially obscured by the P-wave coda. Signals of this quality make up only 3% of the recorded events. Most signals look like the signal in the bottom plot, which is a DMQ from the same source region as the top DMQ example (A001).

## 1.2. Scientific Context and Background

---

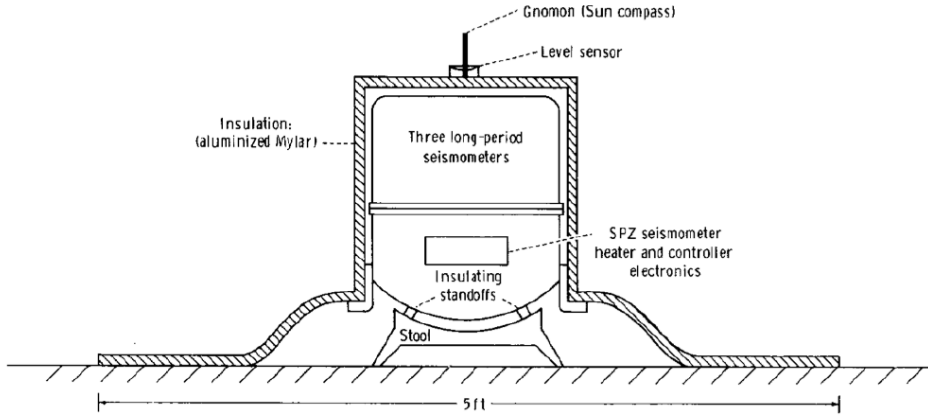


Figure 1.6: Schematic diagram of the APSE unit, showing the location of the LP (top) and SP (bottom) instruments, as well as the insulating aluminized Mylar wrapping. Image reproduced from Latham et al. [1970a] with permission from NASA.

Mylar, which reduced temperature variations on the surface of the instruments as shown in Figure 1.6 [Latham et al., 1970a]. The recorded seismic data was telemetered to Earth, where occasional transmission errors resulted in various gaps and/or large amplitude spikes in the data record [Nakamura et al., 1980]. Noise in the data also originated from several other distinct sources (e.g. passage through the day/night terminator, temperature variations on the lunar surface, the lunar seismic hum due constant regolith gardening, etc. [Dorman et al., 1978; Lognonné et al., 2009; Sens-Schönfelder and Larose, 2010]). Some of these noise sources resulted in high amplitude spikes in the data that could be removed or reduced through various filtering techniques (e.g., Bulow et al. [2005]).

Four types of events were identified in the APSE data. Deep moonquakes (DMQ) have depths ranging from 700 km to 1100 km, and occur repeatedly in very localized source regions. DMQ occurrence times exhibit periodicities present in the spectrum of the Earth-Moon tides [Lammlein et al., 1974]. Several thousand DMQs have been identified in the APSE data. Shallow moonquakes (SMQ) are thought to occur at depths of less than 150 km. Only 28 events were identified, but

## *1.2. Scientific Context and Background*

---

the quality and clarity of the P- and S-wave arrivals are much higher than for DMQ events. It is still unknown whether SMQs occur in the crust or upper mantle [Nakamura et al., 1974; Lognonné et al., 2003]. The focal mechanisms of both DMQ and SMQ events have not been identified because of the small number of seismic stations and the poor quality of the P- and S- arrivals. Thus, unlike on Earth the type of faulting giving rise to lunar seismicity is unknown. Furthermore, uncertainty in the hypocenter locations can be large ( $\sim$ 30-1000 km). Natural impacts (NI) were also recorded in the APSE data. Seismic waves generated when a meteoroid hits the lunar surface are extremely useful for inferring the seismic velocity profile of the lunar crust and upper mantle because the source depth is known, reducing the uncertainty in their locations. Artificial impacts (AI) that occurred close to the stations when the Lunar Modules or the Saturn IV Boosters were dropped on the lunar surface are also useful because of their known times of impact, locations, and depths.

Good quality signals of the different types of seismic events are presented in Figure 1.5 (top 4 signals). Recordings of this quality make up only 3% of all recorded APSE events. Most signals are of the quality shown on the bottom plot of Figure 1.5. The events' long duration ( $\sim$ 60 min) and the incoherent wave trains are the subjects of study of this thesis, and results from the low intrinsic attenuation and high scattering in the lunar interior.

The most probable origin of scattering in the lunar coda is the megaregolith layer and the underlying fractured crust. The lunar megaregolith is defined as the highly fragmented layer, composed of the ejecta of the large basin-forming impact events, that lies on top of the fractured but in-situ crust (see Figure 1.7) [Hartmann, 1974]. Several estimates of the megaregolith thickness have been published, based either on ejecta excavation and deposition models [McGetchin et al., 1973; Pike, 1974; Housen et al., 1983; Petro and Pieters, 2004, 2008], or on radar and optical data [Shkuratov and Bondarenko, 2001; Thompson et al., 2009]. However, the range of published estimates is large (from a few hundreds of meters up to  $\sim$ 10 km thick). Information stored in the scattered coda of lunar seismic events can potentially constrain parameters such as the thickness of the scattering layer beneath the stations (see Dainty et al. [1974]) and the mean free path between scatterers (width of ejecta blocks).

## 1.2. Scientific Context and Background

---

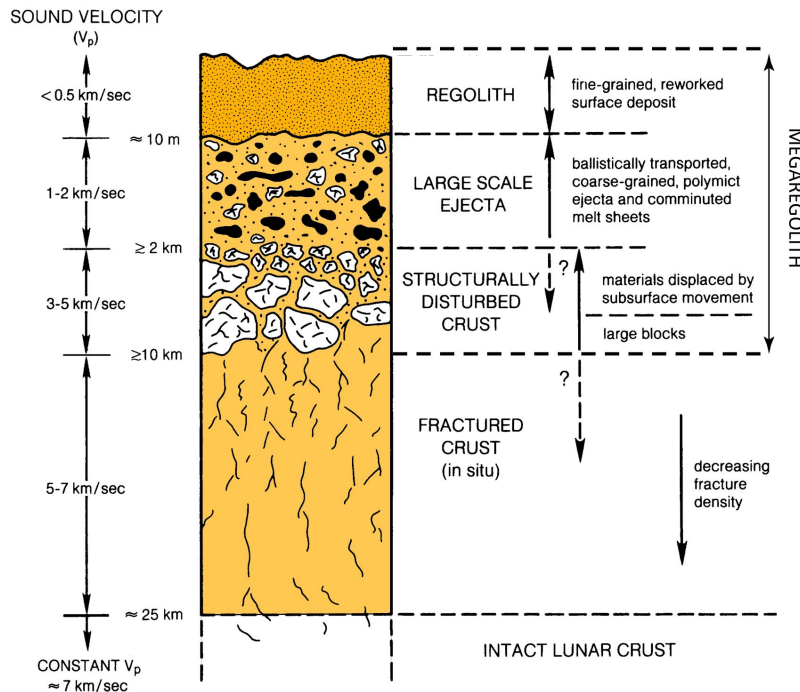


Figure 1.7: Schematic cross-section illustrating the make-up of the lunar megaregolith. The megaregolith layer goes from the upper finer grained regolith to the top of the fractured, in situ crust. The estimated thickness of the entire structure, including the fractured crust, is in the order of 10's of kilometers. Seismic velocities are from Toksöz et al. [1973]. Schematic is modified from Hörz [1991], with permission from *Cambridge University Press*.

## *1.2. Scientific Context and Background*

---

The literature on wave propagation in heterogeneous media on Earth is extensive. Energy from local earthquakes (for which the distance between source and receiver is  $\sim$ 100 km or less), propagating through a laterally heterogenous lithosphere, often results in seismic coda with qualitatively similar characteristics to those observed in the APSE data (e.g., Aki [1969]; Aki and Chouet [1975]; Margerin et al. [1999]). Several theoretical approaches to explain those characteristics have been developed and applied successfully to terrestrial seismograms. These all resort to a statistical treatment of scattering, which allows the dominant characteristics of the coda to be modeled using a small number of parameters. Different models can be used depending on the effective scattering strength of the medium. Single-scatterer to multiple-scatterer models are applicable in the case of weak to moderate scattering [Aki, 1969; Aki and Chouet, 1975]. These assume interactions of the seismic waves with a given number of point-like scatterers. Energy diffusion and radiative transfer models are used for more intensively scattering media [Latham et al., 1970b; Aki and Chouet, 1975; Margerin et al., 1998]. Scattering on the Moon is strong and so the latter models are expected to be more applicable to the APSE data [Latham et al., 1970b; Dainty et al., 1974].

Importantly, no scattering theory currently exists that is directly applicable to the lunar or other non-terrestrial contexts. The approaches described above typically model modest scattering of energy from local events, with the structural models comprising a half space (e.g. Aki and Chouet [1975]) or a constant velocity plane layer over a half space (e.g. Margerin et al. [1998, 1999]), or low-level deep mantle scattering (e.g. Earle and Shearer [2001]). The Moon is a small rocky body with low intrinsic attenuation and strong scattering. While scattering can occur throughout the lunar interior, the major contribution likely arises from the megaregolith layer which is global in extent, though spatially variable in thickness and structure. All events in the APSE data set exhibit a long coda, indicating that scattering affects all types of events, from any depth and any epicentral distance. Thus seismic energy propagation in the Moon, or in any other bodies with high scattering levels (e.g. potentially asteroids, Mars), is inherently different from on Earth and further modeling and analytical work is warranted.

### 1.3 Thesis Structure

This thesis comprises four complementary studies that each helps build a better understanding of the causes and effects of highly scattering environments on seismic energy propagation. The studies from Chapters 2 and 4 directly address the lunar context, whereas the studies in Chapters 3 and 5 can be applied more generally to planetary bodies with high scattering levels.

In Chapter 2, I have made the first systematic analysis of scattering in the Apollo lunar seismic data, characterized through the rise and decay parameters of the seismic coda. This was done by measuring the coda wave characteristic decay times ( $\tau_d$ ) and decay factor ( $Q_c$ ) for all the types of seismic events, in several frequency bands, at all four Apollo stations.  $\tau_d$  and  $Q_c$  are described in detail in Chapter 2 and are both measures of the integrated effects of the scattering encountered by the seismic energy as it travels from the source to the receiver. Large values of  $\tau_d$  (slow decay times) indicates a high level of scattering. This study is the first research work that uses the Apollo seismic dataset to build understanding of the effect of a highly scattering medium on the propagation of seismic energy on a global planetary scale. As part of this study, I have identified much greater scattering for shallow ( $\sim 0\text{-}200$  km depth) versus deep ( $> \sim 700$  km) sources and for frequencies greater than 2 Hz. This confirms that the megaregolith is playing a major role in the scattering of seismic energy. The results also indicate that the effect of scattering would be less at frequencies lower than those observed by the APSE experiment (mostly sensitive to the 0.5-10 Hz range), which will be helpful in the future design of lunar (or other planetary bodies) seismic surveys. Finally, the results and interpretations provide constraints and testable hypotheses for lunar waveform models that include the effect of intense scattering and a near-surface low velocity layer, and this motivates the two subsequent studies of my thesis.

In Chapter 3, I model the ground deformation caused by seismic energy travelling in highly scattering medium using a “phonon method”. This method tracks a large number of seismic wavelets (the phonons) from a seismic source (quake, or surface impact) and record the ground deformation each time they reach the surface. This method is favoured over other synthetic seismic modeling methods using the wave equation (e.g. spectral finite element, frequency-wavenumber) because it

### 1.3. Thesis Structure

---

can reach much larger frequencies and signal durations in very highly heterogeneous medium with much less computational power. My updated method provides the first numerical modeling of 3-D scattering (with 1-D background velocity models), with user-defined power-law distributions of scatterer length-scales, frequency dependent intrinsic attenuation, as well as global background scattering. As part of this study, I modeled the ground deformation for simple subsurface models and varied each model parameter independently in order to asses their individual effect on the seismic coda. The main results show that the magnitude of the decay times is most affected by the background velocity model in particular the presence of shallow low velocity layers, the event source depth, and the intrinsic attenuation level. The decay times are also controlled to a lesser extent by the size-frequency distribution of scatterers, the thickness of the scattering layer and the impedance contrast at the scatterers.

In Chapter 4, I establish some constraints on the scattering and attenuation structures of the Moon using the APSE-derived decay parameters from the study in Chapter 2, along with synthetic modeling. By investigating the decay characteristics of synthetic signals generated in varying scattering environments, we can identify a suite of lunar interior models that produce rise and decay characteristics similar to those observed in the Apollo Passive Seismic Experiment data. This study is the first to constrain lunar interior scattering properties using my new combined approach of APSE data analysis and numerical modeling. I demonstrate that in order to get lunar-like signals, we not only need high scattering levels and low intrinsic attenuation (as suggested in the literature), but also seismic velocity structures that tend to trap the seismic energy near the surface and in the scattering layer (e.g. very low velocity regolith, crust, sharp velocity gradient with depth). I also use this approach to independently constrain the intrinsic attenuation factor values near the Apollo stations ( $Q_i \sim 4000 - 6000$ ).

In Chapter 5, I determine locations on the lunar surface that minimize the effect of scattering on recorded seismic signals, and that have the potential to maximize science returns of future seismic surveys. I used the phonon method detailed in Chapter 3 to model the ground deformation in environments with laterally varying megaregolith thicknesses. I show that ideal locations for seismic receivers would be in large impact structures (assumed to have a thinner megaregolith than the

### *1.3. Thesis Structure*

---

highlands), away from the basins' edges in order to avoid noise from the surrounding thicker megaregolith. Locations above thin crust and thin regolith are also preferred in order to minimize the focusing of seismic energy in the near-surface megaregolith.

## Chapter 2

# Investigation of Scattering in Lunar Seismic Coda

### 2.1 Introduction

Data collected during the Apollo Passive Seismic Experiment (APSE, 1969–1977) have been pivotal in understanding lunar interior structure. However, with a few exceptions [Nakamura et al., 1975; Horvath et al., 1980; Vinnik et al., 2001; Weber et al., 2011; Garcia et al., 2011], analyses of seismic phases other than initial P- and S-wave arrivals has proved challenging due to the following characteristics of lunar seismograms: long durations, low amplitudes, lack of identifiable secondary wave arrivals, gradual build up of energy from the onset of the events, and a slow amplitude decay from the maximum amplitude to the time when the signal amplitude reaches the background noise level at the end of the event. The long coda (typically  $\sim$ 60 minutes or more) result from transmission of seismic energy within a poorly attenuating, and highly scattering medium [Latham et al., 1970a; Nakamura, 1977]. These coda represent a largely untapped source of information about the lunar interior and near-surface layers.

On the Moon, past studies have looked at the frequency content of the coda to investigate geological structure surrounding the receivers. Nakamura et al. [1975] used the peak frequency of the ratio of the horizontal and vertical components to estimate thicknesses of 3.7–4.4 m for the fine-grained regolith layer beneath Apollo stations 11, 12 and 15. The study also identified a layer beneath the regolith whose P-wave velocities of 250–400 m/s could correspond to those of welded tuff deposited by major impact or extensively fractured rocks. Horvath et al. [1980] used a spectral approach to calculate a seismic velocity profile for the near-surface

## 2.1. Introduction

---

layers, to a depth of  $\sim$ 200 m. The decay of the coda amplitude with time can also be used to investigate the properties and structure of the scattering layer in which the coda is generated. The parameter typically used to characterize the coda decay is the quality factor,  $Q_c$ , where the inverse,  $Q_c^{-1}$ , represents the fraction of energy dissipated per cycle at a given frequency,  $f$ . Latham et al. [1970b] used diffusion theory (applicable in cases of intense wave scattering) to model the energy envelope function of a Lunar Module impact at Apollo station 12. The study found a coda  $Q_c$  of 3600, up to an order of magnitude larger than that typical of terrestrial crustal materials (100–1000, e.g., Jin and Aki [1988]). However, there exists no systematic study of scattering for all event types at all four APSE stations, which is the main motivation behind this study.

As explained in Chapter 1, scattering of seismic energy on the Moon probably occurs in the near-surface megaregolith layer. Understanding the scattering properties of the megaregolith is important because it will provide constraints on the shallow seismic structure of the Moon, as well as contribute to understanding megaregolith formation and evolution on other terrestrial bodies. In addition, a quantitative study of the effects of scattering in current lunar seismograms is needed to be able to assess whether secondary seismic phases (from velocity contrasts in the lunar interior) can be identified in the Apollo or future data sets.

I conduct a systematic survey of the coda characteristics of impacts and moonquakes recorded at all four APSE stations. I briefly describe the APSE dataset (Section 2.2), data processing steps and criteria used to identify higher quality seismograms (Section 2.3). These steps result in a total of 369 seismograms from 72 events at 55 distinct locations usable for this study (Figure 2.1 and Table 2.1). For these seismograms, the coda are characterized via their rise times (time from initial P- or S-wave arrival to maximum P- or S-wave amplitude), their maximum coda amplitudes, and their characteristic decay times ( $\tau_d$ ), where  $\tau_d$  is the time taken for the coda amplitude to drop by a factor of  $e$ . I investigate any dependence of these parameters on source type, on source depth, and on source-receiver epicentral distance. Those dependences are evaluated in seven different frequency bands.

Analysis of the results (sections 2.4 and 2.5) focuses on two specific questions: (1) What is the importance of global versus local (near the seismic stations) structure on the overall characteristics of the seismic signals? (2) What is the con-

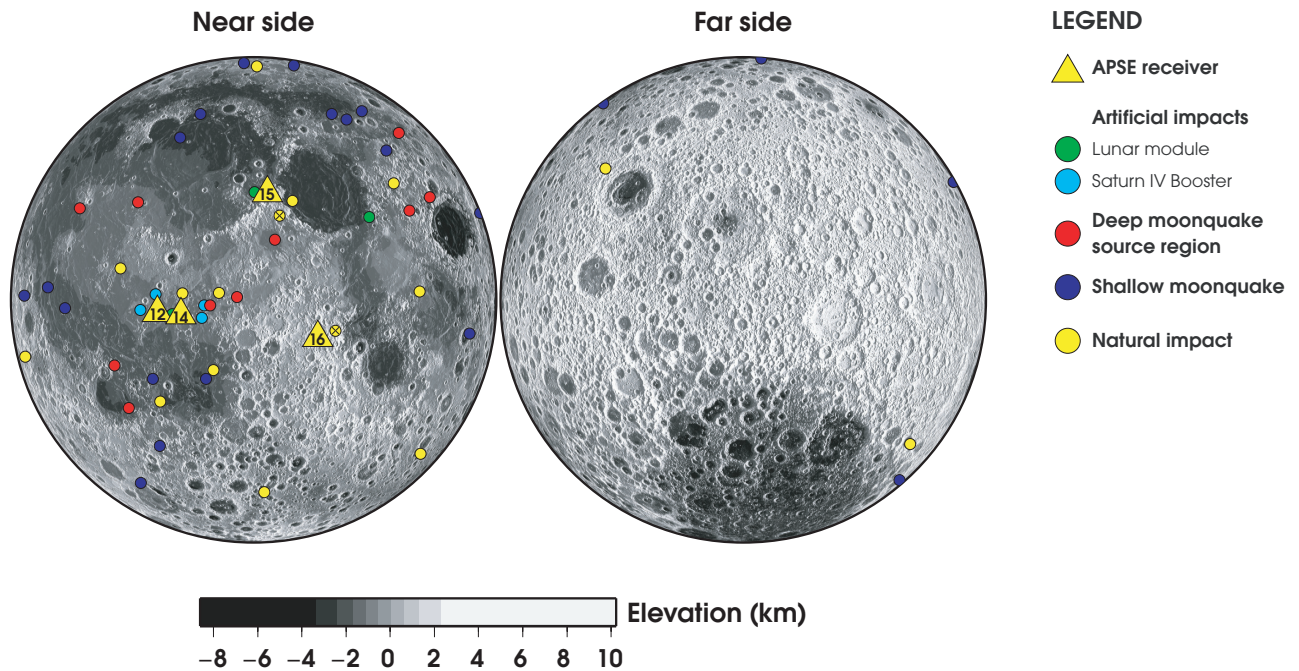


Figure 2.1: Map showing the locations of the four APSE receivers (Apollo stations 12, 14, 15 and 16), and the epicenters of the seismic events used here. Most located events in the APSE dataset occurred on the lunar near side. The background is a shaded relief map of the surface topography, acquired by the LRO-LOLA instrument.

## 2.1. Introduction

---

tribution of intrinsic attenuation ( $Q_i$ ) and scattering attenuation ( $Q_s$ ) to the signals' coda decay? The results clearly demonstrate the need for future theoretical work and synthetic seismogram modeling.

Table 2.1: Occurrence time and location of events used in this study. LM and SIVB refer to Lunar Module and Saturn IV Booster, respectively. Source for event locations: AI from Nakamura [1983] and Lognonné et al. [2003], NI from Lognonné et al. [2003], SMQ from Nakamura et al. [1979], and DMQ from Nakamura [2005]. Source for event depths: (a) From Nakamura [2005], and (b) from Gagnepain-Beyneix et al. [2006].

Type	Year	Day	Hr:Min	Lat. (°N)	Long. (°E)	Depth <sup>a</sup> (km)	Depth <sup>b</sup> (km)
<b>Artificial impacts</b>							
LM12	1969	324	22:17	-3.9	-21.2	0	0
LM14	1971	038	00:47	-3.4	-19.7	0	0
LM15	1971	215	03:07	26.4	0.3	0	0
LM17	1972	350	06:52	20.0	30.5	0	0
SIVB13	1970	105	01:09	-2.8	-27.9	0	0
SIVB15	1971	210	20:40	-1.5	-11.8	0	0
SIVN16	1972	110	21:03	1.3	-23.8	0	0
SIVB17	1972	345	20:32	-4.2	-12.3	0	0
<b>Natural impacts</b>							
	1972	004	06:35	74.1	2.6	0	0
	1972	134	08:46	1.5	-17.1	0	0
	1972	199	21:56	32.8	137.6	0	0
	1972	213	18:08	24	10.1	0	0
	1973	269	20:48	28.7	41.1	0	0
	1973	358	10:05	-24.8	-25.1	0	0
	1974	109	18:34	7.4	-33.6	0	0
	1974	198	12:05	20.3	6.5	0	0
	1974	325	13:16	-7.3	19.9	0	0
	1974	349	09:08	1.6	-8.2	0	0
	1975	064	21:52	-52.4	4.2	0	0
	1975	102	18:15	2	43.2	0	0
	1975	124	10:05	-36.4	-121.3	0	0
	1976	013	07:14	-39.4	62.8	0	0

Continued on next page

## 2.1. Introduction

---

**Table 2.1 – continued from previous page**

Type	Year	Day	Hr:Min	Lat. (°N)	Long. (°E)	Depth <sup>a</sup> (km)	Depth <sup>b</sup> (km)
	1976	149	06:03	-16.8	-10.0	0	0
	1977	179	22:25	-13.5	-75.3	0	0
<b>Shallow moonquakes</b>							
	1971	107	07:04	48	35	-	-
	1971	140	17:29	42	-24	-	-
	1972	002	22:32	54	101	-	-
	1972	341	23:10	51	45	-	10
	1973	072	08:01	84	-134	-	-
	1973	171	20:25	1	-71	-	-
	1973	274	04:00	-37	-29	-	-
	1974	086	09:11	-48	-106	-	-
	1974	192	00:52	21	88	-	-
	1975	003	01:47	29	-98	-	0
	1975	012	03:17	75	40	-	0
	1975	013	00:28	-2	-51	-	-
	1975	044	22:05	-19	-26	-	21
	1975	127	06:40	-49	-45	-	-
	1975	147	23:32	3	-58	-	-
	1975	314	07:56	-8	64	-	-
	1976	004	11:20	50	30	-	125
	1976	012	08:22	38	44	-	-
	1976	066	10:16	50	-20	-	185
	1976	068	14:44	-19	-12	-	-
	1976	137	12:36	77	-10	-	-
<b>Deep moonquakes</b>							
A001	-	-	-	15.7	-36.6	867	917
A006	-	-	-	43.5	55.5	844	860
A007	-	-	-	25	53.2	893	900
A015	-	-	-	0.7	-3.9	747	-
A020	-	-	-	23.7	-31.4	945	1055
A022	-	-	-	21.6	43.6	788	-
A026	-	-	-	14.3	5.2	1122	-
A040	-	-	-	-1.3	-10.3	867	886
A042	-	-	-	22.2	-50.7	907	1004
A209	-	-	-	-26.5	-35.1	-	-

## 2.2 Data

Four main types of seismic events were recorded at four Apollo stations: artificial impacts (AI, including the Lunar Module impacts and the Saturn-IV Booster impacts), natural impacts (NI), deep moonquakes (DMQ) and shallow moonquakes (SMQ). The data were recorded on three orthogonal long-period channels (LP) with an instrument frequency response of 0.004 to 2 Hz and on one vertical short-period channel (SP) with a frequency response of 0.05 to 20 Hz. The long-period instruments could be operated in one of two modes: flat mode, more sensitive to lower frequency signals (natural frequency of 0.07 Hz), and peak mode, with a sharp peak in ground motion sensitivity at 0.45 Hz, but with a reduced sensitivity to low-frequency signals (< 0.45 Hz, see Figure 2.2). The different channels are identified here as LPX, LPY and LPZ for the two horizontal and the vertical long-period channels and as SPZ for the vertical short-period channel. The LPZ component at station 14 worked properly only for a short time and only 3 recordings from this channel are used in this study. Also, the SPZ component at station 12 malfunctioned early on and did not record any events [Latham et al., 1970b]. The data were obtained from the IRIS Data Management Center ([www.iris.edu/dms/dmc/](http://www.iris.edu/dms/dmc/)).

## 2.3 Methodology

### 2.3.1 Data Processing Steps

The data were initially bandpass filtered and despiked using a robust median de-spiking algorithm [Bulow et al., 2005]. The long-period data were filtered from 0.25 to 3.31 Hz (the Nyquist frequency) and the short-period data were filtered from 2 to 10 Hz. A 2 minute running median filter was used to despike the data by cropping amplitudes larger than 5 times the median. These steps removed long term fluctuations, as well as most of the thermal and noise spikes.

All DMQ, SMQ, NI and AI events in the lunar seismic catalogue [Nakamura, 1992] were visually inspected and a signal was selected if it met the following criteria: (i) a clear decaying coda is present, (ii) at least one of the P- or S-wave arrival times is identifiable, (iii) the ratio of the maximum amplitude of the S-

### 2.3. Methodology

---

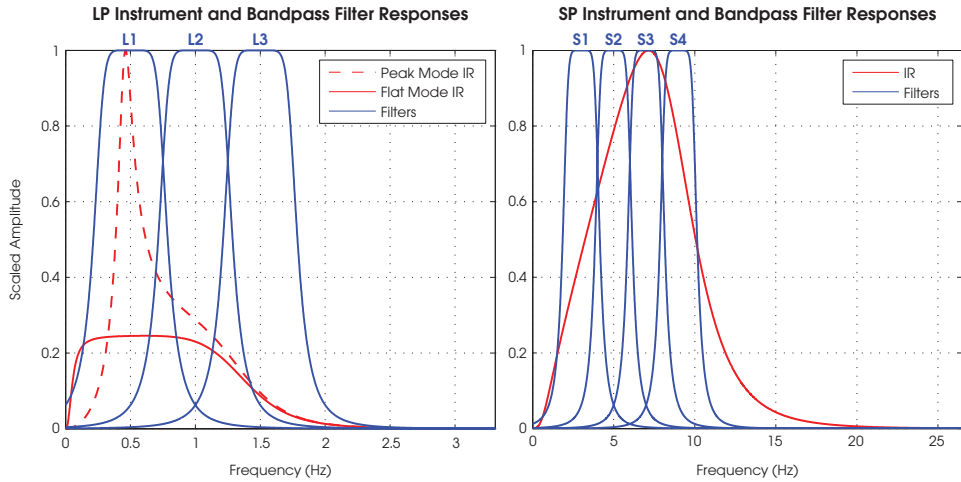


Figure 2.2: Instrument response curves (IR, red) and frequency response curves of bandpass filters used in the analysis (blue). The left plot shows the long-period (LP) instrument responses, both in flat and peak mode. The right plot shows the short-period (SP) instrument response curve.

coda to the root-mean-square (RMS) amplitude of the noise is larger than 3. The noise was measured in a 2 minute window preferably before the P-wave arrival, or once the coda amplitude has decayed to the background level in cases where the data before the signal was not available or not optimal (e.g. if the data had large amplitude spikes). A total of 369 signals from 72 events were selected for analysis. As some of the events are DMQ that occurred at the same source region, the number of distinct locations is 55 (Table 2.1 and Figure 2.1). Arrival times for DMQ were identified through cross-correlation of the individual events with their respective source region stack. The stacks were generated using the method described in Bulow et al. [2005]. SMQ, NI and AI arrival times were identified visually.

Each signal was corrected for the instrument response using the well established Seismic Analysis Code, applying prewhitening to flatten the spectral response [Goldstein et al., 2003; Goldstein and Snoke, 2005]. This allows us to compare analyses from signals recorded on long-period channels, whether they were recorded while the instrument was in peak or in flat mode. Events recorded in peak

### 2.3. Methodology

---

mode account for 71% of the total events recorded on the long-period channels used here.

Signals were then bandpass filtered to allow the measurement of the coda characteristic decay time and the coda rise time in specific frequency bands. The bands for the LP signals were set to be 0.5 Hz wide and centered on the 0.5, 1.0 and 1.5 Hz frequencies. The bands for the SPZ signals were set to a width of 2 Hz and centered on the 3, 5, 7 and 9 Hz frequencies. Similar studies using earthquake data will typically use octave-wide bandpass filters (centered at 1.5, 3, 6, 12 Hz, and so on, e.g. Tsujiura [1978]). However, due to the limited bandwidth of the Apollo instruments, the use of filters of constant width is necessary in order to allow investigation of the dependence of decay and rise times on frequency. The different bands used in this analysis are discussed in the text as L1, L2 and L3 for the long-period bands, and S1, S2, S3 and S4 for the short-period bands (Table 2.2 and Figure 2.2). Figure 2.2 shows that the SP instrument response extends past 10 Hz, however the signal-to-noise ratio of the seismic signal above 10 Hz is too low for the decay to be measured accurately.

Signal envelopes were generated using:

$$E(t) = \sqrt{D(t)^2 + H(t)^2} \quad (2.1)$$

where  $D(t)$  is the original data,  $H(t)$  is the Hilbert transform and  $E(t)$  is the resulting envelope. Envelopes of LPX and LPY channels were averaged using:

$$E_H(t) = \sqrt{E_X(t)^2 + E_Y(t)^2} \quad (2.2)$$

where  $E_H(t)$  is the resulting envelope of the averaged horizontal long-period channel, and  $E_X(t)$  and  $E_Y(t)$  are the envelopes of the LPX and LPY components. This step increases the signal-to-noise ratio around the S-wave arrival. The averaging assumes horizontal isotropy, a step that is justified by the similar (but noisier) results obtained individually for LPX and LPY. This step and the previous bandpass filtering step generated a set of 842 analyzable seismic traces. The envelope was smoothed using a 5 minute (LP) or 35 second (SPZ) running window ( $\sim 2000$  sampling intervals), keeping the 75th percentile. The window length and percentile

### 2.3. Methodology

---

Table 2.2: The different frequency bands investigated in this analysis.  $f_c$  is the central frequency of each band.

	In text	Range (Hz)	$f_c$ (Hz)
Long-Period	<b>L1</b>	0.25–0.75	0.5
	<b>L2</b>	0.75–1.25	1.0
	<b>L3</b>	1.25–1.75	1.5
Short-period	<b>S1</b>	2–4	3.0
	<b>S2</b>	4–6	5.0
	<b>S3</b>	6–8	7.0
	<b>S4</b>	8–10	9.0

were empirically determined to retain the characteristic signal amplitude, while reducing the contribution from remaining noise spikes. Different window lengths (2 to 7 minutes for LP, 15 seconds to 1 minute for SPZ) and percentile values (the median and 99th percentile) were tested and yielded comparable results.

#### 2.3.2 Analytical Solutions for the Coda Decay

Analytical solutions for coda decay are typically of the form

$$E(t) = \frac{1}{t^\alpha} e^{-t/\tau_d} \quad (2.3)$$

where  $\tau_d$  is the characteristic decay time. The value of  $\alpha$  can range from 0.75 to 2 and depends on the model geometry (which affects the geometrical spreading) and on the scattering environment (see review in Shearer [2007]). The model that most closely resembles the lunar scattering environment is that of Margerin et al. [1998], in which a scattering layer overlies a more transparent half-space. However, the lunar and terrestrial contexts are inherently different in the following ways:

1. Studies of terrestrial coda waves mostly use local crustal events (see examples in Yoshimoto and Jin [2008]). In the formulation of Margerin et al.

### 2.3. Methodology

---

[1998], the point-like source resides in the scattering layer, close to the receiver. On the Moon, these assumptions are only valid for a few impact events local to the seismic stations. For most impacts and some or all shallow moonquakes, the source resides on or in the near-surface scattering layer, but because the events are teleseismic much of the energy travels in the mantle before entering, or re-entering, the scattering layer en route to the receiver. This effectively results in an infinite number of sources along the base of the scattering layer, instead of a single source.

2. In Margerin et al. [1998], the scattering layer lies above a weakly or non-scattering half-space. Scattered energy leaks into the half-space, and does not return to the scattering layer. The Moon is a small spherical body with increasing velocity with depth, and low intrinsic attenuation. As such, seismic energy that propagates through the mantle re-enters a near-surface highly scattering layer elsewhere no more than 7 minutes later (the approximate time it takes for a downgoing P-wave to travel through the lunar interior and reach the surface). Seismic energy can go through this process several times due to the low lunar intrinsic attenuation. The net result is that once the body waves have expanded through the majority of the scattering layer's volume (about 12-14 minutes after the quake source time, or the time it takes for an S-wave to travel the lunar interior), the many multiply-scattered waves within a sphere reduce wave expansion within the scattering layer ( $\alpha \rightarrow 0$ ). Lunar coda last for 30 to over 60 minutes after the S- wave arrival, suggesting that geometrical spreading, which is captured by the  $\alpha$  parameter in equation 2.3, should have a reduced effect on the coda decay.

Thus currently there is no published theoretical solution for the coda decay that is directly applicable to the lunar environment, but the above discussion suggests that solutions with  $\alpha \rightarrow 0$  might be expected. In the analyses I set  $\alpha$  equal to zero in equation 2.3. In Section 2.4.3 I discuss further the implications of using a different choice of  $\alpha$ .

An exponential decay curve of the form  $e^{-t/\tau_d}$  was fit using least-squares to the decay of the smoothed envelope function and  $\tau_d$  was retrieved. The beginning of the fit was identified visually, as the exponential decay does not always start at

### 2.3. Methodology

---

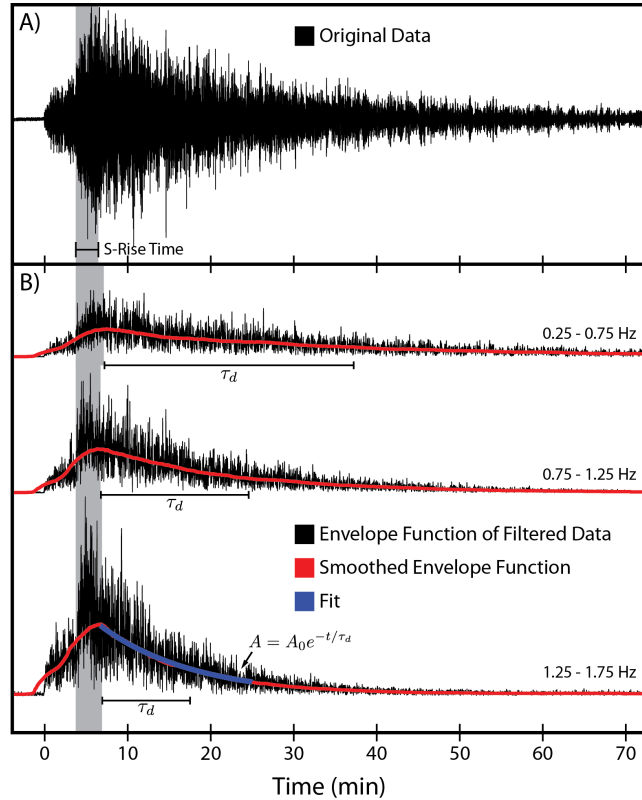


Figure 2.3: Example of the different methodology steps for a SMQ. A) Original data, on the LPX channel. B) The 3 bandpass filtered envelope functions for the averaged LPX and LPY channels (black), the smoothed envelopes (red) and the resulting fit (blue) for the highest frequency band. The characteristic decay times  $\tau_d$  (labeled on figure) and S-rise times (gray band) are also shown. Note that these vary with frequency.

## 2.4. Results

---

the maximum coda amplitude. The end of the fit was determined numerically and defined as the time at which the envelope amplitude is twice the RMS background noise. Only those fits for which  $\tau_d$  is less than the length of the fit were kept for the final analysis, resulting in 641 decay times. Figure 2.3 summarizes the methodology steps discussed above. The envelope functions can also be fit in log space to reduce the relative weight of the larger amplitudes at the beginning of the coda for which the assumption  $\alpha = 0$  may not be valid. The resulting decay times, not shown, did not differ significantly from the results presented here.

The measured  $\tau_d$  were then converted to the frequency specific decay factor  $Q_c$  using:

$$Q_c = 2\pi f_c \tau_d \quad (2.4)$$

where  $f_c$  is the central frequency of the band of interest and  $Q_c$  is a dimensionless parameter called the coda wave quality factor [Aki and Chouet, 1975]. Its inverse,  $Q_c^{-1}$ , represents the fraction of energy dissipated after one period of oscillation. Results for both  $\tau_d$  and  $Q_c$  are presented in the following section as both parameters can provide insight into the attenuation and scattering properties of the Moon. For example, a decrease in  $\tau_d$  with frequency for a series of given frequency bands, with similar  $Q_c$  values for all bands, might indicate a constant intrinsic attenuation ( $Q_i$ ) over the frequency range. In this case, high frequencies lose as much energy per cycle than low frequency (constant  $Q_c$ ), but the coda amplitude will decay faster ( $\tau_d$ ) because high frequencies go through more cycles per unit time.

## 2.4 Results

Maximum amplitude and rise time results show no clear dependence on epicentral distance,  $\Delta$ , or on the source depth. The measured NI rise times in the LP bands are mostly greater than the SMQ rise times, and they decrease with increasing frequency. The SMQ rise times are constant among all 3 frequency bands (Figure 2.4). Rise time values are lower by  $\sim 15\%$  if I halve the length of the smoothing window, but the relationships among frequency, NI and SMQ values remain the same. These results support the observations reported in Latham et al. [1971].  $\tau_d$  and  $Q_c$  do not

## 2.4. Results

---

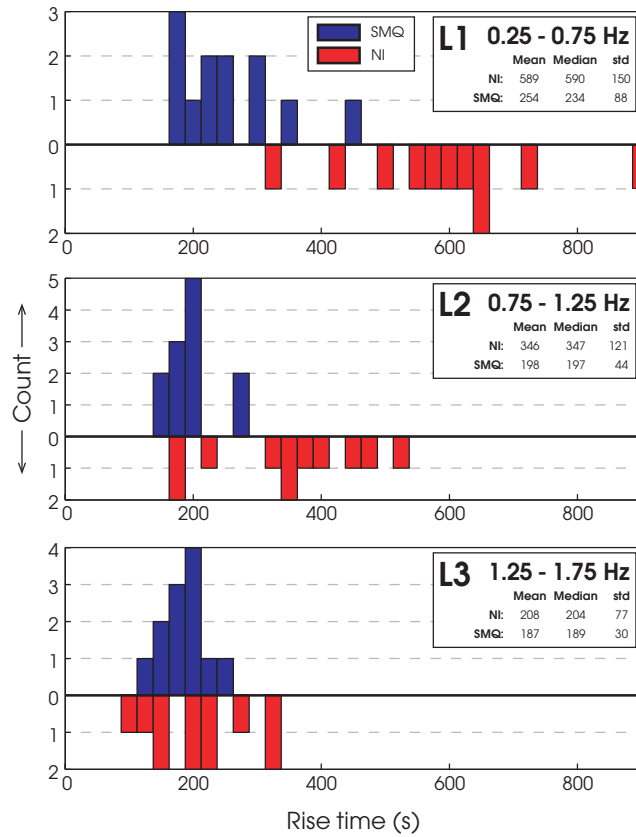


Figure 2.4: NI (red) and SMQ (blue) S-rise times for the L1, L2 and L3 bands. NI rise times are larger than SMQ rise times, and also exhibit a dependence on frequency. SMQ rise times are frequency independent. The mean, median and standard deviation (std) in seconds are given. Only the S-wave rise times that could be clearly measured are shown.

## 2.4. Results

---

exhibit a dependence on the depth of individual events, but are distinct for events occurring at the surface (impacts) and in the lunar interior (moonquakes). I refer to this below as a dependence on event type, and present the  $\tau_d$  and  $Q_c$  results for each event type as a function of  $\Delta$  and frequency (Table 2.3 and Figures 2.5–2.8). The results from the vertical and horizontal LP channels are generally very similar and so no distinction is made between the two channels in Figures 2.5–2.8.

The median  $\tau_d$  and  $Q_c$  values for all events with  $\Delta$  greater than  $20^\circ$  are given in Table 2.3. This distance was empirically determined to avoid local effects, and is based on the AI and NI results, which show either a change in  $\tau_d$  and  $Q_c$  values for  $\Delta$  between 0 and  $20^\circ$  (AI), or large differences among stations at short distances (NI). For  $\Delta$  greater than  $20^\circ$ , no clear dependence of  $\tau_d$  or  $Q_c$  on  $\Delta$  was identified on the LP components for any event type (Figures 2.5 and 2.6). Table 2.3 lists the median values for each individual frequency band, as well as for all the bands combined, along with the median absolute deviation (MAD). A dependence of  $\tau_d$  and  $Q_c$  on  $\Delta$  is seen in the short-period NI and SMQ data. The results of robust least-square fits to individual frequency bands are shown for  $\tau_d$  or  $Q_c$  vs.  $\Delta$  for the NI and SMQ (Figures 2.7 and 2.8), and Table 2.3 gives the slope and intercept ( $\tau_d$  and  $Q_c$  value at  $0^\circ$ ) of each straight line fit. All robust least-square fits were done using the bisquare weighting function. Other weighting functions (e.g. huber, andrews) yield similar results.

For comparison, I show the measured lunar  $Q_c^{-1}$  values and the corresponding  $Q_c^{-1}$  values reported for the terrestrial lithosphere (Figure 2.9). Lower attenuation and/or higher scattering in the Moon are responsible for the much lower lunar  $Q_c^{-1}$  values (higher  $Q_c$ ) compared with those obtained for Earth.

Below I discuss the  $\tau_d$  and  $Q_c$  results measured on the long-period and short-period channels in more detail. I focus on any dependence on distance, frequency, and any differences among stations.

### 2.4.1 Decay Parameters Measured on the Long-Period Channels (LP)

$\tau_d$  values decrease with increasing frequency for all event types on the LP channels, consistent with faster decay of high frequency signals compared with low

## 2.4. Results

---

Table 2.3: Results from the long- and short-period bands. Long-period: Median  $\tau_d$  and  $Q_c$  values and median absolute deviation (MAD) for individual frequency band (L1, L2, and L3) and for all the bands combined. The median values are calculated from all events with epicentral distances ( $\Delta$ ) larger than  $20^\circ$ , to avoid local effects. Short-period results: Interpolated  $\tau_d$  and  $Q_c$  values at  $\Delta = 0^\circ$  ( $\tau_d(0)$  or  $Q_c(0)$ ) and the slope of the best-fit straight line.  $N$  indicates the number of data points used to calculate the median values or the best-fit lines.

Band	<b>Long-Period</b> <i>N</i>	Median $\tau_d$	Median $Q_c$	Band	<b>Short-Period</b> <i>N</i>	$\tau_d(0)$	$Q_c(0)$
		(MAD)	(MAD)			( $d\tau_d/d\Delta$ )	( $dQ_c/d\Delta$ )
<b>Artificial impacts</b>							
L1	3	2732 (239)	8582 (750)			-	-
L2	7	1625 (258)	10212 (1618)			-	-
L3	2	932 (126)	8788 (1192)			-	-
All LP	12	1652 (530)	8982 (1512)			-	-
<b>Natural impacts</b>							
L1	47	2330 (327)	7322 (1030)	S1	16	380 (1.4)	7164 (26)
L2	62	1362 (131)	8556 (824)	S2	11	234 (1.4)	7362 (44)
L3	46	865 (199)	8438 (1876)			-	-
All LP	155	1405 (492)	8364 (1302)			-	-
<b>Shallow moonquakes</b>							
L1	30	2011 (433)	6316 (1360)	S1	33	298 (0.8)	5616 (14)
L2	32	1114 (80)	6998 (500)	S2	35	193 (1.2)	6052 (36)
L3	28	722 (55)	6804 (518)	S3	33	145 (1.8)	6366 (78)
All LP	90	1114 (504)	6866 (824)	S4	34	144 (2.0)	8172 (114)
<b>Deep moonquakes</b>							
L1	14	1373 (434)	4312 (1362)			-	-
L2	15	978 (143)	6202 (898)			-	-
L3	5	732 (122)	6902 (1146)			-	-
All LP	34	1062 (365)	5882 (1296)			-	-

## 2.4. Results

---

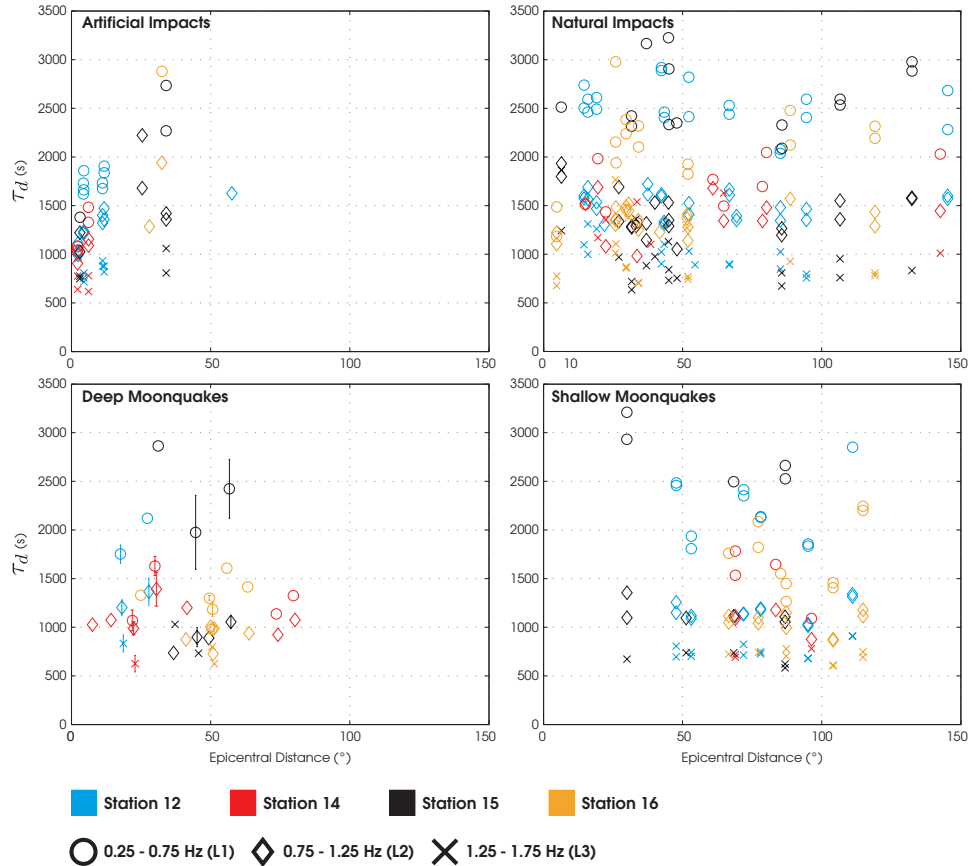


Figure 2.5: Measured  $\tau_d$  for all types of events on the LP channels. The colours represent the different stations and the symbols refer to each frequency band. No distinction is made between the vertical and horizontal channels, as the measured  $\tau_d$  are similar for a given event. Measured  $\tau_d$  from a single DMQ source region have been averaged, and the errorbars correspond to one median absolute deviation.

## 2.4. Results

---

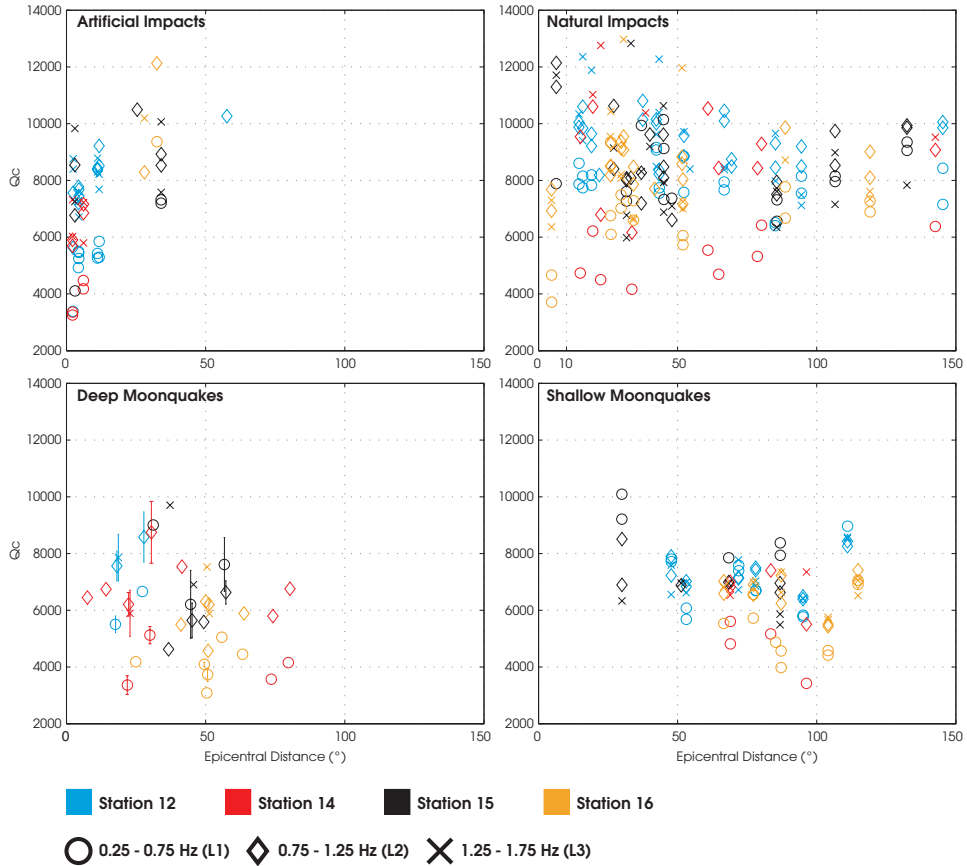


Figure 2.6: Measured  $Q_c$  for all types of events on the LP channels. The colours and symbols are the same as in Figure 2.5.

## 2.4. Results

---

frequency signals. No dependence of  $\tau_d$  or  $Q_c$  on  $\Delta$ , for  $\Delta$  greater than  $20^\circ$ , is observed. In general,  $Q_c$  values for  $\Delta$  greater than  $20^\circ$  are similar for all frequency bands for individual event types, *i.e.*, the median values for each band are indistinguishable from one another within the reported median absolute deviations (MAD) in Table 2.3. Examination of the median  $Q_c$  for all LP bands combined shows that the  $Q_c$  values for impact events are larger than the  $Q_c$  values for tectonic events ( $8982 \pm 1512$  for AI and  $8364 \pm 1302$  for NI, versus  $6866 \pm 824$  for SMQ and  $5882 \pm 1296$  for DMQ).

At epicentral distances less than about  $20^\circ$ , both  $\tau_d$  and  $Q_c$  for AI may increase with  $\Delta$ ; however this is difficult to verify, given the variability in  $\tau_d$  and  $Q_c$  measurements, possible differences among the results for individual stations (Figure 2.6, AI), and the short overall distance range sampled by the AI events. There are insufficient NI data at epicentral distances less than  $20^\circ$  to investigate any dependence of  $\tau_d$  and  $Q_c$  on  $\Delta$ ; however some NI results at short epicentral distances reveal clear differences between decay parameters measured at individual stations. For the two impact events closer than  $10^\circ$ ,  $Q_c$  values at station 15 are about twice the  $Q_c$  values measured at station 16 (Figure 2.6, NI). In addition,  $Q_c$  values for the NI events show greater variability ( $Q_c = \sim 4000\text{--}12000$ ) at short distances than at large distances ( $Q_c = \sim 7000\text{--}10000$  for  $\Delta > 90^\circ$ ); this is particularly evident in the results for station 14.

$\tau_d$  and  $Q_c$  values on the L1 band for all event types, at all  $\Delta$ , show differences among stations. This is most easily seen in the  $Q_c$  results (Figure 2.6).  $Q_c$  values measured at stations 14 and 16 for moonquakes are typically smaller than the values from stations 12 and 15 at similar epicentral distances. This is also true of the natural impacts at epicentral distances less than about  $90^\circ$  (corresponding to the epicentral distance range for most moonquake observations). Similarly, for the AI,  $Q_c$  on the L1 band appears to be lower at station 14 compared with station 12, although in contrast to the results for moonquakes and NI, the values for station 15 are similar to those at station 14. However the range of epicentral distances spanned by the AI data is more limited than for the other event types.

## 2.4. Results

---

### 2.4.2 Decay Parameters Measured on the Short-Period Channel (SPZ)

The bandwidth covered by the SPZ instrument is wider than that covered by the LP instrument, aiding investigation of any dependence of  $\tau_d$  and  $Q_c$  on frequency. However, the frequency content of events other than SMQs is richer in lower frequencies ( $< 3$  Hz). This results in relatively fewer high quality AI, NI and DMQ events on the SPZ component. This is especially true for DMQs, for which the typically lower magnitudes and overall lower frequency content are responsible for the low number of events recorded on the SPZ channels. The SMQ events, on the other hand, have a frequency content that extends into the 8–10 Hz band resulting in  $Q_c$  estimates for all four bands that cover a wide range of  $\Delta$  ( $\sim 20\text{--}120^\circ$ ).

The low number of AI and DMQ events does not allow the identification of a dependence of the decay parameters on  $\Delta$  or frequency. However, a dependence of  $\tau_d$  and  $Q_c$  on distance and frequency is seen in the NI and SMQ data.

$\tau_d$  shows a correlation with  $\Delta$  on the 2–4 Hz and 4–6 Hz frequency bands for the NI events (correlation coefficients  $R = 0.61$  and  $R = 0.78$  respectively), and for all frequency bands for the SMQ ( $R = 0.45$  for 2–4 Hz, 0.65 for 4–6 Hz, 0.75 for 6–8 Hz and 0.75 for 8–10 Hz).  $\tau_d$  values for NI on the S1 band are twice those on the S2 band, but the dependence on distance is the same within error (Table 2.3).  $\tau_d$  values for SMQ on band S1 are larger than those on all other bands, and the values on the other bands (S2, S3 and S4) are similar to each other. The dependence on distance increases for increasing frequencies (seen as increasing slopes in Table 2.3).

The  $\tau_d$  data result in  $Q_c$  values that show a clear dependence on epicentral distance and frequency (Figure 2.8 and Table 2.3). The slope of the straight-line fits to  $Q_c$  versus  $\Delta$  increases from bands S1 to S2 for the NI, and from S1 to S4 for the SMQ. NI show similar  $Q_c$  values for S1 and S2 at very short distances ( $\approx 7200$ ). The  $Q_c$  values for SMQ at short epicentral distances in bands S1 and S2 are also similar to each other, but lower than those for NI ( $\approx 5800$ ), and they increase for bands S3 and S4.

Finally, there is a marked difference in the SMQ  $\tau_d$  and  $Q_c$  values between station 14 and stations 15 and 16, on the 8–10 Hz band.  $\tau_d$  values are larger by

## 2.4. Results

---

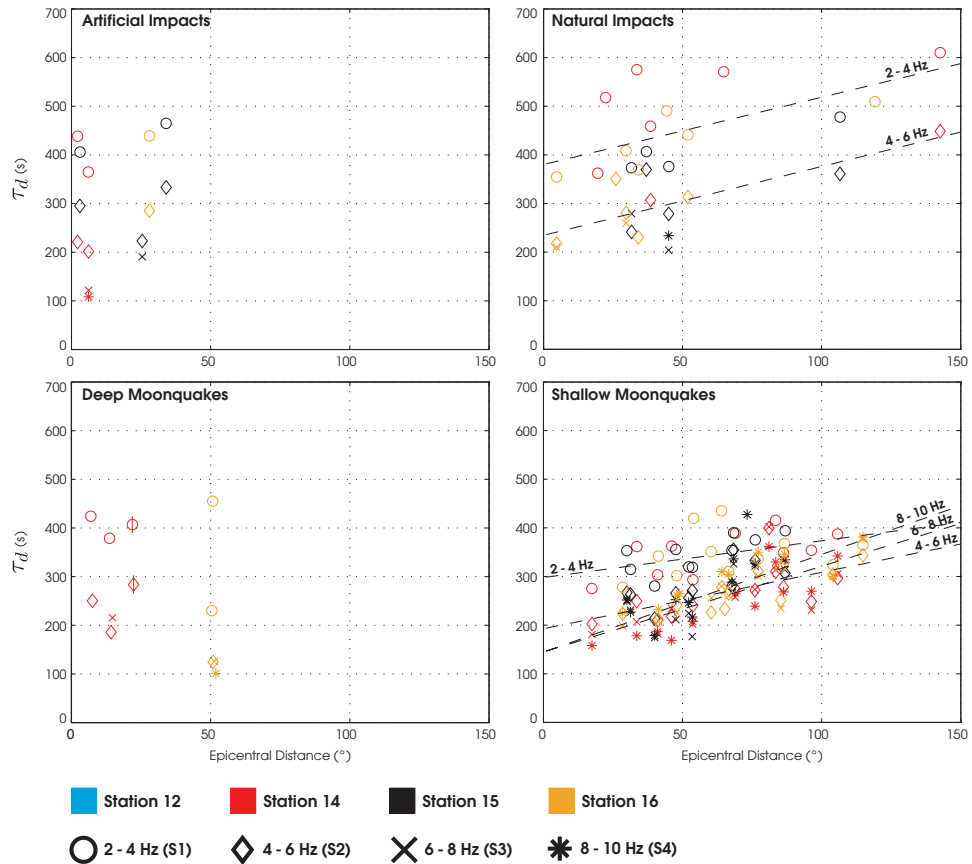


Figure 2.7: Measured  $\tau_d$  for all types of events on the SPZ channel. The colours represent the different stations and the symbols refer to each frequency band. No events were recorded at station 12 due to an early malfunction of the instrument. Robust least-squares fit straight lines showing dependence of  $\tau_d$  on epicentral distance are shown for the two NI lower frequency bands and for all SMQ bands.

## 2.4. Results

---

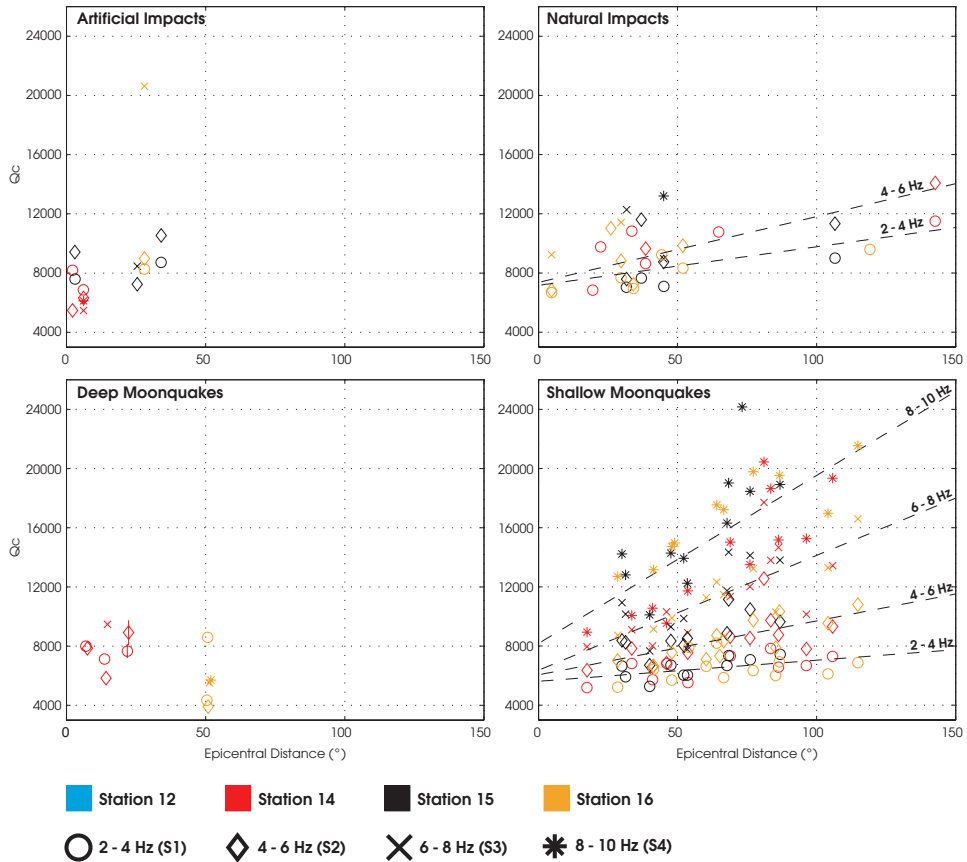


Figure 2.8: Measured  $Q_c$  for all types of events on the SPZ channel. The colours and symbols are the same as in Figure 2.7. Robust least-squares fit straight lines are also shown for NI and SMQ.

## 2.5. Implications

---

$\sim 100$  and  $Q_c$  values are larger by  $\sim 4000$  at stations 15 and 16 compared to station 14. The dependence of  $\tau_d$  and  $Q_c$  on  $\Delta$  for each station is similar.

### 2.4.3 Dependence of Decay Parameters on $\alpha$

I investigated whether the observed coda decay can be better or equally well fit by the more general form of equation 2.3 with  $\alpha \neq 0$ . I used  $\alpha = 1$  and  $\alpha = 2$ , and for each value I refit the coda decay for all events. I compared the RMS misfits of the fits with  $\alpha = 1$  or  $\alpha = 2$  with those for  $\alpha = 0$ . Results show that fits with  $\alpha = 0$  are better, for all event types. I found that using  $\alpha > 0$  generally resulted in values of  $\tau_d$  that are two to three times larger than their value for  $\alpha = 0$ . However for some seismograms, using  $\alpha > 0$  led to unrealistically large  $\tau_d$  and  $Q_c$  values. Importantly, I found that the SPZ dependence of  $Q_c$  on epicentral distance and frequency was robust with respect to the choice of  $\alpha$ . Given these results, and the limitations of the assumptions underlying existing theoretical work for the lunar application, I retain the simplest possible function form for the lunar decay that relies on only one parameter ( $\tau_d$ ).

## 2.5 Implications

The physical significance of  $\tau_d$  and  $Q_c$  is still not fully understood, especially in the lunar context. Theoretical work suggests that for single scatterer models (*i.e.*, weak scattering),  $Q_c$  is an averaged S-wave attenuation parameter, which includes both intrinsic ( $Q_i$ ) and scattering ( $Q_s$ ) attenuations [Sato and Fehler, 1998]. In the case of multiple scatterer models (stronger scattering), numerical and laboratory experiments, as well as theoretical studies indicate that  $Q_c$  corresponds to the S-wave  $Q_i$  (see review in Yoshimoto and Jin [2008]). This assumes that  $Q_c$  is measured at a lapse time larger than the mean free time (defined as twice the time it takes for an S-wave to go from the source to the receiver). However, the dependence of  $Q_c$  on epicentral distance, observed in the short-period NI and SMQ data, is difficult to reconcile with simple geographical and/or depth variations in  $Q_i$ . This suggests a contribution of  $Q_s$  to the observed  $Q_c$ , at least for frequencies larger

## 2.5. Implications

---

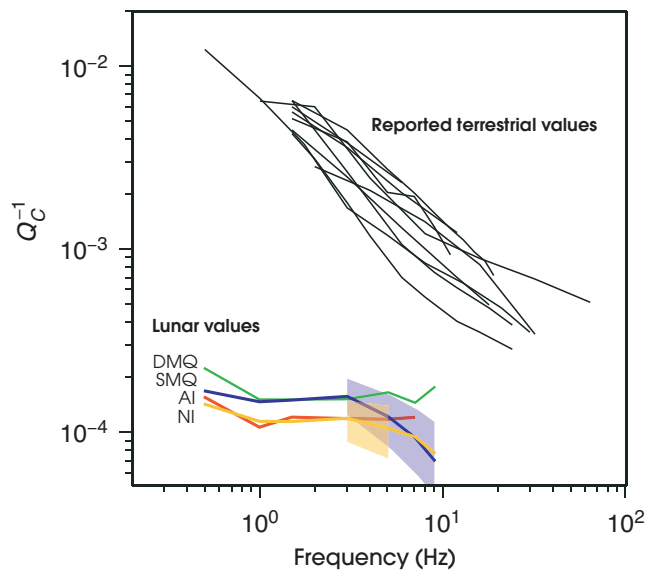


Figure 2.9: Comparison between terrestrial and lunar  $Q_c^{-1}$  values. Lunar values are much lower than terrestrial values (*i.e.*, larger  $Q_c$ ). Lunar mean  $Q_c^{-1}$  values do not exhibit a strong dependence on frequency in the 0.5–4 Hz range, in contrast to the terrestrial data. The blue (SMQ) and yellow (NI) shaded regions show the variations in  $Q_c^{-1}$  due to its dependence on epicentral distance at frequencies larger than 2 Hz.  $Q_c^{-1}$  was plotted (and not  $Q_c$ ) in order to better compare with previously published terrestrial data. Figure modified from Yoshimoto and Jin [2008], with permission from Elsevier.

## 2.5. Implications

---

than 2 Hz. The dependence of  $Q_c$  on epicentral distance could then reflect the fact that the seismic energy will encounter more scatterers along longer path lengths, resulting in increased  $\tau_d$  and  $Q_c$  values. Thus, a major question is what are the relative contributions of  $Q_i$  or  $Q_s$  to the signal recorded in the seismic coda?

The lunar interior is different from the Earth in at least two respects that are important to understanding the observations. First, the relative paucity of volatiles in the lunar interior leads to lower intrinsic attenuation (higher  $Q_i$ ) than on Earth. Studies of the decay of the maximum signal amplitude with distance yield lunar upper mantle S-wave  $Q_i$  values ranging from 4000 at frequencies of 3 Hz to 8000 at 7 Hz [Nakamura et al., 1976; Nakamura and Koyama, 1982], compared with terrestrial values of  $\sim$ 25–500 (e.g., Mitchell [1995]). Second, unlike on Earth, the Moon has a highly fractured megaregolith layer that is global in extent but with regional variations in thickness and structure (e.g., McGetchin et al. [1973]; Thompson et al. [2009]). Thus, scattering can be expected to occur globally in the near-surface megaregolith layer, with regional or local variations in intensity. Scattering in such a global layer is supported by the observations that seismograms for all types of lunar events, from all depths (up to  $\sim$ 1100 km) and all epicentral distances (up to  $150^\circ$ ), exhibit strong scattering. Scattering of seismic energy in the lunar mantle may also be occurring, as on Earth (e.g., Earle and Shearer [2001]), but its seismic signature is likely obscured by the relatively intense scattering in the megaregolith.

Below, I present a scenario that can explain the observations of  $\tau_d$  and  $Q_c$  for different event types, frequencies, epicentral distances and stations. Based on the above discussion, I assume that scattering occurs in the megaregolith layer. Two end-member processes can explain increases in  $\tau_d$  and  $Q_c$  values: the seismic energy encounters (i) more scatterers along its path (higher effective  $Q_s$ ), through either a higher scatterer number-density and/or a longer path, effectively both spreading and redistributing the energy, causing it reach the station over a longer period of time (increasing  $\tau_d$  and  $Q_c$ ); and (ii) a lower intrinsic attenuation (higher  $Q_i$ ) in the scattering layer, increasing the amplitude of the scattered wave arrivals, and effectively increasing  $\tau_d$  and  $Q_c$ . Accordingly, lower  $\tau_d$  and  $Q_c$  values indicate less scattering (lower effective  $Q_s$ ) and/or higher intrinsic attenuation (lower  $Q_i$ ). I note that for direct waves, scattering will defocus the energy, resulting in decreased

## 2.5. Implications

---

amplitudes. Thus high scattering might be expected to imply low  $Q_s$ . However, in the lunar context, scattering continues well after the direct wave arrivals, redistributing the seismic energy, resulting in longer  $\tau_d$ . Thus high scattering implies high  $Q_s$ . This effect can be expected to be even stronger if the scattering layer is also a low velocity layer, as is quite likely for the megaregolith.

I discuss shallow moonquakes and impacts (Section 2.5.1) separately from deep moonquakes (Section 2.5.2), because the distribution of energy entering the scattering layer is likely to be quite different in these two cases, and has implications for the observed  $\tau_d$  and  $Q_c$ .

### 2.5.1 Shallow Events (SMQ, NI and AI)

#### Teleseismic Shallow Events ( $\Delta > 20^\circ$ )

I propose that the seismic energy forming the coda of teleseismic shallow events spends a large proportion of its total travel time in the scattering layer. As such,  $\tau_d$  and  $Q_c$  values are controlled by the scattering layer  $Q_i$ , by the scattering efficiency of the layer (related to  $Q_s$ ), and by the distance travelled, or equivalently the time spent, in the layer. In addition, the low seismic velocities at shallow depths [Garcia et al., 2011; Kovach et al., 1971] will contribute to trapping energy in a near-surface layer. While the depth extent and exact seismic velocity structure of the low velocity near-surface region is unknown, it is reasonable to suppose that it encompasses some or all of the scattering (megaregolith) layer.

For teleseismic events, the most direct path in the scattering layer has a distance proportional to  $\Delta$ . Figure 2.10 shows that increasing  $\Delta$  will increase the time intervals between the arrival of the most direct waves (making up the coda from the first arrival up to its maximum), the partly scattered waves (which travel part of the way in the mantle and enter the scattering layer at some point between the source and the receiver), and the fully scattered waves (which enter the scattering layer at, or near, the source). Assuming similar relative amplitudes between these arriving waves for all  $\Delta$ ,  $\tau_d$  and  $Q_c$  will increase for increasing  $\Delta$ .

Importantly, the energy entering the scattering layer along the source-receiver path does not have a constant amplitude at all points. Seismic waves entering the layer near the source will have a larger amplitude than waves entering the scatter-

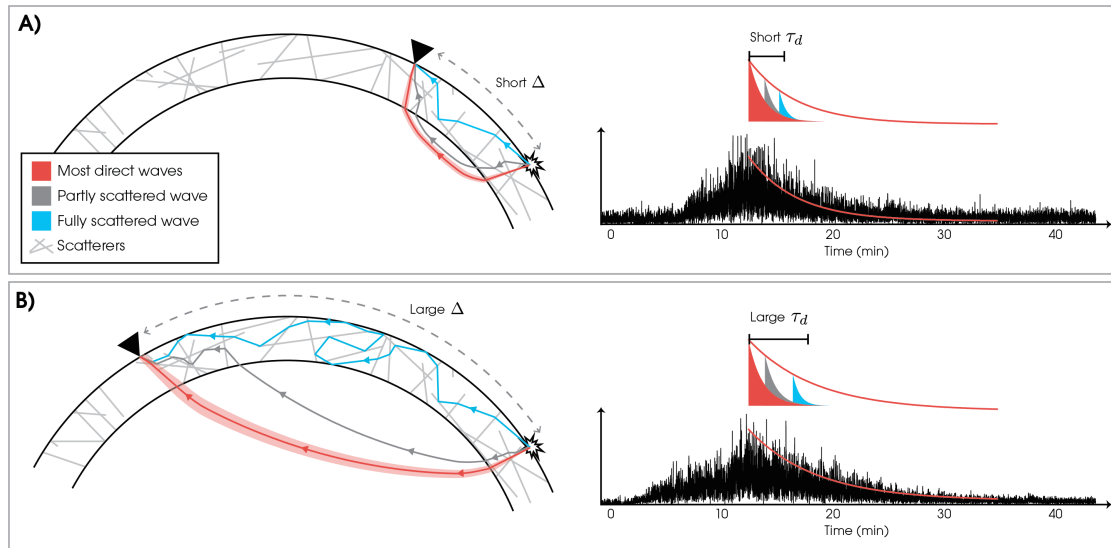


Figure 2.10: Schematic representation of seismic energy propagation showing the effect of epicentral distance on  $\tau_d$ . At short epicentral distances (A), the time intervals between the arrival of the most direct waves (in red, forming the coda up to its maximum amplitude), the partially scattered waves which travel part of the way in the mantle and enter the scattering layer at some point between the source and the receiver (in grey) and the fully scattered waves which enter the scattering layer at, or near, the source (in blue) are small. As the epicentral distance increases (B), these time intervals increase, resulting in larger  $\tau_d$ , for similar relative amplitudes between the waves.

## 2.5. Implications

---

ing layer after travelling some distance in the mantle (Figure 2.11B). Geometrical spreading results in amplitude differences of an order of magnitude or more for the waves entering the scattering layer at different points between the source and receiver. Furthermore, the mantle S-wave  $Q_i$  has been estimated to be  $< 1500$  at depths greater than 300 km at frequencies of 3 Hz [Nakamura et al., 1976]. Thus energy traveling in the mantle and entering the scattering layer close to the receiver will have been attenuated relative to the energy that enters the scattering layer near the source. Energy entering the scattering layer close to the source will spend more time in the layer and will be the most scattered, increasing  $\tau_d$  and  $Q_c$ . In this scenario, we can expect  $\tau_d$  and  $Q_c$  at a given frequency to increase with increasing  $\Delta$ .

The results show an increase in  $\tau_d$  and  $Q_c$  with increasing  $\Delta$  for signals in the S1–S4 frequency bands. Because the increase is seen for all 3 stations for which we have observations, it is difficult to explain in terms of geographical variations in  $Q_i$ , and so I examine the scattering hypothesis above further. Assuming S-wave velocities, ( $V_s$ ), in the scattering layer range from  $\sim 300$  to 3,000 m/s [Garcia et al., 2011], the relevant wavelengths of scatterers are given by  $\lambda = V_s/f$ , where  $f$  is the frequency. For the S4 band, this yields scatterer scale lengths of about 30 - 400m, for the S1 band scale lengths are about 75m to over a km. For the LP bands (for which we observe no increase in  $\tau_d$  and  $Q_c$  with  $\Delta$ ), relevant scatterer scale lengths are on the order of 200m up to several km. Laboratory impact ejecta experiments (e.g., Ryan and Melosh [1998]), suggest that the size-frequency distribution of ejecta blocks in the megaregolith will follow a power-law distribution, with relatively more small scale blocks than large ones. This suggests that high frequency seismic energy will encounter more scatterers compared with low frequency energy, predicting an increase in  $\tau_d$  and  $Q_c$  with frequency at a given  $\Delta$ , as seen in the lunar data. Furthermore, I propose that the lack of dependence of  $\tau_d$  and  $Q_c$  on  $\Delta$  in the LP results (frequencies  $< 2$  Hz) is because at these frequencies scatterer scale lengths are on the order of the scattering layer thickness. If the large scatterers are not distributed uniformly laterally and vertically, or are not present in sufficient number, we might expect no clear dependence of  $\tau_d$  and  $Q_c$  on  $\Delta$ . At the LP frequencies, scattering is still occurring (*i.e.*, the coda waves are still present), but the measured  $Q_c$  reflects a relatively stronger contribution from  $Q_i$ .

## 2.5. Implications

---

than at higher frequencies.

The source depth, above or beneath the scattering and low-velocity layer(s), will also affect the intensity and duration of the recorded scattering. Impact events occur directly above the scattering layer and the seismic energy is scattered at least twice along the way (going through the layer once, travelling in the mantle, and going through the layer again to reach the station, see NI plots on Figure 2.11A). A large part of that energy may also get trapped in the scattering layer, in particular if this layer is also a low-velocity region, and will travel within the layer all the way to the station. I propose that  $\tau_d$  and  $Q_c$  values for impact events are larger than for moonquakes because the seismic energy spends more time overall in the scattering layer. This could also explain the longer rise times for NI compared with SMQ (Figure 2.4). The larger decay values for NI could also be explained by the fact that impact seismic source functions last longer due to the time it takes for the ejecta blanket to fall back down on the lunar surface. Longer source functions would result in larger  $\tau_d$  and  $Q_c$ . Median  $\tau_d$  and  $Q_c$  for shallow moonquakes are also slightly larger than for deep moonquakes. SMQ events occur closer to the scattering layer than DMQ. As such, more SMQ energy will be trapped in the scattering layer on its way to the receiver, increasing the overall amount of scattered energy, and increasing  $\tau_d$ .

The difference in  $\tau_d$  and  $Q_c$  magnitudes between station 14 and stations 15 and 16 on the 8–10 Hz band points to differences in the local structure and/or rock composition surrounding the receivers at those wavelengths. A lower  $Q_c$  (station 14) points to either a weaker scattering, or a higher intrinsic attenuation (lower  $Q_i$ ). Station 14 sits on top of a thick layer of mare basalt, whereas station 15 sits at the edge of a large basin and station 16 overlies crustal ferroanorthosite. This difference in composition and structure could lead to different scattering properties. As such, the scattering characteristics of a signal are not only controlled by the global scattering layer, but also by the local structure near the receivers.

### Local Shallow Events ( $\Delta < 20^\circ$ )

In contrast to teleseismic shallow events, local shallow events defined here as SMQ, NI and AI events having an epicentral distance of  $20^\circ$  or less, have  $\tau_d$  and  $Q_c$  values

## 2.5. Implications

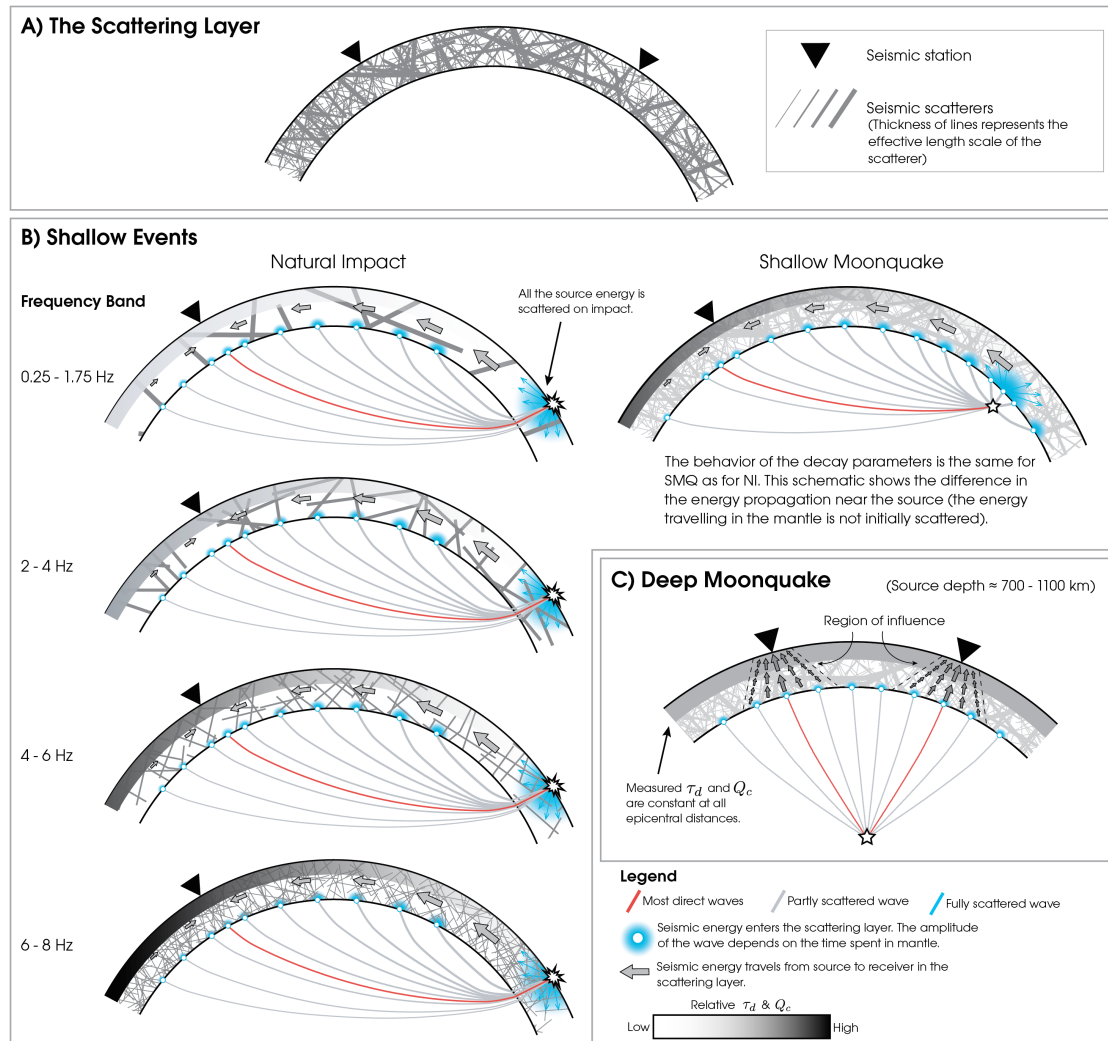


Figure 2.11: See caption on following page.

## 2.5. Implications

---

Figure 2.11: (A) Schematic illustration of the scattering layer. Each line represents a scatterer, and its thickness indicates its effective length scale. A larger scatterer (thicker line) is seen by long-period waves, whereas small-scale scatterers (thin lines) affect higher frequency waves. (B) The signal decay measured at the receiver is dominated by the energy entering the scattering layer with the largest relative amplitude. For NI events (left column), this is the energy trapped in the layer directly after impact. For SMQ occurring below the scattering layer, this is the energy that enters the scattering layer near the source (top right). The relative amplitude of seismic waves entering the base of the scattering layer is shown in blue. For impacts and SMQ, increasing the source-receiver distance ( $\Delta$ ) increases the number of scatterers encountered and for a power-law size distribution of scatterers [Ryan and Melosh, 1998], the effect will be greater at higher frequency (shown for NI in left column). Thus,  $\tau_d$  and  $Q_c$  increase with increasing  $\Delta$  and frequency (gray shading). (C) For DMQ, the energy entering the base of the scattering layer is approximately uniformly distributed over a wide area. Because DMQ magnitudes are small, only energy entering the scattering layer within some region of influence around the receiver is still detectable after scattering.  $\tau_d$  and  $Q_c$  values measured at all  $\Delta$  are similar, and represent the scattering properties of regions surrounding the stations.

that may be controlled dominantly by the local scattering structure surrounding the receivers. An example of the possible effects of local structure is the difference between the  $\tau_d$  and  $Q_c$  values of the two NI events with epicentral distances less than  $10^\circ$ . The two events were recorded at station 15 ( $Q_c = 7882$  on L1) and station 16 ( $Q_c \sim 4200$  on L1) and their locations are shown as crossed yellow circles on the location map (Figure 2.1). Station 15 is slightly to the west of the boundary between Mare Imbrium and Mare Serenitatis, and the local impact event occurred to the south of this boundary. Deep lateral structure related to the margins of these two large basins may have trapped the seismic energy arriving from the south, increasing the decay time of the signal (and increasing  $\tau_d$  and  $Q_c$ ). Station 16 is on the highlands to the south-west of Mare Tranquilitatis, and the impact event hit the surface to the north-east of the receiver. There are no identifiable structures in the vicinity of station 16 that could trap seismic energy as for station 15, potentially explaining the lower  $\tau_d$  and  $Q_c$  values for this particular event.

## 2.5. Implications

---

### 2.5.2 Deep Moonquakes

DMQs have depths of 700–1100 km, and energy propagates from the source regions through the lunar mantle and crust, to the scattering layer. The amplitude of seismic waves reaching a given point at the base of the scattering layer depends on the combined effects of geometrical spreading, intrinsic attenuation and seismic velocity structure of the mantle and crust. This energy is then scattered, and so seismic waves that enter the base of the scattering layer need to have a sufficiently large amplitude to still be detectable by an instrument on the surface. Path lengths traveled by energy between a DMQ source region and the base of scattering layer will vary by less than a factor of about 3 for the epicentral distance range over which we have observations of DMQ ( $\Delta < 80^\circ$ ). Consequently, in the absence of large lateral variations in seismic velocity and intrinsic attenuation, the amplitude of the wave entering the scattering layer will vary by less than an order of magnitude for points along the base of the scattering layer (Figure 2.11C). DMQ magnitudes are small [Latham et al., 1973], and so the amplitude of the wave that reaches any point along the base of the layer is also small. Hence energy entering the scattering layer further from the stations may decay to imperceptible levels before reaching the receivers. The measured  $\tau_d$  and  $Q_c$  are then representative of the properties of the scattering layer in a region surrounding each station (the region of influence). The extent of this region, and hence the measured decay parameters, should be insensitive to the source-receiver distance (Figure 2.11C), but might be expected to increase for larger magnitude DMQs.

No dependence of the decay parameters on  $\Delta$  is observed in the data (Figures 2.5 and 2.6), which is consistent with the above scenario. Source region A001 exhibits the largest number of DMQ in the lunar event catalogue [Latham et al., 1971; Bulow et al., 2005], and contributes the greatest number of DMQ events to the analyses here, so I use it to examine any dependence of the decay parameters on amplitude at a given station. DMQs from source region A001 do not show any dependence of  $\tau_d$  and  $Q_c$  on amplitude (Figure 2.12), but this may simply be due to the low amplitudes, the small amplitude range for most events, and the fact that the recorded amplitudes also include local station effects. While the actual extent of the region of influence is unknown,  $\tau_d$  and  $Q_c$  for band L1 for source region A001

## 2.5. Implications

---

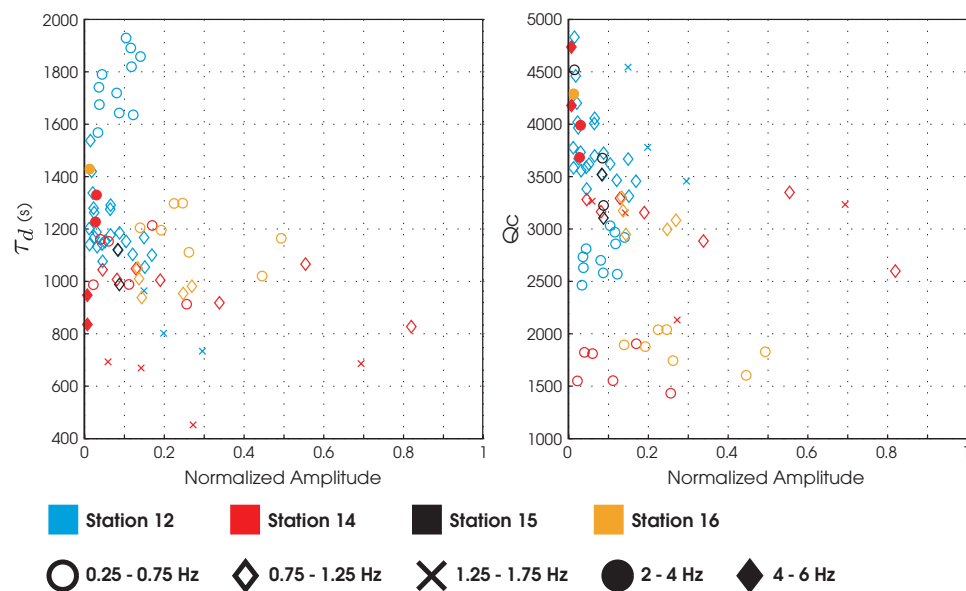


Figure 2.12:  $\tau_d$  and  $Q_c$  values for DMQ events in the A001 source region (same  $\Delta$  for a given station).

## 2.6. Conclusions

---

are larger at station 12 ( $\Delta = 18.2^\circ$ ) than at station 14 ( $\Delta = 22.3^\circ$ ), and station 16 ( $\Delta = 51.2^\circ$ ). This suggests localized differences in the scattering characteristics around station 12, compared with those around station 14, and might offer an upper bound on the size of the region of influence for DMQ type events of similar magnitudes. This limit has to be smaller than the epicentral distance between stations 12 and 14 ( $\Delta = 180$  km). I note that the observation of larger  $\tau_d$  and  $Q_c$  for band L1 at station 12 compared with stations 14 and 16 is supported by my global data set of NI, DMQ and SMQ as summarized in Section 2.4.1, suggestive of lateral variations in scattering properties at scale lengths corresponding to the L1 frequency band.

Scattering of DMQ energy near the source region may also occur. If scattering takes place in the deep Moon, seismic waves entering the near-surface scattering layer will already comprise a long coda (with its own  $\tau_d$ ). This initial  $\tau_d$  would be affected by the strong scattering in the megaregolith, and would be increased even further. However, a higher intrinsic attenuation in DMQ source regions (lower  $Q_i$ , which is plausible due to the temperature increase with depth) would act to mitigate this effect. It is not possible to confirm or deny source-side scattering for DMQ with this data set: one test of source-side scattering might be differences in  $Q_c$  for different DMQ source regions, and I do not observe such differences. It is likely that the DMQ coda are dominated by scattering and intrinsic attenuation in the megaregolith.

## 2.6 Conclusions

The long decay times of lunar seismograms, recorded for all types of lunar events, at all stations, indicate that scattering of seismic energy occurs in a global layer. This layer is likely the near-surface megaregolith, which is global in extent, with recognized regional variations in thickness and structure. Both intrinsic attenuation and the scattering properties of the megaregolith contribute to coda decay times. In addition, low seismic velocities in (and possibly extending below) the megaregolith will focus seismic energy into this scattering layer. While it is not possible to uniquely identify the contributions of intrinsic attenuation and scattering, variations of coda  $\tau_d$  and  $Q_c$  with event type, distance and frequency allow us to identify when

## 2.6. Conclusions

---

the relative contribution of scattering might outweigh that of intrinsic attenuation. The dependence of  $\tau_d$  and  $Q_c$  on epicentral distance at frequencies larger than 2 Hz suggests that  $Q_s$  dominates the coda decay at high frequencies and large distances.

Differences in decay times between shallow events (SMQ and NI) and DMQs indicate that the attenuation and scattering properties of the scattering layer are expressed differently in the seismograms of shallow and deep events. Shallow events show an increase of  $\tau_d$  and  $Q_c$  with increasing source-receiver distances for frequencies larger than 2 Hz. I propose that this is because energy traveling longer distances in the scattering layer encounters more scatterers. This inference is further supported by the observation that  $\tau_d$  and  $Q_c$  also increase with increasing frequency, consistent with the presence of relatively more small-scale versus large-scale scatterers (Figure 2.11B). In contrast, the small magnitude and large depths of DMQs may mean that the seismic energy recorded at the receiver from those deep events samples the scattering layer in a distinct region (region of influence) around the receiver (Figure 2.11C). This hypothesis is supported by the observation that  $\tau_d$  and  $Q_c$  for DMQs are independent of the source-receiver distance, and less than those of shallow events. Differences in  $\tau_d$  and  $Q_c$  for DMQ recorded at stations 12 and 14 suggest that the region of influence for those stations is less than 180 km (the epicentral distance between the two stations).

Local structure can also be important, in particular for signals from local events ( $\Delta < 20^\circ$ ). We see increased scattering in the coda of a NI event recorded close to station 15, compared with one that occurred at a similar distance to station 16, perhaps reflecting the trapping of seismic energy by large scale impact basin-related structures near station 15. Lower  $Q_c$  values in the L1 band for stations 14 and 16, compared to stations 12 and 15, recorded for all event types (Figures 2.6 and 2.12), reflect either relative differences in intrinsic attenuation (at L1 frequencies) or in scattering (at scale lengths of several hundred meters to a few km) between those two groups of stations. Stations 12 and 14 are both located on the southern basaltic plains of Oceanus Procellarum and so the differences in L1 decay times for those two stations point to local differences in structure near the receivers. Stations 14 sits on a crater ejecta blanket (itself overlying the older basaltic layers) and associated low-velocities, and fractured and welded structure might be responsible for these differences in attenuation and scattering properties in the L1 frequency band.

## 2.6. Conclusions

---

In contrast, at higher frequencies (S4),  $Q_c$  values are lower at station 14 than at stations 15 and 16, which once again points to differences in the intrinsic attenuations near the receivers or to relatively less scatterers corresponding to the S4 frequencies at station 14 than at stations 15 and 16.

The results demonstrate that the scattering layer comprises scatterers with a range of length scales, and they indicate that scattering will also be important at frequencies higher than those observed by the APSE experiment. In contrast, recordings of lower frequency signals might yield data that contain minimal scattering and would greatly facilitate the exploration of the Moon's interior. The results and interpretations provide constraints and testable hypotheses for future waveform modeling that includes the effects of very low intrinsic attenuation, intense scattering and near-surface low velocity layer(s) in a small rocky body. Such studies can investigate suites of models that predict seismograms with coda properties that match those reported here from the APSE data set. These in turn can constrain globally averaged and possible regional variations in properties of the scattering layer such as intrinsic attenuation, velocity structure, scatterer size distribution and layer thickness.

## **Chapter 3**

# **Modeling Seismic Energy Propagation in Highly Scattering Environments**

### **3.1 Introduction**

The study of seismic energy propagation in highly scattering bodies is a barely tapped field of planetary seismology research. Scattering of seismic energy occurs when coherent seismic wavefronts are randomly dispersed by a large number of small-scale heterogeneities. In environments with high levels of scattering, this process can obscure the arrivals of waves other than the P- and S-waves and thus limit the use of traditional analysis techniques that make use of body wave arrival times. The best, and only known non-terrestrial, example of this process is observed in the lunar Apollo Passive Seismic Experiment (APSE, 1969-1977) data. The recorded seismic waveforms are characterized by very long durations, by emergent onsets and by the presence of very slowly decaying coda waves. These signals result from the interaction of seismic energy with the various velocity, attenuation and scattering structures within the Moon and as such have the potential to reveal information regarding the lunar interior that is not accessible through more established seismological analyses. I showed in Chapter 2 that the manner in which scattered seismic signals decay can be used to assess first-order properties of the lunar interior structure. My analyses of the APSE data indicated decay properties that are consistent with a shallow scattering layer comprising frequency-dependent scatterer number-densities and scale-lengths. However, these interpretations were restricted in part by the limitations of the APSE instruments (10-bit digitization

### *3.1. Introduction*

---

and narrow bandwidth), but mostly by the lack of understanding of the processes governing seismic energy propagation in highly scattering media. Thus, in order to better appraise the interior structure of the Moon and other highly scattering bodies, we need to first understand the effects of varying velocity, attenuation and scattering structures on seismic signal decay characteristics. In this paper, I address the following general questions: What impact does the seismic wave velocity profile have on the signals' coda (e.g. presence of a crust and of a very low velocity layer, analogous to the surface regolith)? Can the decay properties of the seismic signals be used to assess the various scale-lengths involved in the scattering process (e.g., scattering layer thickness, scale-lengths of scatterers)? Do deep structures like a small core have an impact on the coda wave trains? What happens to the seismic coda when scattering is not restricted to a near-surface highly scattering layer?

I present results from modeling of seismic coda in a highly scattering media, using a modified version of the Monte Carlo simulation method presented in Shearer and Earle [2004], in which a large number of seismic phonons are tracked as they travel through a planetary interior. The phonon method was first used to model the envelopes of seismic waves of local earthquakes with epicentral distances of 30–50 km [Gusev and Abubakirov, 1987]. These quakes exhibit scattering characteristics that are much weaker than, but qualitatively similar to those observed in lunar seismic events. Adapted phonon methods were also used to investigate depth dependent attenuation of coda waves (e.g. Hoshiba [1994]), to study the effect of increasing velocities with depth on the coda shape (e.g. Yoshimoto [2000]), to study the partitioning of wave energy in multiple scattering events (e.g. Margerin et al. [2000]), as well as to model the global short period terrestrial wavefield (i.e. deep Earth scattering, see Shearer and Earle [2004]). However, this method has not been used to simulate and investigate the effects of highly scattering environments such as the Moon on seismic signals, which is the main motivation behind this study. Our chosen modeling method effectively addresses the problem outlined in Nakamura [1977] regarding the synthesizing of seismic signals in highly scattering environments by providing a method to model both the diffusivity of seismic energy (high scattering levels) and simple body wave energy transmission.

I have improved upon the Shearer and Earle [2004] method in two ways that

### 3.1. Introduction

---

are important for highly scattering environments: (i) 2.5-D ray tracing is used for scattered phonons, rather than pure two-dimensional (2-D) ray-tracing, with probabilistic three-dimensional (3-D) heterogeneities. This is important for proper characterization of the scattering. (ii) Predetermined velocity and density heterogeneities can be incorporated directly in the model, in contrast to only stochastic perturbations. This can better characterize site effects due to scattering near the receiver when waveforms from all events undergo similar scattering from the same near-receiver structure.

An important aspect of this method that differs from previous modeling work (e.g. Sato and Fehler [1998]; Przybilla et al. [2009]) is that scatterers are modeled as interfaces, and not as points or small volumes. The orientation of each scatterer, as well as the impedance contrast at the interface, determines by how much the phonons are deviated from their original path (i.e., by how much they are scattered). This method allows us to model the effect of a wide range of impedance contrasts. Other established techniques for modeling scattering (e.g. using the Born approximation) require that the velocity contrasts at the scatterers relative to the background surrounding velocity are small [Sato and Fehler, 1998]. Scattering of seismic energy on the Moon mostly takes place in the near-surface scattering layer, known as the megaregolith. This layer is the product of billions of years of meteorite impacts on the lunar surface [Hörz, 1991]. In that layer, scattering occurs predominantly either at (i) the welded contacts between adjacent ejecta blocks, (ii) the interfaces between blocks of different lithologies (e.g. upper crust vs. upper mantle, major faults bounding large craters and impact basins), (iii) when seismic energy encounters high porosity where interfaces between blocks are not welded. High porosity in the lunar uppermost crust is supported by GRAIL data and the recent work of Wieczorek et al. [2013]. In this context, the impedance contrasts caused by porosity or by adjacent varying lithologies are not always weak.

Our phonon method, dubbed PHONON1D because of its use of one-dimensional (1-D) velocity profiles, is described in detail in Section 3.2. I have benchmarked the code against the TTBox [Knapmeyer, 2004] and the CRFL [Fuchs, 1968; Fuchs and Müller, 1971] packages for travel times, as well as against the CRFL package for amplitudes for synthetics computed in non-scattering environments (see Section 3.3).

### 3.2. Methodology

---

The goal of this work is not to produce synthetics that match the scattered properties of the APSE data. Our purpose is to build an understanding of the general consequences of interior structures of highly scattering bodies, like the Moon, on surface seismograms. Accordingly, I used the PHONON1D method to generate synthetic seismograms from shallow and deep sources in 16 different interior models with varying velocity, attenuation and scattering properties. The resulting highly scattered waveforms can be characterized by their decay times ( $\tau_d$ ) and the frequency-dependent equivalent decay factor ( $Q_c$ ). I describe in Section 3.4 the processing steps I followed to analyze the decay properties of the synthetic signals. I then present and compare examples of synthetic traces and decay properties for all the different models, and I follow with discussions on the effect of each model parameters (Section 3.5).

## 3.2 Methodology

In the PHONON1D method, background P- and S-wave velocities ( $v_p$  and  $v_s$ ), density ( $\rho$ ), scattering probabilities ( $p_{sc}$ ) and intrinsic attenuations ( $Q_i$ ) are prescribed from 1-D (i.e., depth-dependent) models. The phonons travel in a 2-D disk (i.e., a sagittal plane), and at any given time a phonon's position is specified by its depth ( $z$ ) and epicentral distance ( $\Delta$ ). In order to capture the 3-D nature of scattering, randomly oriented scatterers can scatter phonons out of the plane of the 2-D disk by altering their azimuthal angle ( $\phi$ ). In this case, only the projection of the phonons' trajectories onto the 2-D disk are recorded. This method assumes longitudinal symmetry of the background models and the statistics of the scattering, but allows us to model longitudinally scattered energy while only needing to track phonons on a 2-D disk.

### 3.2. Methodology

---

#### 3.2.1 Model Geometry

The phonons travel in a disk of radius  $R_M$ , where  $R_M$  is the radius of the planetary body under study. I use lunar-like dimensions (radius  $R_M = 1737$  km) in this work, mostly to save on computational requirements (the larger the body, the greater the number of phonons that have to be released), but also because the lunar seismic dataset is to date the only one showing evidence of such high scattering intensity. Each phonon is released from a source located at  $\Delta = 0^\circ$ , at a specified source depth  $z_s$ . At each time step, the phonon's depth ( $z$ ), epicentral distance ( $\Delta$ ), and out-of-the-disk azimuth ( $\phi$ ) are recorded.  $\phi$  is initially set to  $0^\circ$  and changes only through the phonon's interaction with a scatterer. Such interactions can add an out-of-the-plane (longitudinal) component to the phonon's trajectory. In that case, for each time step, I project the phonon's path increment back onto the transmission plane such that only the colatitudinal ( $d\Delta$ ) and radial ( $dz$ ) components of displacement are recorded. For example, a phonon with an instantaneous azimuth of  $90^\circ$  (or  $270^\circ$ ) has no colatitudinal displacement (i.e. it remains at a constant  $\Delta$  over that time step, and until it is scattered again). This approach is justified by the assumption of longitudinal symmetry. In this context, any phonon that leaves the transmission plane ( $\phi \neq 0$ ) is assumed to be replaced by a phonon entering the plane from the opposite direction. Thus, any phonon with a non-zero azimuth can be considered equivalently as scattered energy that enters or exits the plane. This aspect of the model is required to capture the 3-D nature of scattering. Non-scattered phonons have a constant  $\phi = 0^\circ$  and they propagate purely in the transmission disk (2-D propagation). The model geometry is illustrated in Figures 3.1 and 3.2.

In a sphere, out-of-plane energy will sample velocities at a different radius than energy projected back into the plane of the 2-D disk. This is important if the energy travels a large distance out of the plane, and/or if the curvature of the spherical shell at that radius/depth is large, *i.e.*, the difference between the projected in-plane and the out-of-plane radii and hence the difference in velocities increases with depth. However, one can minimize this effect by only using small time steps (short distances) before re-evaluating the phonon's velocity. In this case, the phonon will travel a maximum distance of 10 km out of the plane (and typically only tens to

### 3.2. Methodology

---

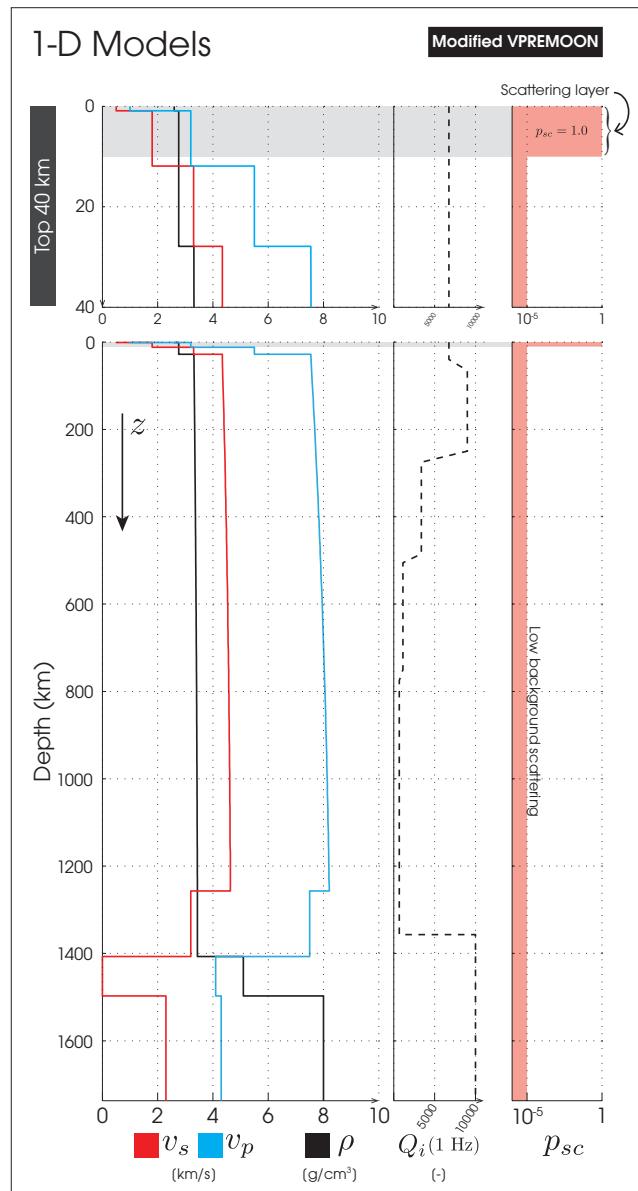


Figure 3.1: See caption on following page.

### 3.2. Methodology

---

Figure 3.1: Example of a 1-D layered model: P- and S-wave velocities ( $v_p, v_s$ ), density ( $\rho$ ), intrinsic attenuation for 1 Hz waves ( $Q_i(1 \text{ Hz})$ ), and the scattering probability ( $p_{sc}$ ). The modified VPREMOON model shown here combines the crustal and mantle velocities from Garcia et al. [2011] with the core velocities from Weber et al. [2011]. This example model has a 10 km thick scattering layer ( $p_{sc} = 1$  near surface) and low overall background scattering ( $p_{sc} = 10^{-5}$  elsewhere). The top plot shows an expanded view of the top 40 km.

hundreds of meters given the distribution of distances between scatterers) before I reassess its radial position and the corresponding velocity. This results in a maximum error in radius of 10 km, if the phonon travels directly perpendicular to the transmission disk ( $\phi = 90^\circ$ ), and very close to the core. This error decreases dramatically at shallower depths, and is negligible at depths throughout the lunar crust and mantle. In this work, most of the scattering occurs within the megaregolith layer, and for models that include background scattering beneath the main scattering layer, the background scattering is limited to depths shallower than 1000 km.

#### 3.2.2 Velocity Profiles

The velocity profiles are specified as individual layers of up to 10 km thickness, separated by interfaces at which the layer properties (wave velocities, intrinsic attenuations, density, scattering probability) are set. The properties of each layers are defined at the overlying interface. Layers of 0 km thickness define sharp boundaries (e.g., crust-mantle and core-mantle boundaries).

I applied the exact Earth flattening transformation to each model interface [Bhattacharya, 1996, 2005]:

$$r/R_M = e^{-z_f/R_M} \quad (3.1)$$

$$v_p = (r/R_M)v_p^*, \quad v_s = (r/R_M)v_s^* \quad (3.2)$$

$$\rho = (R_M/r)^{p-2}\rho^* \quad (3.3)$$

where  $r$  is the distance from the center of the planetary body to the interface,  $R_M$  is the radius of the planetary body,  $z_f$  is the transformed depth coordinate,  $v_p^*$  and  $v_s^*$  are the original P- and S-wave velocities,  $v_p$  and  $v_s$  are the transformed P- and

### 3.2. Methodology

---

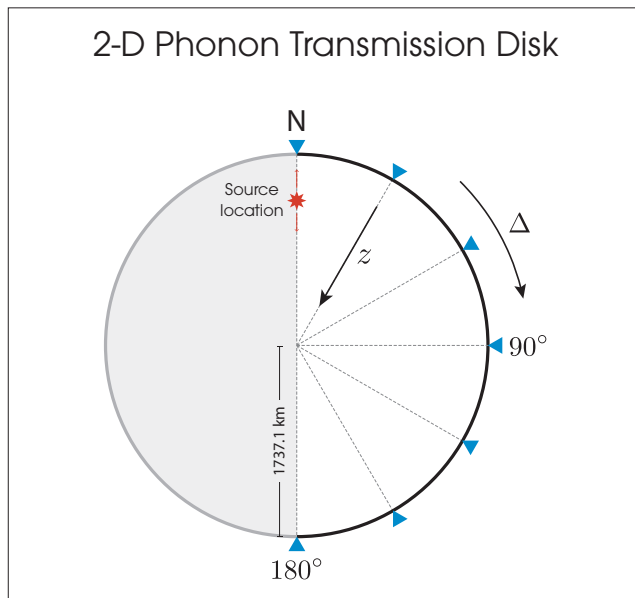


Figure 3.2: Phonons travel in a 2-D disk of radius  $R_M$  ( $R_M = 1737.1$  km). The phonons' depth ( $z$ ) and epicentral distance ( $\Delta$ ) are tracked at each time step. Phonons that reach the surface are recorded by receivers (blue triangles) spaced at regular intervals along the surface away from the source (located at  $\Delta = 0^\circ$ ). Phonons are allowed to travel to distances greater than  $180^\circ$ . They are however reflected back into the  $0$ - $180^\circ$  half-disk if they reach the surface.

### 3.2. Methodology

---

S-wave velocities,  $\rho^*$  and  $\rho$  are the original and transformed densities, and  $p$  is an arbitrary constant that varies with wave type [Bhattacharya, 1972, 1996]. In this work,  $p$  is set to  $-2$ , as in Bhattacharya [2005].

The flattening transformation results in a singularity at the core ( $r = 0$  km). To avoid numerical error during the calculation of the phonon path, I assume that any phonon that travels to within  $0.1$  km of the center of the planetary body travels through the center point, and I adjust the travel time ( $dt = 0.2/v_{core}$ , where  $v_{core}$  is the seismic wave speed in the core in km/s) and epicentral distance ( $d\Delta = \pi R$ ) accordingly.

#### 3.2.3 Seismic Source

I use a modified simple analytical two-sided pulse [Dahlen, 2005] as a source function for quakes (source depth  $z_s > 0$  km), defined as:

$$m(t) = -4\pi^2 P_0^{-2} (t/3 - P_0/2) e^{-2\pi^2(t/3P_0-1/2)^2}, \quad (3.4)$$

where  $m$  is the source function,  $t$  is time,  $P_0 = 4\Delta t$  and  $\Delta t$  is the signal sampling interval. The equation was modified from the original in order to introduce more low frequency energy. The focal mechanisms of non-terrestrial quakes are still poorly understood, and so I use a circular radiation pattern in this modeling work. However, the radiation pattern could be adjusted to fit any particular focal source. For a circular radiation pattern, the release angle is a uniform random number between  $-\pi/2$  and  $\pi/2$ , where  $0$  is horizontal,  $-\pi/2$  is upward, and  $\pi/2$  is downward. The phonon's polarity at the source is randomly determined based on a energy partitioning ratio of 1:10:10, for P-, SV- and SH-waves respectively [Boatwright and Fletcher, 1984]. In the case of impact events ( $z_s = 0$  km), the source function is a delta function with release angles randomly selected between  $0$  and  $\pi/2$  (downward direction only). Only P-wave energy is released for such events, i.e., the energy partitioning ratio is set to 1:0:0. The initial ray parameter ( $p$ ) is set at this stage, based on the release angle, polarization and corresponding velocity at the source depth. If the scattering probability ( $p_{sc}$ ) is set to 0, then  $p$  remains unchanged as the phonon travels throughout the Moon.  $p$  will change if the phonon is scattered by a non-horizontal scatterer. Sources used for the synthet-

### 3.2. Methodology

---

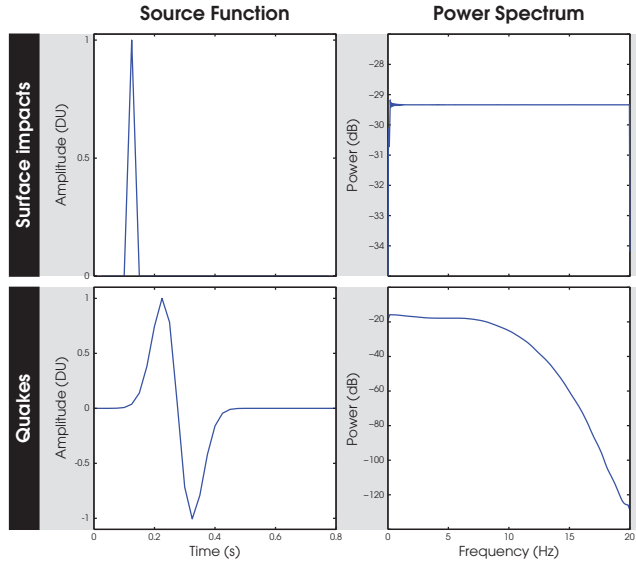


Figure 3.3: Source functions, in digital units (DU), used in the modeling for both impact events (top) and quakes (bottom). The right plots are the corresponding power spectra. A sampling frequency of 40 Hz was used throughout.

ics shown in the modeling section (Section 3.4) are presented in Figure 3.3, along with the corresponding power spectra. I used a sampling frequency of 40 Hz (i.e.  $\Delta t = 0.025$  s) for all synthetic signals presented in this article.

#### 3.2.4 Scattering Layers

If a phonon reaches a layer in which the scattering probability is greater than 0 ( $p_{sc} > 0$ ), it will travel within that layer, from scatterer to scatterer, until it reaches the next velocity interface or until it is sent back to the initial interface if it is back-scattered. The distance between scatterers ( $\delta_{sc}$ ) can be set to a constant value (e.g., I use 10 km for global background scattering), or can be stochastically selected from a power-law probability distribution ( $\delta_{sc}^{-n}$ ) where small inter-scatterer distances have a higher probability of occurrence than large distances (as in Figure 3.4). A power-law distribution for megaregolith blocks is motivated by the heterogeneity length-scales generated by impactors of different sizes (e.g. O’Keefe and Ahrens

### 3.2. Methodology

---

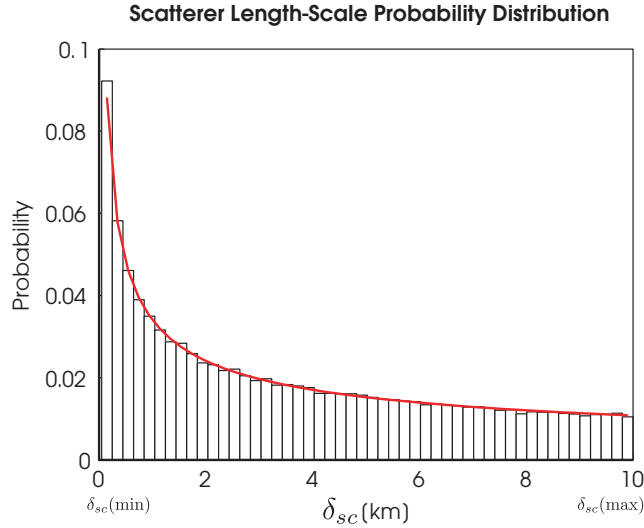


Figure 3.4: Scatterer length-scale probability distribution. The distance a phonon will travel between two consecutive scatterers is randomly picked from the power law distribution plotted above, such that a phonon will travel a greater number of short distances ( $d_{sc}(\min)$ ) than large distances ( $d_{sc}(\max)$ ).

[1987]). In this work  $n$  is always equal to 0.5. Further investigations could study the effect of various  $n$  values, or different length-scale probability distributions (e.g. uniform distribution, only one  $\delta_{sc}$  values, etc.)

Once a phonon reaches a scatterer, it is scattered, or not, based on the scattering probability. Let  $r_x$  be a random number between 0 and 1 taken from an uniform distribution, where different subscripts,  $x$ , indicate different random numbers as described below. If  $r_1 > p_{sc}$ , the phonon is not scattered; if  $r_1 < p_{sc}$ , scattering occurs. In that case, a random scatterer orientation and velocity/density perturbations are generated and the phonon will be reflected or transmitted with a probability based on the reflection/transmission coefficients as for conventional ray theory at a solid-solid interface (Figure 3.5B, and section 3.2.5). The orientation of the scatterer (dip between 0 and  $\pi/2$ , where 0 is locally horizontal and  $\pi/2$  is vertical, and strike between 0 and  $2\pi$ ), as well as the magnitude of the perturbations ( $\pm r_2 \delta v_{p/s}$  and  $\pm r_2 \delta \rho$ , where  $\delta v$  and  $\delta \rho$  are the maximum change in velocity and density at the scattering interface, see Figure 3.5B) will define the orientation

### 3.2. Methodology

---

of the scattered phonon via its incident and azimuth angles. In my models the orientations of the scatterers are selected such that the vectors normal to the scattering interfaces are uniformly distributed (strike is defined as  $r_3 2\pi$ , and the dip as  $\sin^{-1} r_4$ ). Also, the maximum  $\delta v$  and  $\delta \rho$  perturbation levels are kept equal and is referred to as  $\delta_{v,\rho}$ . Once the phonon has interacted with the scatterer, it travels a new random distance  $\delta_{sc}$  to the next scatterer. If  $\delta_{sc}$  is larger than the distance between the phonon and the next velocity interface, the phonon travels directly to the velocity interface. Because of the 3-D geometry of the scatterers, and depending on the phonon's incident and azimuthal angles, scattering can convert the phonon's polarity to P-, SV- or SH- energy (e.g., Figure 3.5B). The transmission and reflection coefficients are calculated with the same equations that govern the behaviour of phonons at regular interfaces (next section).

In the modeling work presented in Section 3.4, the scattering probability in the scattering layer ( $p_{SL}$ ) is always set to 1, such that phonons will always interact with the scatterers. In this case, the intensity and overall direction of scattering are controlled by the impedance contrast at the scatterer (i.e. the differences in velocity and density between the scatterers and the background values,  $(\delta_{v,\rho})$ ). As the average impedance contrast approaches 0 ( $r_2 \delta_{v,\rho} \rightarrow 0$ ), most phonons will be scattered forward (transmission is favored over reflection) with only a small deviation from their original path, regardless of the orientation of the scatterers. Scattering outside of the near-surface scattering layer can be set by setting the global scattering probability ( $p_G$ ) to a non-zero value. Global scattering is limited to depths shallower than 1000 km in the models presented in section 3.4.

#### 3.2.5 Regular Velocity Interfaces

When a phonon reaches an internal boundary, the likelihood that it reflects or transmits in a particular polarization is proportional to the square of the amplitude reflection or transmission coefficient normalized by the sum of the squares of all coefficients. A random number is generated to determine the state of the scattered phase. The phonon will then travel to the next interface if the layer's scattering probability is 0 ( $p_{sc} = 0$ ), or to the next scatterer, if  $p_{sc} > 0$ .

The coefficients are calculated based on the incoming phonon's incident angle

### 3.2. Methodology

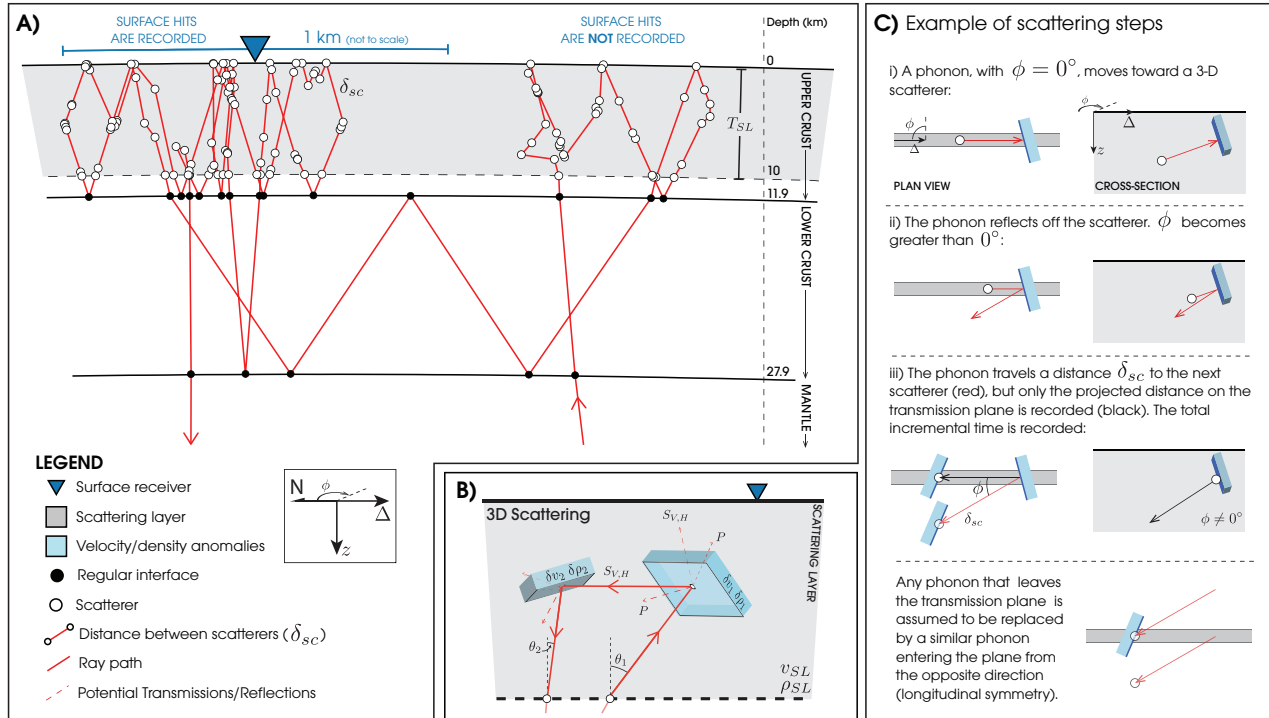


Figure 3.5: A) Example of a scattered ray path in a 10 km thick surface scattering layer. The red line shows the path of the phonon as it enters and leaves the scattering layers. The white dots represent the 3-D scatterers. Inset shows angle  $\phi$  which is non-zero when the phonon has an out-of-plane component. B) Randomly oriented 3-D scatterers, represented here as interfaces with different impedance values from the background values. The probability that the incident ray will be reflected or transmitted, as P, SV or SH energy, is proportional to the square of the reflection/transmission coefficient. Due to the 3-D nature of the scatterer, the phonon can acquire an out-of-the-plane component ( $\phi \neq 0^\circ$ , not shown here). C) Example scattering steps showing a change in the azimuthal angle ( $\phi$ ).

### 3.2. Methodology

---

and polarity. Coefficients for solid-solid interfaces are based on Aki and Richards [2002], whereas those for the free-surface reflections and solid-liquid interfaces come from Ben-Menahem and Singh [2000]. The explicit form for the coefficients is given in Appendix A. Benchmarking of wave amplitude with the CRFL package (Section 3.3) showed that results are better when energy is conserved rather than amplitude at the interfaces. Hence, I use the square of the amplitude coefficients, normalized by the sum of the squares.

All coefficients acquire an imaginary component if any of the transmission or reflection angles are supercritical ( $v_{(p,s)}p > 1$ , where  $p$  is the ray parameter). In this case, I set the coefficient(s) with the supercritical angle to 0 (based on Ben-Menahem and Singh [2000]) and use the moduli of the other complex coefficients.

#### 3.2.6 Surface Recorders

Seismometers are distributed at specific intervals along the surface and record the radial, transverse, and vertical ground displacements each time a phonon comes within a prescribed distance, set to 1 km in this work, from a receiver. I correct for time if the phonon does not hit the surface directly beneath the receiver (Figure 3.6). The applied correction,  $\Delta t$ , is:

$$\Delta t = \frac{\Delta L}{v} = \frac{\Delta x \sin \theta}{v} = p\Delta x, \quad (3.5)$$

where  $\Delta L$  is the additional distance the phonon would have travelled if it had hit the surface directly beneath the receiver,  $v$  is the wave speed,  $\Delta x$  is the distance between the receiver and the arrival position of the phonon on the surface,  $\theta$  is the ray incident angle, and  $p$  is the ray parameter.  $\Delta t$  is negative when the phonon hits the surface before the receiver (Figure 3.6A) and positive when it hits the surface past the receiver (Figure 3.6B). The resulting  $\Delta t$  is also used to calculate the correction to the phonon's attenuation.

### 3.2. Methodology

---

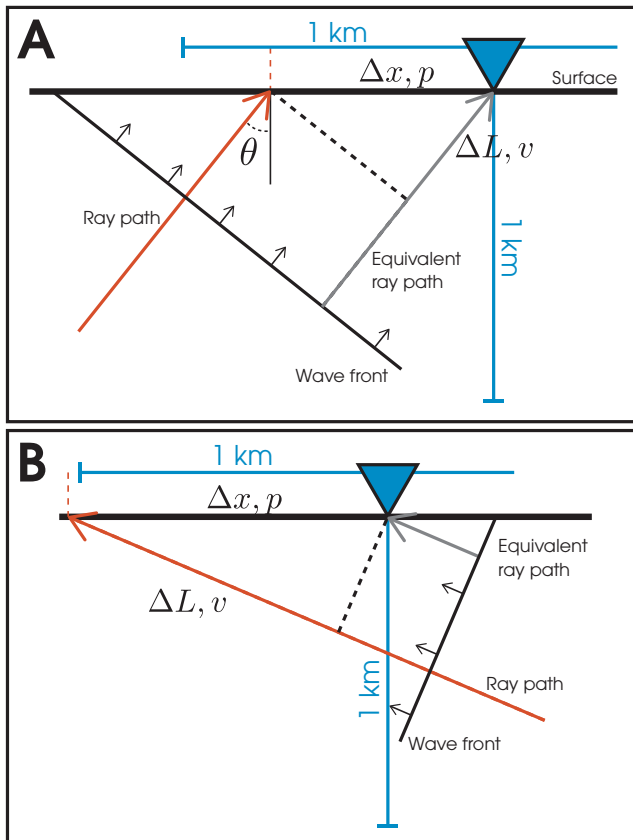


Figure 3.6: All phonons that pass within 1 km horizontally (A) or vertically (B) of a receiver before hitting the surface are recorded, whether they hit the surface within 1 km of the receiver (A), or not (B). In all cases, a time correction ( $\Delta t$ ) is applied. I assume that the phonon's path (red arrow) is perpendicular to the corresponding planar wavefront. This phonon travels a distance that is different by  $\Delta L$  km from the distance travelled by a similar phonon (gray arrow) hitting the surface directly underneath the receiver at a velocity of  $v$  km/s. The resulting time difference ( $\Delta t$ ) is equal to the horizontal slowness ( $p$ ) multiplied by the distance difference at the surface ( $\Delta x$ ) and must be subtracted or added from the arrival time of the phonon that reaches the surface away from the receiver.

### 3.3. Modeling Method Benchmarking

---

#### 3.2.7 Intrinsic Attenuation

I calculate the attenuation of the phonon's amplitude as follows:

$$A(\omega) = A_0 e^{-\omega t^*}, \quad (3.6)$$

$$t^* = \sum \frac{\Delta t}{Q_i(z)} \quad (3.7)$$

where  $A$  is the recorded amplitude at time  $t$ ,  $A_0$  is the phonon's initial amplitude (typically 1 digital unit (DU)),  $\omega$  is the angular frequency, and  $Q_i(z)$  is the depth-dependent intrinsic attenuation factor. I track each phonon's  $t^*$ , which is the sum of all time increments travelled divided by the attenuation factor ( $Q_i$ ) at the depth at which a given travel time increment was spent. For each time step, I record the incremental time spent in a layer with a given  $Q_i$ , and  $t^*$  is the sum of these incremental attenuations.

## 3.3 Modeling Method Benchmarking

As there are no standard numerical benchmarks against which to compare my scattering phonon code, I benchmarked the travel times and amplitude of synthetic signals generated in non-scattering environments. The assumption is that synthetics generated in highly scattering media will have coda with realistic rise and decay characteristics if the amplitudes and times for non-scattered signals have been shown to be appropriate.

I benchmarked the PHONON1D code against the TTBox package [Knapmeyer, 2004] for travel times, and against the reflectivity CRFL code [Fuchs, 1968; Fuchs and Müller, 1971] for both travel times and wave amplitudes. The PHONON1D synthetics match the TTBox and CRFL travel times, for both terrestrial (Figure 3.7A) and lunar (Figure 3.7B) models. Wave amplitudes (Figure 3.7B and 3.7C) compare well for direct waves, but small discrepancies between synthetics from the PHONON1D and CRFL codes are seen at larger times, after the seismic energy has undergone multiple reflections and refractions. I briefly explain below why these discrepancies arise and why the benchmarking results indicate that this code is adequate to be used for its intended purpose of computing synthetics in highly

### 3.4. Modeling Approach

---

scattering media.

The reflectivity method allows a quick estimation of the reflected and transmitted wave field as a function of frequency, ray parameters and distances [Fuchs, 1968]. The CRFL code was constructed using wave theory in layered media, which is intrinsically different from the PHONON1D approach, itself based on generalized ray theory. For example, CRFL computes all wave phase shifts at interfaces, whereas PHONON1D only tracks the 90° shifts occurring at caustic points (e.g., I do not track diffuse waves). I chose to not implement extensive phase shift tracking in order to keep the computation costs to a minimum. Nonetheless, I have opted to benchmark my code with CRFL because it allows us to compare synthetics at higher frequencies than other codes easily allow (e.g. SPECFEM, MINEOS). It is thus reasonable to expect an imperfect match between synthetics from both codes, especially for more complicated velocity profiles (e.g. terrestrial profiles vs. these simple lunar profiles). The criteria I used to decide if benchmarking was satisfactory were: (i) good visual fit of travel times, and (ii) good visual fit of primary wave amplitudes. All benchmarking runs met these two criteria.

The PHONON1D code was not built to study seismic waves in a non-scattering environment. CRFL, or other packages, are better suited to do so. The code's main purpose is to study the propagation of seismic energy in highly scattering media at larger frequencies (up to  $\sim 10$  Hz in this work). In such an environment, most of the non-primary wave types (PP, SS, SP, PcS, and so on) will be very low amplitude and are hidden by the P- and S-wave scattered coda, as observed in the APSE data.

## 3.4 Modeling Approach

Using the PHONON1D code, I computed synthetic signals in 16 distinct highly scattering planetary interiors. I present this modeling work and the results in this section. I focused my investigations on 7 different model parameters: specific 1-D velocity and density profiles, the thickness of the near-surface scattering layer ( $T_{SL}$ ), the maximum velocity and density perturbation levels at each scatterer ( $\delta_{v,\rho}$ ), the reference intrinsic attenuation ( $Q_i(1 \text{ Hz})$ ), the intrinsic attenuation frequency dependence ( $Q_i(f)$ ), the probability of low-level global scattering ( $p_G$ ), as well as the minimum and maximum scatterer length-scales ( $\delta_{sc}$ ). Most of the

### 3.4. Modeling Approach

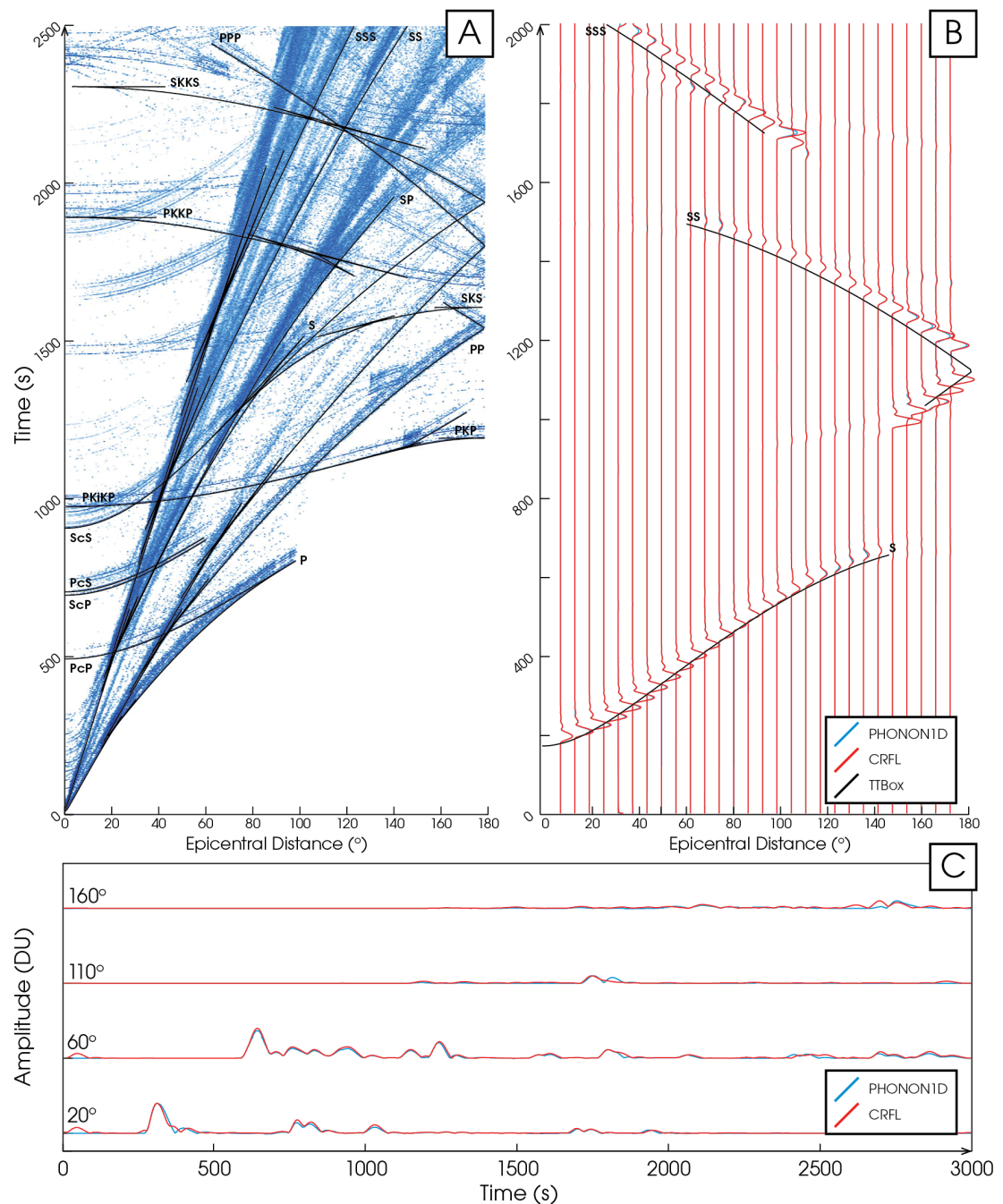


Figure 3.7: See caption on following page.

### 3.4. Modeling Approach

---

Figure 3.7: A) PHONON1D synthetics (blue) vs. TTBox travel times (black), for a PREM model, with a 100 km depth point-source. The logarithmic of the wave amplitudes is plotted in order to show weaker wave arrivals at later times. I only show travel times that TTBOX can compute (i.e. not all multiple reflection phases at later times are identified). B) Comparisons between PHONON1D traces (blue) and CRFL traces (red), showing the transverse component (no P-wave energy) in the 0.10-0.15 Hz frequency band. This is for a simple two-layered Moon, with a 700 km depth point-source. Black lines are TTBOX arrival times. C) Comparisons between PHONON1D traces (blue) and CRFL traces (red), for a PREM model, with a 100 km depth source, showing the vertical component in the 0.10-0.15 Hz frequency band. The PREM model has many interfaces and the discrepancies between the two codes get larger at larger times (e.g. 160°). Note for that both B and C, CRFL plots on top of the phonon code traces, so the absence of blue means a good fit.

velocity profiles used are very simple, the majority having constant P- and S-wave velocities throughout the body. Some of these velocity profiles are somewhat unrealistic, but were chosen for their simplicity and to allow us to easily investigate the individual effects of each model parameter on the seismic coda.

The parameters for all models are outlined in Table 3.1. Figures 3.1 and 3.8 show the five 1-D velocity and density profiles used. Model A is defined as the baseline model, and all other models implement simple variations from it. Other models have been grouped using sequential model names (e.g. C1, C2 and C3) in order to indicate which models are used to demonstrate the effect of a specific velocity, attenuation or scattering structure on the coda. Note that the background intrinsic attenuation factor,  $Q_i(f)$ , is high when compared to terrestrial values (i.e. much lower attenuation levels), but this is necessary to obtain synthetics with long scattered coda. Such high  $Q_i$  values can be expected in very dry planetary environments (e.g. Latham et al. [1970a], Nakamura et al. [1976]).  $Q_i(f)$  is kept constant at 2000, 4500 or 6500 in most models, but increase with increasing frequencies in models C3 and F (Figure 3.9).

I computed synthetics for events at three distinct depths: surface events ( $z_s = 0$  km), shallow events ( $z_s = 30$  km), and deep events ( $z_s = 1000$  km). These are analogous to surface impacts, lunar shallow quakes and lunar deep quakes, respectively. The resulting decay properties of the shallow events are very similar to these of the

### 3.4. Modeling Approach

---

Table 3.1: Models investigated in this study.  $T_{SL}$  is the scattering layer thickness,  $\delta_{v,\rho}$  is the maximum velocity and density perturbation level at each scatterer, and  $Q_i(1 \text{ Hz})$  is the reference intrinsic attenuation. The different  $Q_i(f)$  styles are plotted on Figure 3.9.  $p_G$  is the low-level global scattering probability, and  $\delta_{sc}$  sets the minimum and maximum scatterer length-scales, as defined in Figure 3.4. Model A is the baseline model, with constant P- and S-wave velocities, a scattering layer thickness of 30 km, maximum velocity and density perturbations at the scatterers of  $\pm 0.75 \%$ . For model C3,  $Q_i = Q_i(f, z)$  and  $Q_i(1 \text{ Hz})$  is depth-dependent and is plotted on Figure 3.1.

Model	1-D Velocity Model	$T_{SL}$ [km]	$\delta_{v,\rho}$ [%]	$Q_i(1 \text{ Hz})$ [-]	$Q_i(f)$ style	$p_G$ [%]	$\delta_{sc}$ [km] min. max.
<b>A</b>	Constant Velocity	30	0.75	4500	1	0	0.05 10
<b>B</b>	Constant Velocity	15	0.75	4500	1	0	0.025 5
<b>C1</b>	Crust	30	0.75	4500	1	0	0.05 10
<b>C2</b>	VLVL	30	0.75	4500	1	0	0.05 10
<b>C3</b>	VPREMOON	30	0.75	$Q_i(z)$	2	0	0.05 10
<b>D1</b>	Constant Velocity	5	0.25	4500	1	0	0.05 10
<b>D2</b>	Constant Velocity	5	0.75	4500	1	0	0.05 10
<b>D3</b>	Constant Velocity	5	0.95	4500	1	0	0.05 10
<b>D4</b>	Constant Velocity	60	0.25	4500	1	0	0.05 10
<b>D5</b>	Constant Velocity	60	0.75	4500	1	0	0.05 10
<b>D6</b>	Constant Velocity	60	0.95	4500	1	0	0.05 10
<b>E</b>	Solid Core	30	0.75	4500	1	0	0.05 10
<b>F</b>	Constant Velocity	30	0.75	4500	2	0	0.05 10
<b>G1</b>	Constant Velocity	30	0.75	2000	1	0	0.05 10
<b>G2</b>	Constant Velocity	30	0.75	6500	1	0	0.05 10
<b>H</b>	Constant Velocity	30	0.75	4500	1	0.01	0.05 10

### 3.4. Modeling Approach

---

surface impacts. This is a result of the sources being located in, or very near the surface scattering layer in both cases. Thus, I only present the synthetic traces and decay analysis results from the surface impacts and deep events. As mentioned earlier, I used lunar-like dimensions for this particular work (planetary radius of 1737 km). However, this method could be applied to much larger (i.e. Mars) or smaller (e.g. asteroids) bodies.

#### 3.4.1 Processing of Synthetics

I used a method similar to the one described in Chapter 2 to measure the characteristic decay time ( $\tau_d$ ) and decay factor ( $Q_i$ ) of the synthetic signals. All synthetic data were bandpass filtered to allow the measurement of the decay properties in specific frequency bands. For this study, I investigated decay properties in five 2-Hz wide bands centered on 1, 3, 5, 7 and 9 Hz. I then computed the signals' envelope functions and smoothed them in order to reduce the contribution of noise spikes in the decay fits. Smoothing was done by using a 35 second running window, keeping the 75th percentile. The decaying part of the smoothed curves were fitted in a least-squares sense with an exponential decay curve of the form  $e^{-t/\tau_d}$ , and  $\tau_d$  was retrieved (See Figure 2.3). The coda wave decay factor  $Q_c$  was then calculated using:

$$Q_c = 2\pi f_c \tau_d \quad (3.8)$$

where  $f_c$  is the central frequency of the band of interest.  $Q_c$  is useful to compare decay properties in different frequency bands. Its inverse,  $Q_c^{-1}$ , represents the fraction of energy dissipated after one period of oscillation. In a closed system with uniformly distributed energy, the signal amplitude decay factor  $Q_c$  should be controlled by, and equal to, the intrinsic attenuation factor  $Q_i$ .  $Q_c$  values that are less or more than the local  $Q_i$  suggest leaking or focusing of seismic energy away from or toward the receiver.

The beginning of the fits were determined automatically as the time at which the energy starts to decay exponentially after the theoretical S-wave arrival time. In some models with lower levels of scattering not all the energy from the impulsive wave arrivals is converted into the scattered coda. Fitting only the exponentially

### 3.4. Modeling Approach

---

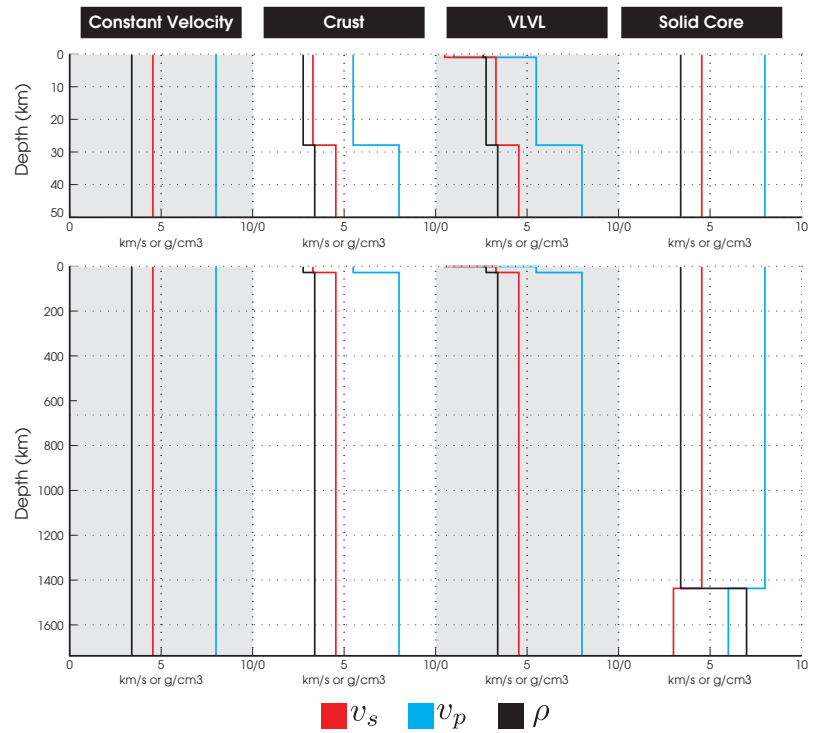


Figure 3.8: Four of the five 1-D velocity and density profiles used in this study, showing the S-wave velocity (red), the P-wave velocity (blue) and the density (black). The modified VPREMOON profile used in C3 is shown in Figure 3.1.

### 3.5. Results and Discussion

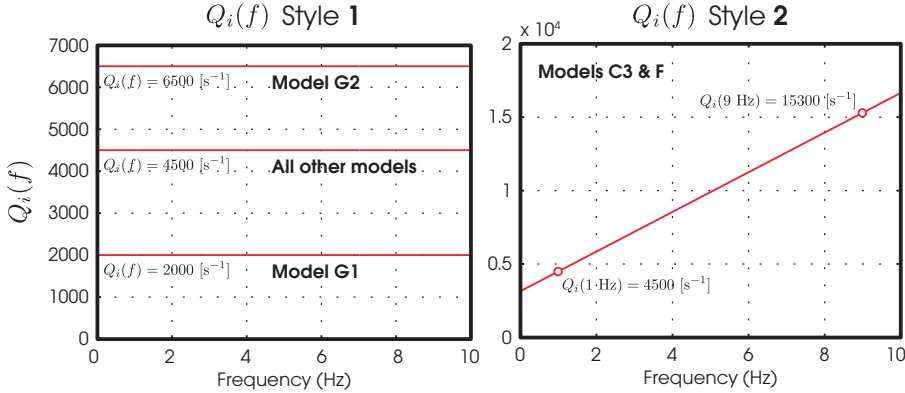


Figure 3.9: The two different  $Q_i(f)$  styles used in the modeling work. Style 1 has a constant  $Q_i$  over the entire frequency range. Most models use  $Q_i(f) = 4500$ , except for models G1 ( $Q_i(f) = 2000$ ) and G2 ( $Q_i(f) = 6500$ ). Style 2 has increasing  $Q_i$  for increasing frequency:  $Q_i(1\text{ Hz}) = 4500$ , up to  $Q_i(9\text{ Hz}) = 15300$ . Style 2 is used in models C3 and F.

decaying part of the coda ensures that I do not fit the larger amplitude impulsive arrivals and retrieve artificially low decay times. It follows that the decay times and decay factors discussed in the following sections are the S-wave coda decay times and factors. All S-wave travel times were computed using the TTBOX package [Knapmeyer, 2004]. The  $\tau_d$  values for individual radial, vertical, and transverse components were similar in all cases and only the average  $\tau_d$  values from all three channels are shown here. Fits were of an arbitrarily determined length of 2500 s, and were only retained if  $\tau_d$  was less than 2500 s. Most fits fell within that constraint and only a small number of fits for models with high scattering levels were dropped.

## 3.5 Results and Discussion

Figure 3.10 presents examples of synthetic traces from all models, for surface impacts and deep events, recorded at an epicentral distance of 50°. All traces have been normalized by their maximum amplitude for better visualization and are aligned on the theoretical P-wave arrival times. The thin red lines indicate the time

### 3.5. Results and Discussion

---

of the first  $\pm 10^{-7}$  DU hit, i.e., the first *observable* P-wave arrival.  $10^{-7}$  DU is the minimum amplitude output by the code. Thus, the red line does not indicate the theoretical P-wave arrival, but the time at which enough energy hits the receiver to become observable. In a non-scattering environment, this would coincide with the theoretical P-wave arrival time (Figure 3.7A). Increased levels of scattering can distribute wave energy over a long time, generating very emergent wave arrivals. This can impede precise wave arrival picks as seen in the traces for models C2, C3, D5 and D6, because the initial direct P-wave energy can be too weak to be observed. The uncertainty in picks would be even greater in the presence of ambient and instrument noise. The effect is greater for impact events than for deep sources because rays from impacts tend to hit the base of the scattering layer at a shallower angle, and this energy thus travels a longer distance in the scattering layer before reaching the receivers.

The substantial visual differences among some of the traces are good initial indicators of the influence that the seismic velocities, scattering and attenuation environment each have on surface recordings. Traces from models with lower scattering such as models D1, D2 and D3, overall have distinct P- and S-wave coda. Traces from models with higher levels of scattering such as C3 and D6 have traces that show a blended P- and S-wave coda. Another important difference among the traces is the apparent signal length. The total signal length of scattered signals is dependent on the initial energy released at the source and on how fast this energy decays near the receivers. For all events I released the same number of phonons (i.e., same total energy at the source), but some recordings, especially those from models with high scattering levels, show a much longer duration signal.

I present an example of detailed results from the coda decay fits in Figure 3.11 for models D4, E and F. I show  $\tau_d$  as a function of epicentral distance, for the five investigated frequency bands, for both impacts (left) and deep events (right). All impact events exhibit a sharp rise in  $\tau_d$  values at short epicentral distances, tend to stabilize at larger distances, and may display another short rise at very large distances. Deep events show similar behavior but without the sharp rise  $\tau_d$  values at short epicentral distances. The effect of  $Q_i(f)$  on the coda decays can be addressed by observing  $\tau_d$  in different frequency bands.  $\tau_d$  clearly decreases with increasing frequency for models with a constant  $Q_i(f)$  (e.g., models D4 and E in

### 3.5. Results and Discussion

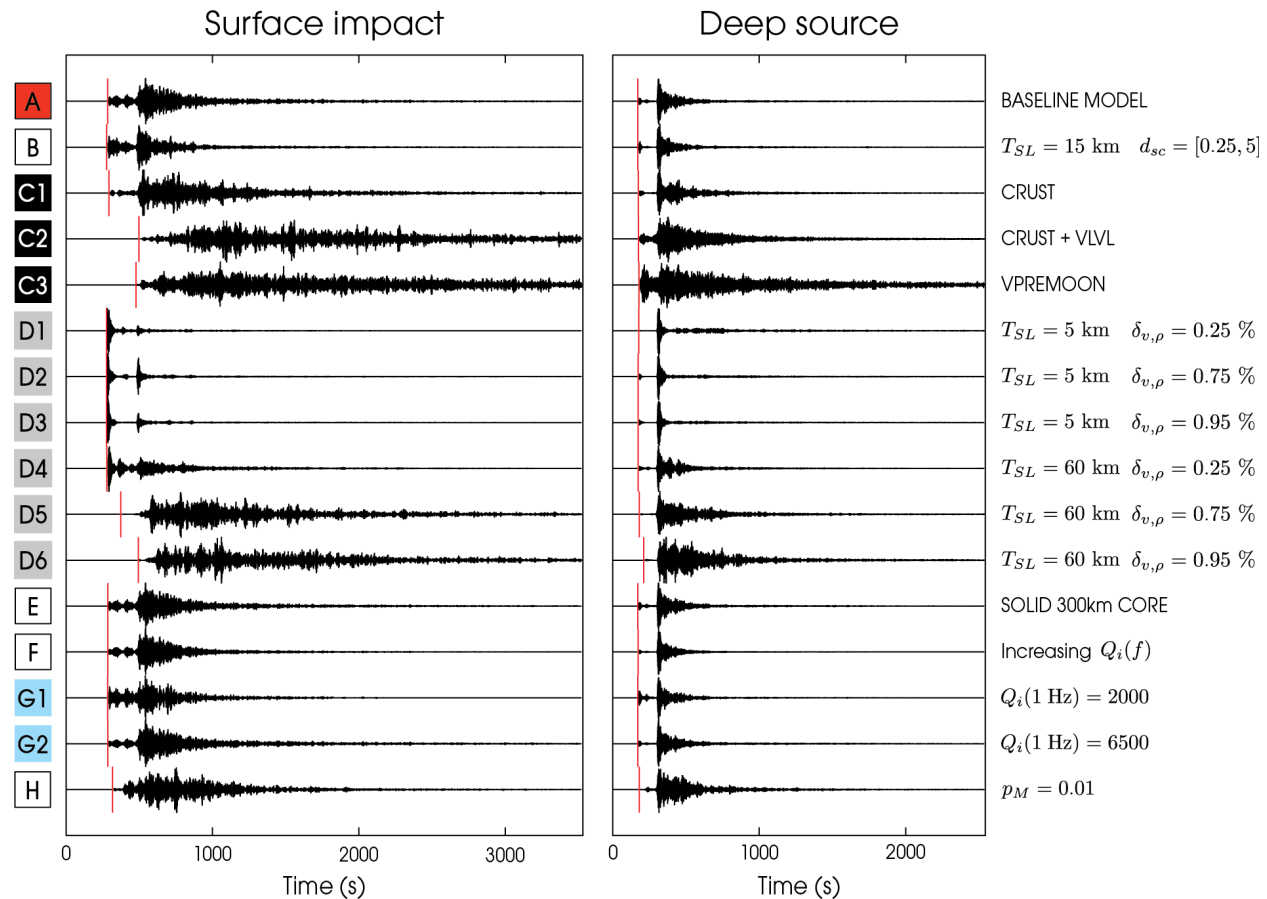


Figure 3.10: See caption on following page.

### 3.5. Results and Discussion

---

Figure 3.10: Examples of synthetic traces for all models presented in this work, for both surface impacts and deep event, at  $\Delta = 50^\circ$ . Note that amplitudes can vary greatly among models, so the traces have been normalized such that their maximum amplitudes are equal. All traces are aligned on the theoretical P-wave arrival times. The top traces are from the baseline model (model A). For each other models (B to H), the annotation on the right indicates the main difference(s) from the baseline model. A detailed description of all the models, including the symbol definitions, can be found in Table 3.1. The red lines indicate the time of the first  $10^{-7}$  DU hit for each traces, which is not the theoretical P-wave arrival time, but the first time at which enough phonons hit the receiver to trigger the minimum  $10^{-7}$  DU amplitude signal. The choice of label colors is arbitrary and designed only to accentuate the different model groupings. Models with white labels are those that can be used individually to show the effect of a particular model parameter.

Figure 3.11). On the other hand, models with an increasing  $Q_i(f)$  (e.g., model F), shows a clustering of  $\tau_d$  values at high frequencies.

Two decay regimes have been identified. Regime 1 (larger outlined circles in Figure 3.11) is characterized by overall shorter decay times, whereas Regime 2 (smaller circles) has much longer decay times. These two regimes were identified in all models and so I first discuss them in more detail below. We shall see that in practice Regime 1 is likely to be the regime that is relevant to seismograms recorded on a planetary surface, and so I then proceed to discuss the results for coda decay times for Regime 1 from the suite of interior structure models studied here. I note that the level of scattering in model D1, with a 5 km scattering layer ( $T_{SL} = 5$  km) and lower maximum velocities and density perturbation levels, was too low to generate codas adequate for fitting and so no further results are shown from that model.

#### 3.5.1 Two Distinct Decay Regimes

Figure 3.11 shows that the transition between Regimes 1 (shorter decay times) and 2 (longer decay times) is gradual and occurs over a fairly large range of epicentral distances. This range varies depending on the internal structure model and on the frequency band. High frequency bands transition to Regime 2 at smaller epicentral distances than lower frequencies. In fact, in most of the models under investigation,

### 3.5. Results and Discussion

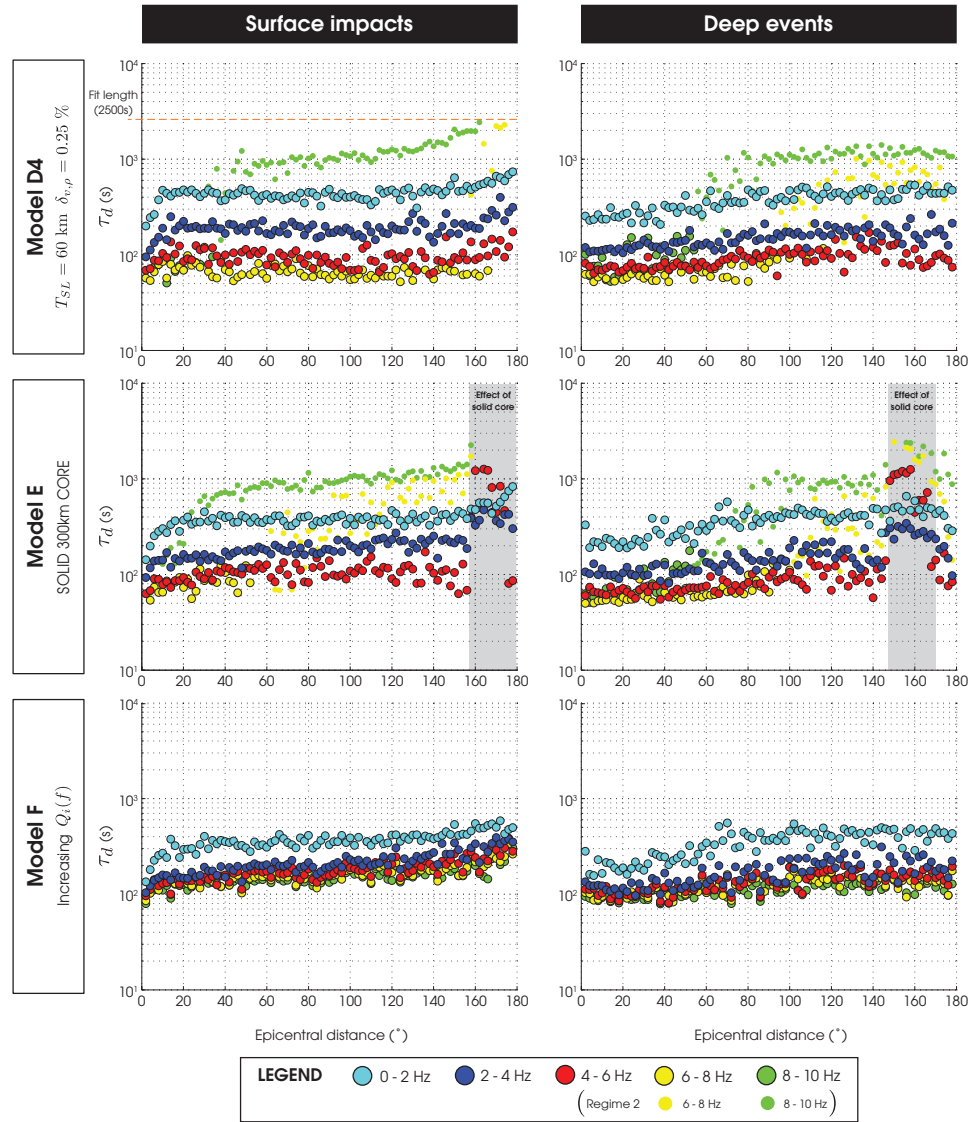


Figure 3.11: See caption on following page.

### 3.5. Results and Discussion

---

Figure 3.11: A) PHONON1D synthetics (blue) vs. TTBox travel times (black), for a PREM model, with a 100 km depth point-source. The logarithmic of the wave amplitudes is plotted in order to show weaker wave arrivals at later times. I only show travel times that TTBOX can compute (i.e. not all multiple reflection phases at later times are identified). B) Comparisons between PHONON1D traces (blue) and CRFL traces (red), showing the transverse component (no P-wave energy) in the 0.10-0.15 Hz frequency band. This is for a simple two-layered Moon, with a 700 km depth point-source. Black lines are TTBOX arrival times. C) Comparisons between PHONON1D traces (blue) and CRFL traces (red), for a PREM model, with a 100 km depth source, showing the vertical component in the 0.10-0.15 Hz frequency band. The PREM model has many interfaces and the discrepancies between the two codes get larger at larger times (e.g. 160°). Note for that both B and C, CRFL plots on top of the phonon code traces, so the absence of blue means a good fit.

scattered cudas in the 8-10 Hz band are in Regime 2, at least at larger epicentral distances. On the other hand, scattered cudas in the 0-2 Hz band always remain in Regime 1. This frequency-dependent transition is demonstrated in the top right plot of Figure 3.11 (model D4, deep events). The transition occurs first in the 8-10 Hz band, starting at around 40° and ending around 80°, and is followed by the 6-8 Hz band with a transition between 90° and 140°.

Figure 3.12 presents synthetic traces and decay fits for traces in Regime 1, in the transition zone, and in Regime 2. I also show the change in  $\tau_d$  and maximum S-coda amplitude values as a function of epicentral distance. The synthetic traces,  $\tau_d$  and amplitude values were measured in the 6-8 Hz band of a model D6 deep event. It is evident that Regime 1 is characterized by much larger amplitudes than Regime 2. The transition between the two regimes occur when the change in maximum S-coda amplitude as a function of epicentral becomes very small, i.e. the maximum S-coda amplitude reaches a near-constant low value for the remaining epicentral distances.

The differences between decays in Regime 1 and 2 are clearly expressed in Figure 3.13 which shows histograms of the averaged  $\tau_d$ , maximum S-coda amplitudes and  $Q_c$  values for impacts and deep events. The average  $\tau_d$  values are calculated over the distance range in which the  $\tau_d$  values are approximately constant for either Regime 1 or Regime 2. Results from all frequency bands are included, from

### 3.5. Results and Discussion

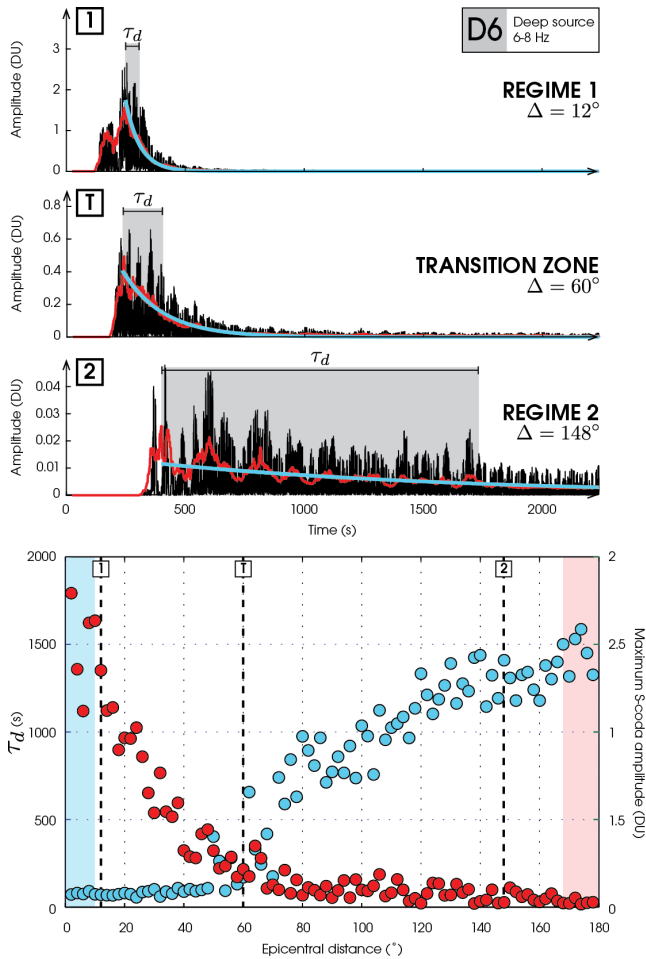


Figure 3.12: Traces and decay times for a deep source event in model D6, showing the transition between regimes 1 and 2. Only traces and results from the 6-8 Hz frequency band are shown. Top 3 panels show the envelope functions (black), the smoothed envelope functions (red) and the least-squares fits (blue) for traces at epicentral distances  $\Delta = 12, 60$  and  $148^\circ$ . The lower panel shows the change in  $\tau_d$  (blue) and maximum S-coda amplitude (red) values as a function of epicentral distance.

### 3.5. Results and Discussion

---

all models with a constant  $Q_i(f) = 4500$ . There is a distinct difference in the mean decay time and mean S-coda amplitude values between the two regimes. Models with lower intrinsic attenuation levels will have less energy transitioning to Regime 2. For example codas from model F, which has an increasing  $Q_i$  (lower attenuation) for increasing frequency, have no decay in Regime 2 (Figure 3.11).

The maximum amplitude coda in Regime 2 is close to the average signal's coda amplitude, and typically there are only two characteristic decay times in the 2500 s long fits, as compared with ten or more in Regime 1. As such, the decay times for Regime 2 decays are less well estimated and in fact, Regime 2 may not be best-estimated by an exponential decay. Further modeling work with longer traces would be necessary to investigate this, which is beyond the scope of the work presented here. However, it is still valid to state that at some distance exponentially decaying scattered signals (Regime 1) become so scattered that the recorded ground deformations are similar to very slowly decaying and very low amplitude seismic noise (Regime 2). This occurs at high frequencies first, because of the larger number of small-scale scatterers than large-scale ones, and because high frequencies go through more cycles over same time period than low frequencies and are thus more attenuated. Regime 2 decays thus occur when most of the P- and S-wave impulsive signals have been reduced to very low amplitudes and very long duration source functions through intrinsic attenuation and scattering.

In Figure 3.13 I also compare the measured  $Q_c$  values with  $Q_i$  ( $= 4500$  for the models shown).  $Q_c$  values for Regime 1 decays are on average slightly less than  $Q_i$ . I propose that in high scattering environments, energy reaching the receiver is partially trapped locally. This is mainly due to the scattering layer reflecting the energy back towards the receiver, effectively mimicking a nearly closed system. In this case, intrinsic attenuation is the main process by which energy levels are reduced. The fact that individual  $Q_c$  values are slightly less or more than  $Q_i$  implies that some leakage or focusing of energy occurs, due to the particular interior structure of each model. Still, I conclude that  $Q_c$  values of Regime 1 decays are good first-order indicators of intrinsic attenuation levels (i.e. good first order approximation of the local  $Q_i$ ).  $Q_c$  values from Regime 2, on the other hand, are all larger than the models  $Q_i(f)$ , suggesting high frequency energy is focused near the surface. However, the low amplitudes and less well-constrained least-squares

### 3.5. Results and Discussion

---

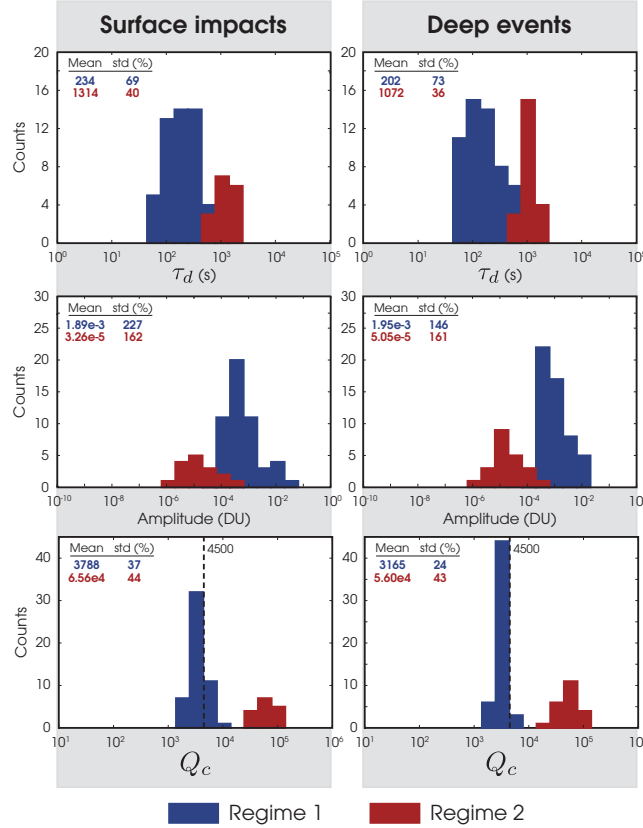


Figure 3.13: Histograms showing the average  $\tau_d$  (top row), maximum S-coda amplitudes (middle row) and  $Q_c$  values (bottom row) for Regimes 1 (blue) and 2 (red), and for both impact events (left) and deep events (right). The mean values for each regime are indicated, along with the standard deviation given as a percentage of the mean. Only models for which  $Q_i(f) = 4500$  are compiled here. Results from all frequency bands are included. The dashed lines in the  $Q_c$  plots show the  $Q_i$  value used.  $Q_c$  results to the left of that line indicate that the codas decay faster than they would if intrinsic attenuation was the only process by which energy was reduced.

### 3.5. Results and Discussion

---

fits prohibits any further interpretations of Regime 2.

In the following sections, all interpretation regarding the effects of the velocity profile, and attenuation and scattering structure on the coda decays uses the Regime 1 decays. This is the regime likely to be measured with surface instruments given the much larger amplitudes.

#### 3.5.2 Effects of Interior Structure on Coda Decay Times

Given the large amount of data, I characterize the  $\tau_d$  as a function of epicentral distance and frequency by an average Regime 1  $\tau_d$  calculated over the distance range in which the  $\tau_d$  values are approximately constant. I summarize these average  $\tau_d$  values for all models and frequency bands in Figure 3.14. Models A, C1, C2 and C3 show the effect of 1-D velocity profiles that increasingly tend to trap seismic energy in lower velocity layers near the surface and in the scattering layer. Models A and D2 to D6 illustrate the changes in coda decay for increasing levels of scattering (implemented using increasingly thicker scattering layers and by varying the maximum velocity and density perturbation levels). Models A, G1 and G3 emphasize the effect of reducing or increasing the reference intrinsic attenuation factor  $Q_i(1 \text{ Hz})$ . Model B halves the scattering layer thickness ( $T_{SL} = 15 \text{ km}$ ) and the minimum and maximum scatterer length scales, such that the seismic energy interacts with the same amount of scatterers, but in a thinner scattering layer. Model E shows the effects of having a small solid core on the averaged  $\tau_d$ . Model F illustrates the effect of a constant versus an increasing  $Q_i$  with frequency (i.e. lower intrinsic attenuation at high frequency). Finally, model H is used to show the effect of low level global scattering on the coda.

##### Sharp rise in impacts $\tau_d$ times at short distances

Figure 3.11 shows an increase in  $\tau_d$  values for impact events between  $0^\circ$  and approximately  $10^\circ$ . This increase is seen in all models, including those not presented in Figure 3.11. Furthermore, a similar trend is observed in the APSE seismic lunar data (see Figure 2.5). The rate of increase, as well as the exact distance at which  $\tau_d$  becomes near constant appear to be model dependent, suggesting that these values could be used to infer first-order near-surface interior structure properties such as

### 3.5. Results and Discussion

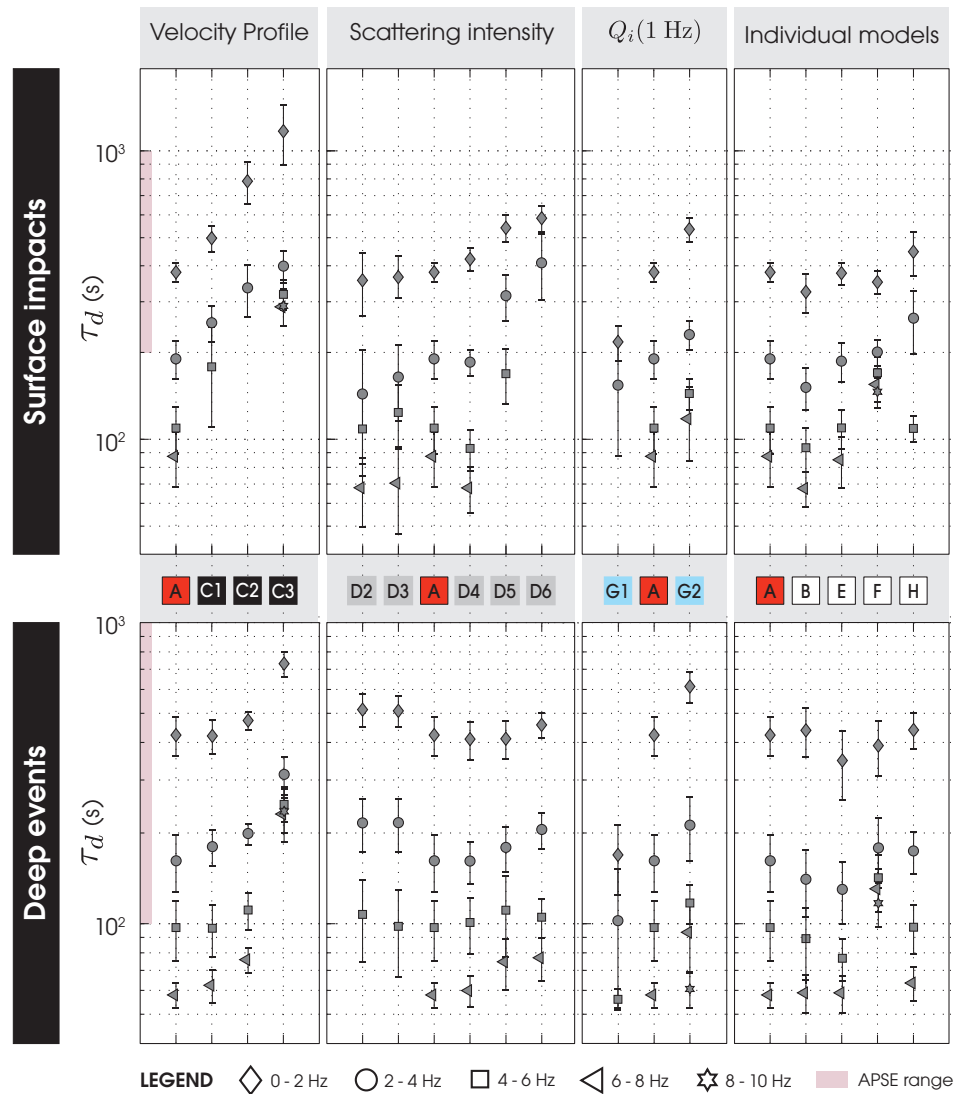


Figure 3.14: See caption on following page.

### 3.5. Results and Discussion

---

Figure 3.14: Plots showing the average  $\tau_d$  values for each models and each frequency bands, for surface impacts (top), and deep events (bottom). Each symbol stand for a different frequency band and the error bars represent one standard deviation about the mean. Only the  $\tau_d$  from Regime 1 are shown. In some model,  $\tau_d$  were in Regime 2 for the entire range of epicentral distances and are thus not included here. The pink bars show the range of  $\tau_d$  present in the Apollo Passive Seismic Experiment (APSE) dataset as comparison (see Chapter 2). Models have been grouped based on which model parameters they help investigate, and each are plotted against the baseline model A. Models C1, C2 and C3 help identify the effect of the velocity profiles that increasingly trap seismic energy near the surface. The scattering intensity (combining both  $T_{SL}$  and  $\delta_{v,\rho}$ ) is investigated with models D2 to D6. The effect of a lower and larger  $Q_i$  (1 Hz) is shown with models G1 and G2. Model B shows the effect of halving the scattering layer thickness and the scatterer length scales (i.e. as many interaction with scatterers as in model A). Model E demonstrates the lack of effect that a small solid core has on the average  $\tau_d$  values. Model F has increasing  $Q_i$  values for increasing frequencies ( $Q_i$  style 2 compared to style 1 in model A). Model H shows the effect of a low scattering level in the interior.

the thickness of the scattering layer and scattering intensity. However, the receiver sampling distance used in this modeling ( $2^\circ$ ) is too large to assess precisely differences between models. Further modeling work could investigate this near-source effect, its potential as a geophysical tool and any specific application to the Apollo seismic data.

I propose that the distance at which the sharp rise in decay times ends relates to the distance at which the seismic energy traveling between the source and the receivers stops interacting only with the scattering layer and starts to have a substantial fraction of the travel path in the underlying non-scattering (or less highly scattering) lower crust or mantle. Our model impact source function is an impulsive delta function ( $\tau_d \rightarrow 0$ ). This initial impulse spreads out as it travels in the scattering layer. Each adjacent receiver is hit by an increasingly diffused source function that travelled primarily within the scattering layer, with closer receivers seeing a more impulsive arrival (shorter  $\tau_d$ ) than the more distant ones (longer  $\tau_d$ ). Distant receivers ( $> 10^\circ$ ) all see a similar source wave function, that has left the scattering layer near the source and travelled in the mantle to reenter the scattering layer at all point near the receivers.

### 3.5. Results and Discussion

---

#### Velocity profile

The velocity profile appears to be one of the parameters that has the biggest impact on the characteristics of the scattered cudas, especially for impact events. Models A, C1, C2 and C3 have velocity profiles that increasingly tend to trap or focus seismic energy near the surface and in the scattering layer. This results in increasingly large decay times, for example from  $\tau_d(1 \text{ Hz}) = 380 \text{ s}$  in model A to  $\tau_d(1 \text{ Hz}) = 1170 \text{ s}$  in Model C3 for impact events. Benchmark model A has only mantle velocities and scattering in the scattering layer is the only process by which the energy remains near the surface. Model C1 introduces a crust/mantle boundary, which will reflect some downgoing rays up into the scattering layer. Model C2 not only has a crust, but also has a near-surface, thin, very-low-velocity layer analogous to a regolith layer. This layer is particularly effective in trapping energy from impact events near the surface and in the scattering layer. Model C3 has a crust, a thin low velocity layer, and a more realistic velocity gradient (velocities increase with depth) which causes the rays to turn at depth, sending them back near the surface sooner than in models without a gradient.

This shows that velocity profiles that are conducive to focusing seismic energy near the surface and / or in the scattering layer can drastically increase the coda decay times. I found that for all other attenuation and scattering parameters remaining equal, the velocity profile has the biggest impact on the decay times.

#### Scattering layer thickness and impedance contrast

Models A and D2 to D6 show the effect of increasing the scattering layer thickness and the impedance contrast on the coda decays. The impedance contrast is incorporated in the model as the maximum variations from the background density and velocities at each scatterers ( $\delta_{v,\rho}$ ). A small  $\delta_{v,\rho}$  means that most phonons will hit scatterers with low velocity and density contrast and that most will be transmitted with only small variations to their original path and so weak forward scattering is preferred. On the other hand, a large  $\delta_{v,\rho}$  will cause more phonons to be widely scattered off path resulting in more isotropic scattering. Low impedance contrasts (e.g.  $\delta_{v,\rho} = 0.25 \%$ ) may be analogous to interaction with annealed fractures or interfaces between two similar lithologies, whereas large impedance contrasts (e.g.

### 3.5. Results and Discussion

---

$\delta_{v,\rho} = 0.95\%$ ) may be analogous to high porosity levels. Models D2 and D3 have a 5 km thick scattering layer, with  $\delta_{v,\rho}$  values of 0.75 and 0.95 % respectively. Models D4, D5 and D6 all have a much thicker scattering layer ( $T_{SL} = 60$  km) and  $\delta_{v,\rho}$  equal to 0.25, 0.75 and 0.95 %. These are compared to the baseline model A that has  $T_{SL} = 30$  km,  $\delta_{v,\rho} = 0.75\%$ . All models used the same scatterer length-scale distribution. None of these models had a velocity profile that was conducive to trapping the energy near the surface and I infer that this is why changing the scattering layer structure has a bigger effect for impact events than for deep events.  $\tau_d(f)$  values for deep events tend to be within one standard deviation of the mean values of all other models and do not seem much affected by variations in  $T_{SL}$  and  $\delta_{v,\rho}$ . In fact, most of the deep event energy will hit the scattering layer at a fairly steep angle and spend less time overall in the layer than energy from impact events.

For impact events both the scattering layer thickness and the average impedance contrast affect the level of scattering and the resulting decay times. Models D3, A and D5 all have  $\delta_{v,\rho}$  set at 0.75 %, but have successively increasing scattering layer thicknesses. It follows that  $\tau_d$  values from model D5 ( $T_{SL} = 60$  km) are larger than those from model A ( $T_{SL} = 30$  km) and from model D3 ( $T_{SL} = 5$  km), with  $\tau_d$  of 541, 380, and 370 s in the 0-2 Hz band, respectively. The same is true of increasing impedance values:  $\tau_d$  values increase from models D4 to D6 which all have a similar scattering layer thickness (421 s, 541 s and 583 s in the 0-2 Hz band). Note that  $\tau_d$  values for the 4 to 10 Hz frequency bands are not shown for model D6, as the high levels of scattering caused these bands to be in Regime 2 at all epicentral distances.

Both increasing impedance contrasts at the scatterers and an increasing scattering layer thickness will result in longer coda decay times. However, a high impedance contrast does not necessarily generate long scattered coda if the scattering layer is insufficiently thick because there will not be enough interactions with scatterers. An example is model D3, which has  $T_{SL} = 5$  km with a maximum impedance contrast of 95 %.

### 3.5. Results and Discussion

---

#### Intrinsic attenuation

Models G1, A, and G2 show the effect of various levels of intrinsic attenuation with  $Q_i(1\text{Hz}) = 2500, 4500$  and  $6000$ , respectively. This corresponds to decreasing levels of intrinsic attenuation. In all models,  $Q_i(f)$  is constant, resulting in high frequencies that attenuate faster than lower frequencies, because they go through more cycles for similar time periods. Results show that decay times increase for increasing  $Q_i(1\text{Hz})$ , at all frequency levels. Decay times in the 0-2 Hz band for impact events increase from 154 s in model G1, to 380 s in model A, and up to 535 s in model G2. In addition the higher attenuation level of model G1 causes more frequency bands to switch to regime 2 scattering and only the 0-2 and 2-4 Hz bands have codas in the Regime 1. The effect is similar for deep events. Overall, results show that an increase in  $Q_i$  by a factor of 2 or 3 can yield similar increase in  $\tau_d$ , depending on the frequency.

The behaviour of  $\tau_d(f)$  and  $Q_c(f)$  can be used to assess the properties of  $Q_i(f)$ , as can be seen with the results from models A, C3 and F. Model A has a constant  $Q_i(f)$ , whereas models C3 and F have an increasing  $Q_i(f)$ , with  $Q_i = 4500$  in the 0-2 Hz band as in model A, 7200 in the 2-4 Hz band, 9900 in the 4-6 Hz band, 12600 Hz in the 6-8 Hz band, and 15300 in the 8-10 Hz band. The attenuation differences are reflected in the decay times and factors. The  $\tau_d$  in model A decreases as a function of frequency (as seen on Figures 3.14 and 3.15), the corresponding  $Q_c$  values, however, tend to cluster, at least for frequencies above 2 Hz. The opposite is true for models C3 and F, where the  $\tau_d$  values cluster in the 2-10 Hz band, and where  $Q_c(f)$  increases with frequency. This observation is particularly important as a similar behaviour is seen in the Apollo lunar seismic data (clustering of  $Q_c$  values at low frequencies and clustering of  $\tau_d$  values at high frequencies, as shown in Chapter 2). This suggests a near constant  $Q_i(f)$  for lower lunar seismic frequencies (0.5-1.5 Hz) and an increasing  $Q_i$  with increasing frequency for the higher frequency range (2-10 Hz).

#### Scatterer density and scattering time

Model B is similar to model A, except that the scattering layer thickness and the minimum and maximum scatterer length-scales are halved. This means that

### 3.5. Results and Discussion

---

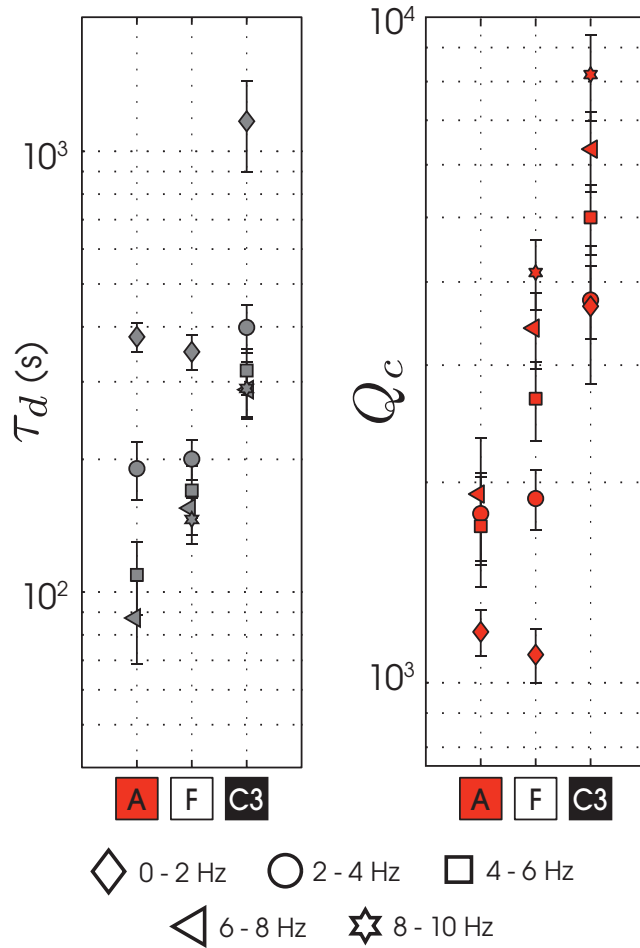


Figure 3.15:  $\tau_d$  (left) and  $Q_c$  (right) for impact events from models A, F and C3. Model A has a constant  $Q_i(f)$  (style 1 of Figure 3.9). Models F and C3 have an increasing  $Q_i(f)$  with increasing frequencies (style 2 of Figure 3.9). Changes in  $\tau_d$  and  $Q_c$  as a function of frequency is dependent on  $Q_i(f)$ . For model A,  $\tau_d$  values decrease as a function of frequency, whereas for models F and C3,  $\tau_d$  values tend to cluster around a constant value (except for the 0-2 Hz band). The opposite is true for  $Q_c(f)$ . Model A values, except for the 0-2 hz band, cluster around 1800, whereas  $Q_c$  values increase with increasing frequency for models F and C3. As such, comparing  $\tau_d(f)$  and  $Q_c(f)$  can be useful to assess the properties of  $Q_i(f)$ .

### 3.5. Results and Discussion

---

phonons in both models interact with the same amount of scatterers. In other words, the *scatterer density* in model B is twice that of model A, but the scattering layer thickness in B is half that of model A. One would expect similar decay times for both models, given that they interact with as many scatterers. However,  $\tau_d$  values from model B are overall less than  $\tau_d$  from model A. This may be due fact that although the seismic energy in model B interacts with as many scatterers as the energy in model A, the path length between those scatterers will be half as long, such that scattered energy will be delayed less relatively to the geometric path than in model A. This leads to overall shorter decay times. One might expect a more drastic drop in decay times in model B (close to half of that of model A), but because the energy in model B spends less time in the scattering layer, it will also be less attenuated, and this effect acts to increase the decay times.

#### Presence of a solid core

The presence of a small solid core (model E) has little effect on the average decay times for either surface impact or deep events (as seen in Figure 3.14). We observe a slight decrease in  $\tau_d$  for the deep events when compared to model A values, but all  $\tau_d$  remain within one standard deviation of each other. This lack of effect on the average  $\tau_d$  is mostly due to the fact that most of the direct P- and S-wave energy leaving the sources does not actually interact with the core. The effect of the core does show up however at larger distances, where no direct P- or S-wave energy hits the surface (the core shadow zone, see middle plots of Figure 3.11 showing increased  $\tau_d$  in shadow zone). Decay times in this region are much larger. Our results also indicate that maximum S-coda amplitudes at stations within the shadow zone are smaller by about 2 orders of magnitude than coda amplitudes at stations just adjacent to the shadow zone. I propose that in high scattering environments, the energy that makes it to surface recorders in the core shadow zone has leaked from the surrounding scattering layers. This scattered leaked energy dominates the signal, in contrast to the other stations where energy from the direct P- and S-wave arrivals dominate.

### 3.6. Conclusions

---

#### Low level mantle scattering

Model H introduces low level scattering in the planetary body's interior. The scatterer length-scale outside of the scattering layer was set to 10 km, with a scattering probability of 0.01. This means that a phonon interacts with a scatterer approximately every 1000 km of travel distance in the interior.  $\delta_{v,\rho}$  was set to 0.75 %, similar to that in the scattering layer. Low level mantle scattering slightly increases the average  $\tau_d$  for both impact and deep events, as observed by comparing models A and H values in Figure 3.14. This increase in average  $\tau_d$  is caused by a slowly increasing  $\tau_d$  with increasing  $\Delta$  (not shown here). This in turn is due to the fact that travelling phonons hitting the base of the scattering layer at large distances will have been scattered more in the interior than those hitting the scattering layer near closer receivers. Another effect of interior scattering can be observed by comparing traces from model A and H in Figure 3.10. For the impact events, low level mantle scattering will effectively blend the P- and S-wave codas, effectively obscuring the S-wave arrival (bottom left trace). Low level mantle scattering as implemented in this model appears to have a negligible effect on deep event traces, except for lengthening the decay time and slightly accentuating the P-wave coda.

## 3.6 Conclusions

I used a phonon method to model the propagation of seismic energy in highly scattering environments. I have generated synthetic traces and measured their characteristic decay times and decay factors to assess the effects of various velocity, attenuation and scattering parameters on the seismic signals. The main observations and conclusions of this study are:

1. High levels of seismic energy scattering will generate ground deformation with amplitudes that decay exponentially (Regime 1), up to a point at which intrinsic attenuation and scattering transform the traveling source function and the resulting ground deformation into very low amplitude, slowly decaying noise-like signals (Regime 2). Our modeling work favored higher scattering levels and faster attenuation for high frequencies and as such, high

### 3.6. Conclusions

---

frequencies transition to Regime 2 at shorter epicentral distances than lower frequencies.

2. I observed a sharp rise in characteristic decay times at short epicentral distances ( $0^\circ$  to  $\sim 10^\circ$ ) for impact events, after which  $\tau_d$  values tend to stabilize. The distance at which  $\tau_d(\Delta)$  stabilizes and the rate of increase appear to be model-dependent, suggesting these values, together with further modeling, could be used to infer first-order near-surface interior structure properties such as the thickness of the scattering layer and the scattering intensity.
3. Velocity structures that tend to trap and focus seismic energy near the surface and in the scattering layer have considerable effect on the characteristic decay times. A crust-mantle boundary, the presence of a thin very low velocity layer near the surface (e.g. the lunar regolith), or a sharp velocity gradient with depth increased the decay times by up to at least a factor of 4 in the models investigated here. This effect is also larger for shallow events – impacts or quakes – than for deep events.
4. Both the impedance contrast at the scattering interfaces and the scattering layer thickness have an effect on the resulting seismic coda. Larger impedance contrasts and a thicker scattering layer will lead to longer decay times. However, a thick scattering layer with lower levels of impedance can scatter energy more than a thin scattering layer with high levels of impedance, at least in the manner in which impedance was modeled in this study.
5. Our modeling showed that higher attenuation levels (lower  $Q_i$ ) will lead to shorter decay times, and conversely that lower attenuation levels result in longer decay times. An increase in  $Q_i$  by a factor of 2 or 3 can yield similar increase in  $\tau_d$ , depending on the frequency band.  $Q_c$  values of Regime 1 signals are good first-order indicators of the near-station intrinsic attenuation level,  $Q_i$ . Similarly, the change of  $Q_c$  as a function of frequency can be used to assess  $Q_i(f)$ : Near constant  $Q_c(f)$  suggests a constant  $Q_i(f)$ , whereas  $Q_c$  values that are increasing with frequency indicate an increasing  $Q_i$  with frequency.

### 3.6. Conclusions

---

6. Deep structures such as a small core have little impact on the decay times. Any effect seems to be spatially limited to the core's direct P- and S-wave shadow zone. Energy is observed in the shadow zone even if no direct wave can propagate into the region, as the energy leaks from the surrounding scattering layer. At these epicentral distances, the maximum S-coda amplitudes are much lower, and the decay times much longer.
7. Increasing  $\tau_d$  as a function of epicentral distance suggests low levels of seismic scattering in the interior. Interior scattering also tends to blend the P- and S-wave codas, making it harder to identify with precision the location of the S-wave arrival.

The velocity profile, intrinsic attenuation and scattering structures of highly scattering planetary bodies have a considerable effect on the duration and form of the resulting ground deformations. Our ability to model and understand these effects will lead to better interpretations of current and future seismic datasets and will provide us with a clearer understanding of the interiors of planetary objects under investigation.

## Chapter 4

# Constraints on Lunar Interior Structure from the Scattered Signals of the Apollo Passive Seismic Experiment

### 4.1 Introduction

Seismic energy propagation in the Moon is dominated by two processes particular to the lunar environment: extreme levels of seismic scattering and very low intrinsic attenuation [Latham et al., 1970a; Nakamura, 1977]. The resulting recorded seismic waveforms are characterized by very long durations, by emergent onsets and by the presence of slowly decaying coda waves that mostly obscure the arrivals of waves other than the P- and S-waves. These long coda typically hinder more traditional analysis techniques that make use of seismic wave arrivals. I showed in Chapter 2 that the decay properties of these coda can be used to assess first-order subsurface scattering and attenuation structures. The results indicated higher levels of scattering for shallow events (impacts and shallow moonquakes) and for increasing frequencies, supporting the idea that scattering mostly occurs in the near-surface megaregolith layer made up of much more small-scale scatterers than large-scale ones.

Nonetheless, further interpretations of the APSE coda observations were hindered by limitations in modeling of seismic energy propagation in a highly scattering, spherical body. I have addressed this issue by developing a method to model seismic energy transmission in lunar-like environments (Chapter 3). My adapted

#### 4.1. Introduction

---

version of the phonon method described in Shearer and Earle [2004] tracks a large number of seismic wavelets (the phonons) as they travel in the planetary body. These phonons are redirected by randomly oriented scatterers in the megaregolith layer, and ground deformation is recorded each time the phonon packets hit the surface near a receiver. The method has been demonstrated to generate synthetic signals that reproduce the general characteristics of the seismograms observed in the APSE dataset. Modeling results from the initial study in Chapter 3 show that several model parameters affect the decay properties of the scattered coda. These include the velocity profile with depth, the megaregolith layer thickness, the impedance contrast at the scatterers, the scatterer length-scales, as well as the intrinsic attenuation levels. Furthermore, I showed that there is a tradeoff between the scattering intensity and the intrinsic attenuation level on the decay rate of the scattered seismic signals.

The main motivation behind this work is to build on the more general results of Chapter 3 and use the APSE data to constrain the interior scattering structure and intrinsic attenuation levels in the Moon. Accordingly, I use the phonon method developed in Chapter 3, along with the coda decay constraints from Chapter 2 to attempt to identify suites of lunar interior models that produce signals with similar decay characteristics to those observed in the APSE data. The APSE receivers recorded with a narrower bandwidth ( $\sim$ 0.5–20 Hz for the long-period and short-period instruments combined) and poorer digitization (10-bit) than typical modern receivers. Thus as part of this study I investigate the limitations of the APSE instrumentation and the resulting data by implementing the APSE instrumentation effects on the synthetic signals.

Early studies with the APSE data provided some constraints on shallow subsurface structure and intrinsic attenuation. Active seismic experiments on the lunar surface (e.g. Kovach et al. [1972]), as well as inversions of seismic signal travel times lead to a series of seismic velocity profiles constraining seismic velocities in the crust and mantle, down to depths of  $\sim$ 1100 km (depth of the deepest located events, see e.g., Toksöz et al. [1971]; Nakamura et al. [1975]; Nakamura [1983]; Khan et al. [2000]; Kuskov et al. [2002]; Lognonné et al. [2003]; Garcia et al. [2011]; Weber et al. [2011]). All of these models included a thin and shallow very low-velocity layer (i.e. the lunar regolith) and a crust-mantle interface. These

#### *4.2. Apollo Passive Seismic Experiment Data*

---

structures will tend to focus seismic energy into the megaregolith layer, increasing the overall scattering observed in the data. Other studies inferred limits on the levels of intrinsic attenuation (as measured by the quality factor,  $Q_i$ , where a low  $Q_i$  corresponds to high attenuation and vice versa) in the crust and upper mantle. Reported  $Q_i$  values vary from 3000 to 6750 in the upper crust, from 4000 to 9000 in the upper mantle, and from  $\sim$ 1000 to 1500 in the upper mantle (see Nakamura and Koyama [1982]; Garcia et al. [2011] and references therein). Nakamura and Koyama [1982] also reported an increase in the shear wave  $Q_i$  from about 4000 at 3 Hz, to at least 7000 near 8 Hz. In addition, modeling and radar studies of the lunar megaregolith indicate a power-law distributions of block sizes for blocks in range of meters to about 1% of the largest basins diameters (or about 10 km, see Schultz and Mendell [1978]), and a scattering layer thickness of a few hundred meters to a few kilometers [McGetchin et al., 1973; Pike, 1974; Housen and Schmidt, 1991; Petro and Pieters, 2004, 2008; Shkuratov and Bondarenko, 2001; Thompson et al., 2009]. I use these results collectively to motivate the general classes of models considered here: models with near-surface low-velocity layers (regolith and crust), with power-law distributions of block sizes, and with intrinsic attenuation levels based on published results.

I first briefly review the APSE dataset in section 4.2 and follow with the modeling approach and data analysis steps in section 4.3. Modeling results are presented in section 4.4.

## **4.2 Apollo Passive Seismic Experiment Data**

The Apollo Passive Seismic Experiment consisted of four seismic recorders, forming a triangular array with stations 12 and 14 at one apex, approximately 1100 km from each of stations 15 and 16. Four main types of seismic events were recorded: artificial impacts (AI, including the Lunar Module impacts and the Saturn-IV Booster impacts), natural impacts (NI), deep moonquakes (DMQ) and shallow moonquakes (SMQ).

The seismic recorders comprised three orthogonal long-period channels (LP) with an instrument frequency response of 0.004 to 2 Hz and one vertical short-period channel (SP) with a frequency response of 0.05 to 20 Hz. In Chapter 2, I

## 4.2. Apollo Passive Seismic Experiment Data

---

Table 4.1: Least-squares fit results from the long- and short-period bands, as measured in Chapter 2. Long-period: Median  $\tau_d$  values (in seconds) and median absolute deviation (MAD) for individual frequency band (L1, L2, and L3) and for all the bands combined. Short-period results: Interpolated  $\tau_d$  values at  $\Delta = 0^\circ$  ( $\tau_d(0^\circ)$ ) and the slope of the best-fit straight line (seconds per degree), with the corresponding standard errors on the coefficient estimates (s.e.). Refer to Figure 2.2 and Table 2.2 to see the frequency range covered by each band.

Long-Period		Short-Period		
Band	Median $\tau_d$ (MAD)	Band	$\tau_d(0)$ (s.e.)	$d\tau_d/d\Delta$ (s.e.)
<b>Artificial impacts</b>				
L1	2732 (239)		-	-
L2	1625 (258)		-	-
L3	932 (126)		-	-
<b>Natural impacts</b>				
L1	2330 (327)	S1	380 (23)	1.4 (0.5)
L2	1362 (131)	S2	234 (26)	1.4 (0.4)
L3	865 (199)		-	-
<b>Shallow moonquakes</b>				
L1	2011 (433)	S1	298 (19)	0.8 (0.3)
L2	1114 (80)	S2	193 (16)	1.2 (0.2)
L3	722 (55)	S3	145 (19)	1.8 (0.3)
<b>Deep moonquakes</b>				
L1	1373 (434)		-	-
L2	978 (143)		-	-
L3	732 (122)		-	-

### 4.3. Methodology

---

selected 72 events, from 55 distinct source locations, and measured their characteristic decay times ( $\tau_d$ ) and decay factor ( $Q_C$ ) in 7 frequency bands: 3 bands for the signals recorded on the LP components, and 4 bands on the SP component. The bands for the LP signals were set to be 0.5 Hz wide and were centered on frequencies of 0.5, 1.0 and 1.5 Hz (L1, L2, and L3 respectively). The bands for the SPZ signals were set to a width of 2 Hz and centered on frequencies of 3, 5, 7 and 9 Hz (S1 to S4, respectively). Results from the LP bands showed no dependence of  $\tau_d$  or  $Q_c$  on epicentral distance, whereas higher frequency signals recorded on the SP component have a clear dependence on epicentral distance. I summarize the  $\tau_d$  results in Table 4.1 for each type of seismic event. I quote results from Chapter 2 for the median  $\tau_d$  values for the LP bands, and the intercepts (value of  $\tau_d$  at  $0^\circ$  epicentral distance) and slopes ( $d\tau_d/d\Delta$ ) of the linear fits with epicentral distance for the SP bands. In this chapter, I investigate how well I can match these properties of the APSE data with synthetic seismograms generated using the method detailed in Chapter 3 and using interior structure models that have a range of scattering and intrinsic attenuation properties.

## 4.3 Methodology

The modified phonon method used here is described in detail in Chapter 3 and summarized in the introduction above. In this chapter I investigate 32 models for which I varied seven different model parameters: the thickness of the near-surface scattering layer ( $T_{SL}$ ), the probability of low-level global scattering ( $p_G$ ), the minimum and maximum scatterer length-scales ( $\delta_{sc}$ ) and their power-law distribution ( $\delta_{sc}^{-n}$ ), the maximum velocity and density perturbation levels at each scatterer ( $\delta_{v,\rho}$ ), the depth-dependent 1-D reference intrinsic attenuation ( $Q_i(1 \text{ Hz})$ ), as well as the intrinsic attenuation frequency dependence ( $Q_i(f)$ ). The choices of parameters for each model are given in Table 4.2.

The different  $Q_i(z)$  and  $Q_i(f)$  profiles are plotted in Figures 4.1 and 4.2, respectively. I investigated four distinct  $Q_i(z)$  profiles: one given by Garcia et al. [2011] (VPREMOON), one with a 50% increase in  $Q_i(z)$  in the VPREMOON model (VPREMOON $\times 1.5$ ), and two with constant  $Q_i(z)$ . The two constant  $Q_i(z)$  models were chosen to have values equal to 6000 and 9000 (Q6000 and Q9000

### 4.3. Methodology

---

Table 4.2: Models investigated in this study.  $T_{SL}$  is the scattering layer thickness,  $p_G$  is the low-level global scattering probability (outside of the scattering layer),  $\delta_{sc}$  sets the minimum and maximum scatterer length-scales and  $n$  defines the power-law probability distribution ( $\delta^{-n}$ ) as outlined in Chapter 3.  $\delta_{v,\rho}$  is the maximum velocity and density perturbation level at each scatterer. The different choices of  $Q_i(z)$  and  $Q_i(f)$  are plotted on Figures 4.1 and 4.2. In the table VP stands for VPREMOON.

Model	$T_{SL}$ [km]	$p_G$ [%]	$\delta_{sc}$ [km] min. max.	$n$ [-]	$\delta_{v,\rho}$ [%]	$Q_i(z)$ model	$Q_i(f)$ style
<b>1</b>	5	0	0.05 10	-0.5	0.75	VP	3
<b>2</b>	30	0	0.05 10	-0.5	0.75	VP	3
<b>3</b>	30	0.01	0.05 10	-0.5	0.75	VP	3
<b>4</b>	15	0	0.05 10	-0.5	0.95	VP	4
<b>5</b>	15	0	0.05 10	-0.5	0.25	VP	4
<b>6</b>	15	0	0.05 10	-0.5	0.6	VP	4
<b>7</b>	30	0	0.05 10	-0.5	0.95	VP	4
<b>8</b>	30	0	0.05 10	-0.5	0.25	VP	4
<b>9</b>	30	0	0.05 10	-0.5	0.6	VP	4
<b>10</b>	30	0.05	0.05 10	-0.5	0.75	VP	4
<b>11</b>	40	0	0.05 10	-0.5	0.95	VP	4
<b>12</b>	40	0	0.05 10	-0.5	0.25	VP	4
<b>13</b>	20	0.0025	0.05 10	-0.5	0.6	Q6000	4
<b>14</b>	20	0.0025	0.05 10	-0.5	0.6	VP	5
<b>15</b>	20	0	0.05 10	-0.5	0.6	Q6000	5
<b>16</b>	20	0.0025	0.05 10	-0.5	0.6	Q6000	5
<b>17</b>	20	0.0025	0.025 5	-0.5	0.6	Q6000	5
<b>18</b>	20	0.0025	0.05 10	-0.5	0.9	Q6000	5
<b>19</b>	20	0.005	0.05 10	-0.5	0.6	Q6000	5
<b>20</b>	20	0.0025	0.05 10	-0.5	0.6	VP	6
<b>21</b>	30	0.0025	0.05 10	-0.5	0.6	VP	6
<b>22</b>	30	0.0025	0.05 10	-0.3	0.6	VP	6
<b>23</b>	30	0.0025	0.05 10	-0.6	0.6	VP	6
<b>24</b>	30	0.0025	0.05 2.5	-0.5	0.6	VP	6
<b>25</b>	40	0.0025	0.05 10	-0.5	0.6	VP	6
<b>26</b>	30	0.0025	0.05 10	-0.5	0.6	VP×1.5	6
<b>27</b>	30	0.005	0.05 10	-0.5	0.6	VP×1.5	6
<b>28</b>	20	0.0025	0.05 10	-0.5	0.6	Q6000	6
<b>29</b>	30	0.0025	0.05 10	-0.5	0.6	Q6000	6
<b>30</b>	30	0.0025	0.05 2.5	-0.5	0.6	Q6000	6
<b>31</b>	40	0.0025	0.05 10	-0.5	0.6	Q6000	6
<b>32</b>	30	0.0025	0.05 10	-0.5	0.6	Q9000	6

### 4.3. Methodology

---

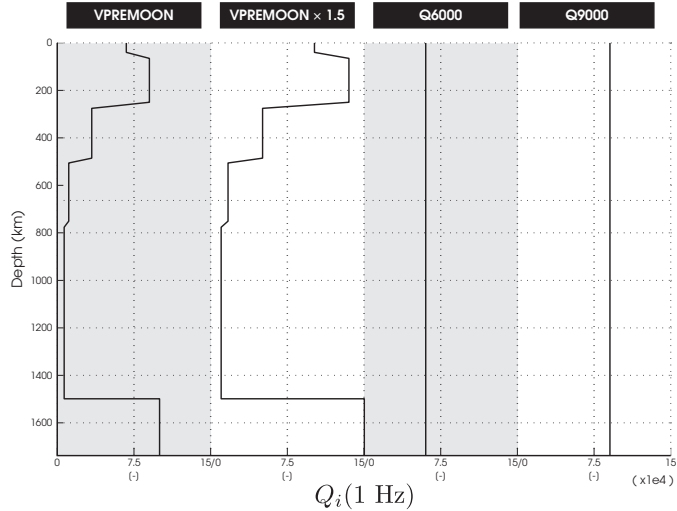


Figure 4.1: The four depth-dependent 1-D  $Q_i(1 \text{ Hz})$  profiles used in this study.

respectively), close to those for the crust and upper mantle in Garcia et al. [2011], and reasonable bounds on averages along the entire source–receiver path for deep, shallow and surface events. Each of the  $Q_i(f)$  styles presented in Figure 4.2 were chosen based on results from Chapter 3 in order to generate synthetics with similar  $\tau_d(f)$  and  $Q_c(f)$  as the ones measured with the APSE data. The  $Q_i(f)$  style 5 was computed so that  $Q_i(f)$  equals the mean  $Q_c(f)$  measured at the APSE stations.  $Q_i(f)$  style 6 is similar to style 5, but with a larger increase in  $Q_i$  at high frequencies. Lower attenuation at high frequencies is consistent with  $Q_i$  values reported in Nakamura and Koyama [1982].

I used a single velocity and density model in which I combined the crustal and mantle velocities from the VPREMOON model in Garcia et al. [2011] with the core velocities from Weber et al. [2011] (see Figure 3.1A). The presence of a thin, low-velocity regolith, a crust, and a velocity gradient with depth is essential to obtaining decay times in the range of those observed in the APSE data (see Chapter 3). I have not tested the effect of a deeper low-velocity zone that is observed in some earlier mantle velocity models (e.g. Nakamura [1983]), as such a layer is not required by the travel time observations; however the effects of a mantle low-velocity zone can

### 4.3. Methodology

---

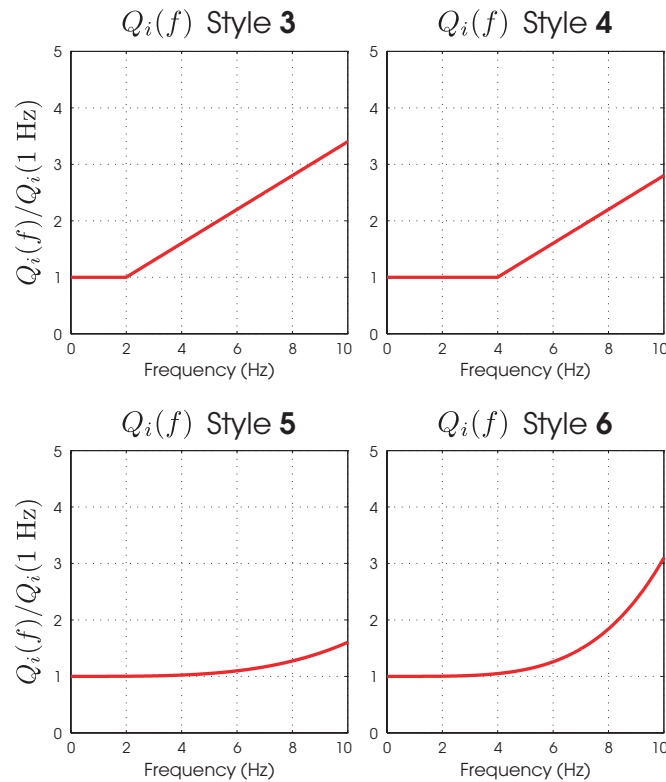


Figure 4.2: The four different  $Q_i(f)$  styles used in this analysis. The plots show the ratios between  $Q_i(f)$  and  $Q_i(1 \text{ Hz})$ , such that a ratio greater than 1 for a given frequency indicates a  $Q_i$  greater than  $Q_i(1 \text{ Hz})$  at that frequency (i.e. lower attenuation). Styles 1 and 2 were used in the analysis presented in Chapter 3.

### 4.3. Methodology

---

easily be tested in future modeling work. The source functions used here are the same as the ones used in Chapter 3 (Figure 3.3). Future work could also investigate the effect of different source functions on the signals, however this was outside the scope of this work.

In section 4.3.1 I describe how I implemented the effects of ambient seismic noise and of the APSE instruments in my modeling. The steps used to measured coda decay times are the same as in Chapter 2 and are reviewed in section 4.3.2.

#### 4.3.1 Modeling Ambient Noise and APSE Instrument Effects

Noise in the APSE dataset originated from several distinct sources. Among these are increased noise levels recorded during passage through the terminator [Dorman et al., 1978] and also resulting from temperature variations on the lunar surface (e.g. [Sens-Schönfelder and Larose, 2010]), the lunar seismic hum (meteoritic [Lognonné et al., 2009] or tectonic), and the long-range transmission of data back to Earth [Nakamura et al., 1980]. Some of these noise sources resulted in high amplitude spikes in the data that could be removed or reduced through various filtering techniques (e.g., Bulow et al. [2005]).

Here I focused on the low amplitude noise that is present throughout most of the recordings. Due to the limited dynamic range of the instruments, this noise is expressed as pervasive 1-bit fluctuations. To investigate the effect of this ambient noise I added white gaussian noise to the synthetic signals, convolved the noisy signals with the APSE instrument responses, and 10-bit-digitized the resulting time series. I explain here how this was implemented.

I measured the maximum signal-to-noise ratio (SNR) for all events analyzed in Chapter 2. I defined the SNR as the ratio between the root-mean-square (RMS) of a 10 s window centered on the time of the maximum S-coda amplitude, and the RMS of 10 s time window of noise measured before the P-wave arrival or after the signal amplitude has decreased to the background noise level. The SNR values range from 1:1 to about 50:1. I then picked the median epicentral distance, and the median SNR for each event type and sampling frequency. These median SNRs and epicentral distances for all types of events, on both the LP and SP components, are listed in Table 4.3.

### 4.3. Methodology

---

Table 4.3: Median epicentral distances and signal-to-noise ratios measured on the APSE signals

Type	Component	Median Epicentral	
		Distance ( $^{\circ}$ )	Median SNR
DMQ	LP	34	4.98
NI	SP	42	8.01
NI	LP	42	10.46
SMQ	SP	68	15.08
SMQ	LP	68	14.28

The magnitude ranges for individual impact or quake events are very poorly constrained. As a result, there is no reliable scaling relationship one can use for characterizing the appropriate quake mechanics to model nor the appropriate resulting measured amplitudes. In fact, such a relationship would depend on an accurate attenuation relationship, which I attempt to calibrate here. For this reason, I scale the synthetic waveforms to the appropriate amplitudes relative to the background 1-bit noise. I make the assumption that the median SNR at the median source-receiver distance is a reasonable proxy for the appropriate SNR with which to scale synthetics of each type.

I defined the amplitude of one bit in the synthetics such that the synthetic signals have a SNR similar to that of the data at an epicentral distance corresponding to the median epicentral distance identified for that type of event in the APSE data. I next added noise to all the synthetic recordings, where the noise was taken from a gaussian distribution with a mean of zero and a standard deviation equal to that of the amplitude for 1-bit for each type of event. I then convolved each signal with the LP or SP instrument responses, and bit-limited the resulting traces. For example, to add noise to a set of deep source synthetics, I measured the RMS of a 10 s window centered on the maximum S-wave coda amplitude ( $R_S$ ) for the synthetic signal recorded at  $34^{\circ}$  epicentral distance.  $R_S/4.98$  is the amplitude of 1-bit for all signals related to this event. I then added noise with root-mean-square amplitude of 1 bit to all signals originating this source. Examples of noise-free versus noisy signals, for an impact and a deep event are shown in Figure 4.3.

### 4.3. Methodology

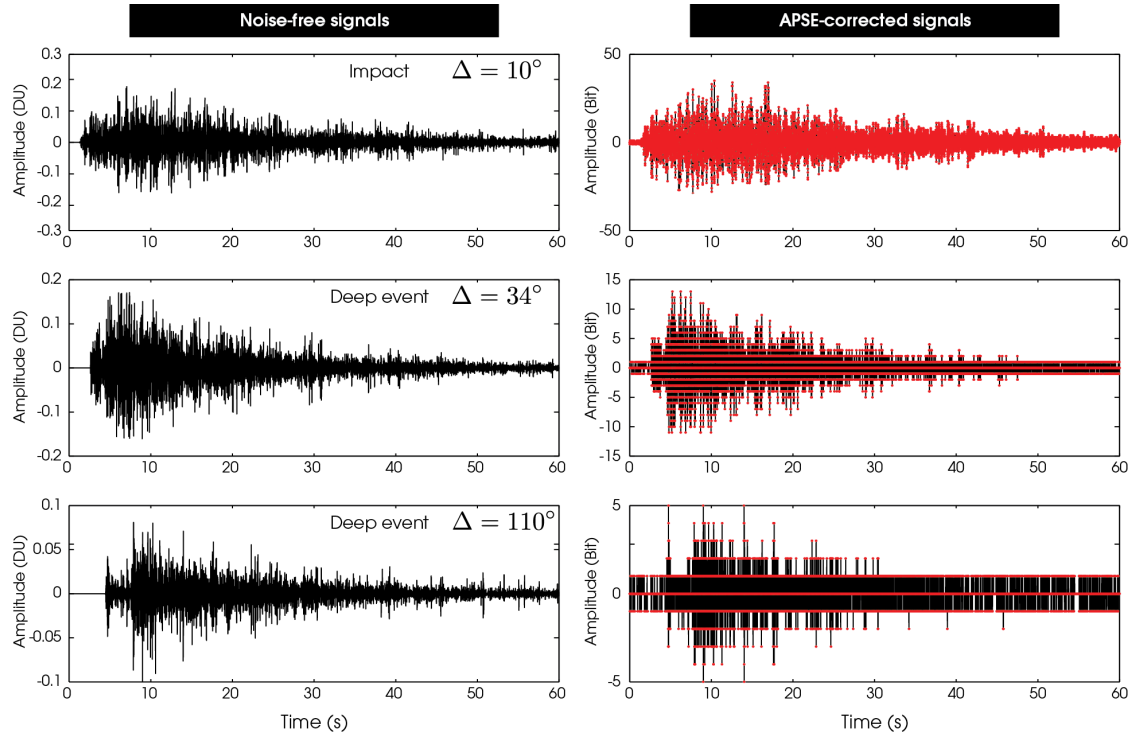


Figure 4.3: Noise-free synthetic signals (left), and resulting signals after addition of 1-bit noise and 10-bit digitization (right). The top signal is from an impact event, recorded at  $10^\circ$  epicentral distance. The middle and bottom signals are both from the same deep event (source at 1000 km depth) and were recorded at epicentral distances of  $34^\circ$  and  $110^\circ$  respectively.

### 4.3. Methodology

---

#### 4.3.2 Analysis of Synthetic Seismograms

Before measuring the coda decay time of each synthetic signal, I followed the analysis steps used in Chapter 2 and for each synthetic seismogram I:

1. Deconvolved the APSE instrument response,
2. Band pass filtered the signal into three LP bands and four SP bands: 0.25-0.75 Hz, 0.75-1.25 Hz, 1.25- 1.75 Hz, 2-4 Hz, 4-6 Hz, 6-8 Hz and 8-10 Hz,
3. Generated the signal envelope,
4. Smoothed the envelope function using a 5 minute (LP) or 35 second (SP) running window, keeping the 75th percentile,
5. Determined when the amplitude started decaying exponentially (the beginning of the fit),
6. Least-squares fit an exponential decay curve of the form  $e^{-t/\tau_d}$  to the decaying section of the smoothed envelope.  $\tau_d$  is the characteristic decay time. All fits were of an arbitrary length of 2500 s for SP signals, and 4000 s for LP signals.

$\tau_d$  can be converted to the frequency-specific decay factor  $Q_c = 2\pi f_c \tau_d$ , where  $f_c$  is the central frequency of the frequency band analyzed.  $Q_c$  is useful to compare decay properties between different frequency bands. However, because  $Q_c$  is directly proportional to  $\tau_d$  I use only the APSE  $\tau_d$  values as model constraints. Accordingly, only summary modeling  $\tau_d$  results are shown below.

To compare the results for synthetic seismograms with the APSE decay values from Chapter 2, I plotted  $\tau_d$  estimated from the synthetics as a function of epicentral distance. I measured the median  $\tau_d$  (LP bands) or the slope and intercept of a best fit of  $\tau_d$  as a function of epicentral distance (SP bands), as shown in Figure 4.4. In all cases, I calculated the medians, or the slopes and intercepts using only data between  $\sim 20 - 130^\circ$  epicentral distance to avoid the near-source effect and the effect of the core on the measured  $\tau_d$  (see Chapter 3).

#### 4.3. Methodology

---

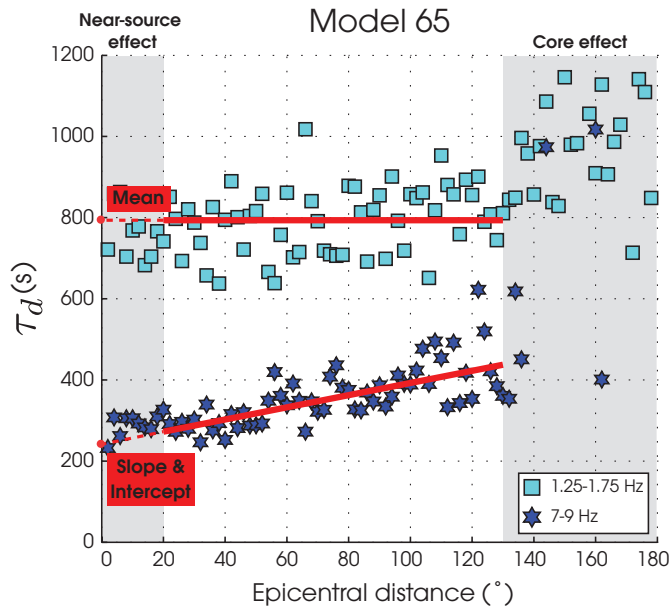


Figure 4.4: Examples of the summary  $\tau_d$  values measured in the 1.25-1.75 Hz band (squares) and in the 7-9 Hz band (stars). The long period bands show no to only a weak increase of  $\tau_d$  with epicentral distance and so only a median  $\tau_d$  value is measured. For short period bands, a least-squares robust fit of the data yields a  $\tau_d$  intercept ( $\tau_d(0^{\circ})$ ) and the slope ( $d\tau_d/d\Delta$ ). The measurements are made over epicentral distances of approximately 20–130° to avoid the effect of the core at large distances and of the sharply increasing  $\tau_d$  at short distances.

## 4.4 Results

### 4.4.1 Results from Modeling of Seismic Noise and APSE-Instrument Effects

I have measured the characteristic decay times from noise-free signals, as well as from the corresponding APSE-corrected signals. Figure 4.5 compares decay times from a 50 km deep event for noise-free signals (Figure 4.5A), APSE-corrected signals (Figure 4.5B), and shows the percentage difference in  $\tau_d$  between the two (Figure 4.5C), for frequency bands corresponding to the APSE short-period component. Results indicate that the exponential decay times measured from the APSE-corrected synthetic signals match the decay times measured from the noise-free synthetic signals, within  $\sim 10\%$ , as long as the SNR is approximately greater than 1. Below this threshold, the added noise and limited bit-digitization either totally obscures the original signal, or affects the signals' decay such that they lose their exponential behavior. In this case, the automatic fitting method fails and tend to generate artificially large  $\tau_d$  values (for  $\text{SNR} < 1$ ). The distance at which the measured  $\tau_d$  on the APSE-corrected synthetic signals diverge from the noise-free synthetic signals depends on the epicentral distance at which I implemented the average SNR ( $68^\circ$  in Figure 4.5B). Higher frequencies decay times start diverging earlier due to their lower overall amplitudes (i.e., they reach  $\text{SNR} < 1$  at shorter distances).

All signals used in the analysis presented in Chapter 2 were selected based on the quality of the seismic trace, and all selected signals had a  $\text{SNR} > 1$ . Importantly, the results presented here indicate the  $\tau_d$  and  $Q_c$  values obtained in Chapter 2 were not affected by the APSE instruments bit-limitation or by the presence of seismic noise, and that they are representative of the lunar interior structure. Based on this conclusion, I now show only  $\tau_d$  values measured from noise-free synthetics in order to examine any variations in  $\tau_d$  over the entire epicentral distance range ( $0\text{-}180^\circ$ ).

#### 4.4. Results

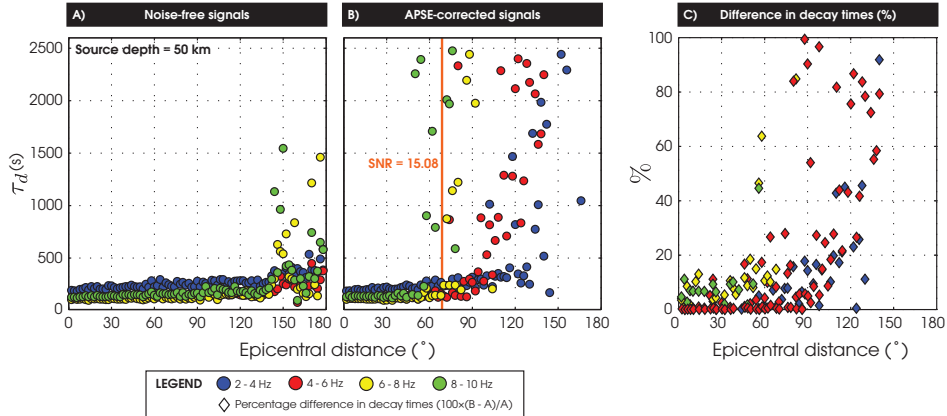


Figure 4.5: Characteristic decay times ( $\tau_d$ ) measured from noise-free signals (A), and from the same signals after being corrected for the 1-bit seismic noise and the APSE-SPZ instrument effects (B). The percentage difference in decay times,  $(100 \times (B - A)/A)\%$ , is shown in C. The orange line in B shows the distance at which the amplitude corresponding to 1 bit was measured ( $\Delta = 68^\circ$ ). The increase  $\tau_d$  at large distances in A is due to the small core included in the model.

#### 4.4.2 Modeling Results

Figures 4.6 shows the median  $\tau_d$  measured in the long-period frequency bands (0.5–1.75 Hz) for both shallow and deep events, for all 32 investigated models. As a comparison, the median  $\tau_d$  values from the APSE data are shown. Results show that variations in the scattering structure (i.e. the scattering layer thickness, the impedance contrast at the scatterers, the scatterer length-scales) have little effect on the median  $\tau_d$  (e.g. models 1–20, except for model 10, have near constant median  $\tau_d$ ). Only model 10, which has a high global scattering probability ( $p_g = 5\%$ ), shows larger median  $\tau_d$  values.

The main control on the median  $\tau_d$  appears to be the intrinsic attenuation level  $Q_i(f)$ . Results indicate that only the models using somewhat lower attenuation levels (i.e. higher  $Q_i$ ) than that proposed in the VPREMOON model produce median  $\tau_d$  values that match the APSE data, for both the shallow and deep event cases. For example, models 26 and 27 with a  $Q_i(z)$  profile like that of VPREMOON, but 1.5× larger in magnitude), or model 32 that has a constant  $Q_i(z)$  of 9000 produce

#### 4.4. Results

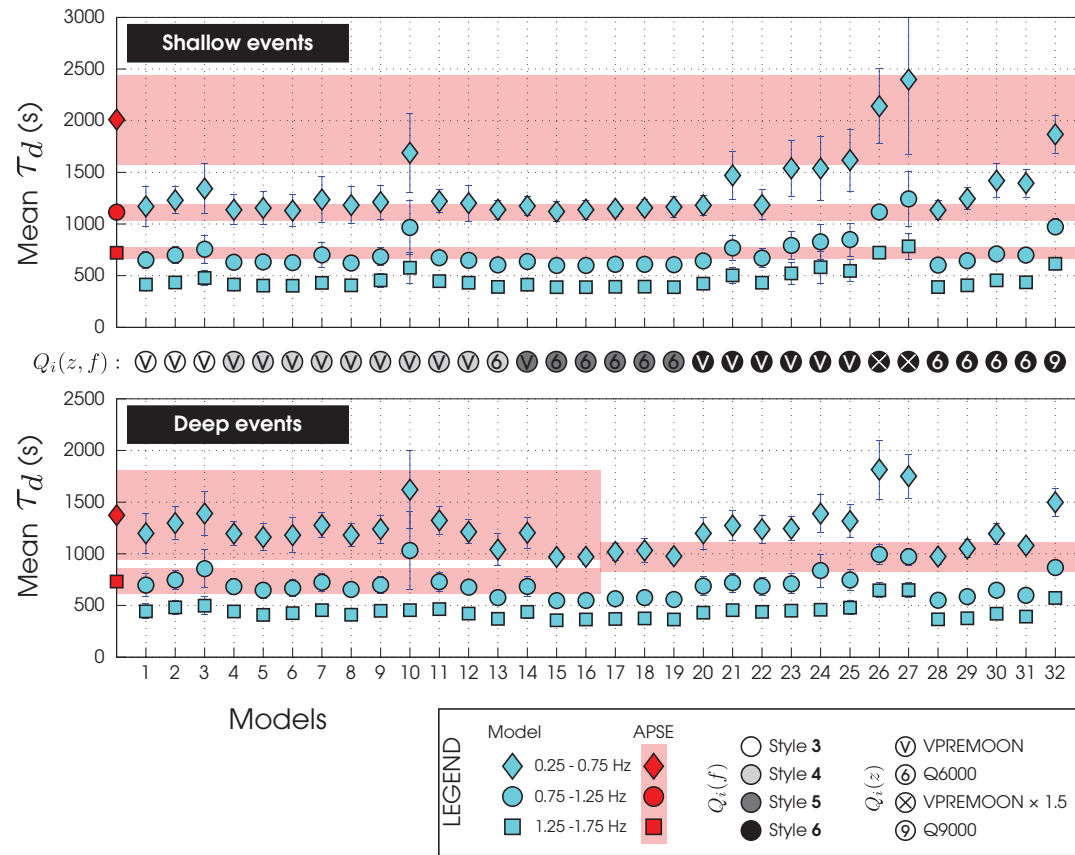


Figure 4.6: Median  $\tau_d$  values measured in the low frequency bands (0.5-1.5 Hz) for shallow events (top) and deep events (bottom) for the 32 models investigated in this analysis. The red bars indicate the median  $\tau_d$  measured with the APSE data in Chapter 2 within one median absolute deviation. Note that for overlapping APSE value ranges, the ranges are plotted on only either half of the plot, as in the deep event case. However, these values apply to all models. Also, in some cases the uncertainty in  $\tau_d$  derived from the synthetics is less than the height of the symbol and is not shown.

#### 4.5. Discussion

---

synthetic seismograms that yield median  $\tau_d$  that match the APSE data.

In Figure 4.7 I present the measured slopes and intercepts for a selection of models that best represent the effects of the scattering and intrinsic attenuation parameters on the data, as well as the models that best match the data. Results for surface impacts and shallow events are presented, and measurements from the APSE data are plotted for comparison (only the 2-4 and 4-6 Hz bands are available for the impact events for the APSE data). In the case of the  $\tau_d(0^\circ)$  intercepts (Figure 4.7A and B), the models with lower intrinsic attenuation values (models 26, 27 and 32) perform best in matching the APSE data in the lower frequency bands (2-6 Hz). None of the models investigated properly reproduce the  $d\tau_d/d\Delta$  slopes observed in the APSE data (Figure 4.7C and D). However, in contrast to the median  $\tau_d$  values and the intercepts, the slopes for impact events are more strongly affected by the scattering structure (Figure 4.7C) and not only controlled by the intrinsic attenuation.

## 4.5 Discussion

The crust and thin surficial low-velocity layer (analogous to the lunar regolith) included in the velocity profile used in the analysis focus seismic energy near the surface and into the scattering layer. As seen in Chapter 3, such velocity profiles generate coda that are much more scattered (i.e., longer  $\tau_d$ ) than models without a crust or low-velocity regolith. In such very highly scattering environments, further variations in scattering properties do not appear to be the main control on the decay characteristics of the scattered codas. For example, both a thin and a thick scattering layer will generate similar decay times (e.g. model 1 with  $T_{SL} = 5$  km and model 11 with  $T_{SL} = 40$  km). For models using the VPREMOON or the Q6000  $Q_i(z)$  profiles, no combination of scattering property values produced decay times that match those observed in the APSE data, at least not in the lower frequency bands. The one exception is model 10 that has a high probability of global scattering ( $p_g = 5\%$ ) and produced median decay times in the lower frequency bands that compare with the APSE values, but resulted in slopes  $d\tau_d/d\Delta$  at higher frequencies that are too steep. I found that the best way to affect the decay times is to change the intrinsic attenuation levels in the models ( $Q_i(f, z)$ ). Models using

#### 4.5. Discussion

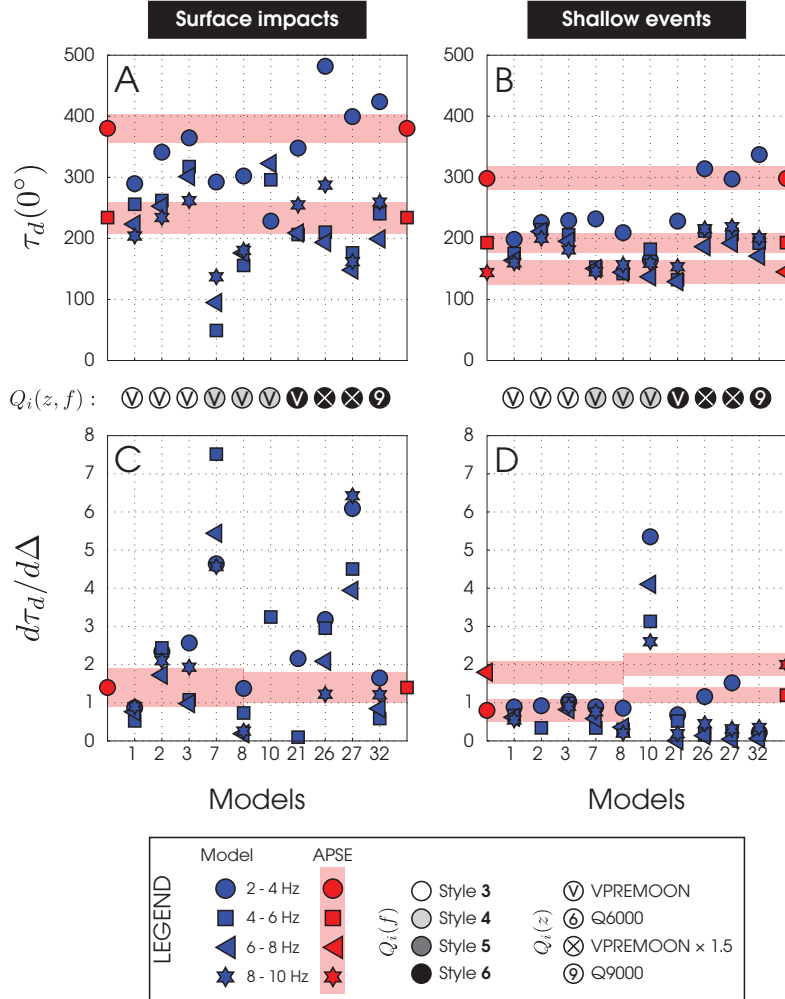


Figure 4.7: Intercepts (A and B) and slopes (C and D) of least-squares fits on the short-period bands (2-10 Hz), for surface impacts and shallow events. Similar measurements from the APSE data are given (red), within one standard error. Same format as Figure 4.6.

#### 4.5. Discussion

---

$Q_i(z)$  values that are 50% larger than the ones in the VPREMOON model (models 26 and 27), or models using a constant  $Q_i(z) = 9000$  (Q9000), produce decay times that compare well with the APSE data at low (median) and high (intercept) frequencies, at least up to 6 Hz. I propose that there are conditions under which scattering is so extreme (e.g. when a crust and a regolith focus scattered energy back into the scattering layer) that variations in the scattering properties do not significantly affect the decay times of scattered coda. In such situations, anelastic processes exert the greatest control on the decay of seismic energy (intrinsic attenuation). As such, measuring median decay times and intercept values may not be the best tool to assess the length scales of scattering of very highly scattering bodies like the Moon, but they can give us some first order information regarding the levels of intrinsic attenuation.

Based on the modeling observations from Chapter 3, I found that a near constant  $Q_i(f)$  at lower frequencies (0.5–1.5 Hz) and an increasing  $Q_i(f)$  at higher frequencies (2–10 Hz) is necessary to reproduce the corresponding APSE decay times dependence on frequency ( $\tau_d(f)$ ). Based on the models investigated,  $Q_i(f)$  style 6 provides the best match when combined with the VPREMOON $\times 1.5$  or the Q9000 models. However, more investigations of the parameter space are needed to test which  $Q_i(f)$  works with the depth-dependent  $Q_i(z)$ , either the styles already modeled, or a different style for a better overall fit with the APSE data.

One potential way to investigate scattering structures would be to make use of the slope of  $\tau_d$  as a function of epicentral distance in the high frequency bands. None of the models investigated in this study produced slopes that compare well with the ones from the APSE data (see Figures 4.7C and 4.7D). However, the slopes seem to be particularly affected by the model scattering parameters, especially for surface impact events (Figures 4.7C). We see an increase in slope for models with high maximum velocity and density perturbation level (e.g., model 31), as well as for models with a higher probability of global scattering (models 10 and 27). Slopes also seem to increase with increasing scattering layer thicknesses (e.g., model 1 with a 5 km thick scattering layer, versus model 2 with a 30 km thick scattering layer). On the other hand, change in intrinsic attenuation levels have little impact on the slopes, especially for shallow events (Figure 4.7D). Future work will need to further explore parameter space in order to find models with

#### 4.6. Conclusions

---

slopes that better match the APSE data and achieve improved constraints on the scattering structure of the lunar interior.

The main goal of this analysis was to investigate a suite of scattering structures in order to constrain the length scales of scattering in the lunar interior (e.g.,  $T_{SL}$ ,  $\delta_{sc}$ ,  $\delta_{v,\rho}$ ,  $p_g$ ). However, as discussed above, the median  $\tau_d$  values for models 1–25 (except model 10) show that changes in the scattering properties at the levels implemented in this work (e.g., changes in  $T_{SL}$ ,  $\delta_{sc}$  of a factor of a few) do not have a significant effect on the coda. Further modeling (models 26–32) suggests that most changes in coda decay times are captured by the intrinsic attenuation ( $Q_i(f, z)$ ). As each model run takes approximately 3 weeks to complete on a multi-core system (computation of the synthetics and data analysis, including the smoothing of the signals), I saved computational time for models 26 and above by not basing my choice of model parameters on a systematic search of the parameter space, but rather attempting to explore changes to the models that experience suggested could be important. More modeling work is thus needed to put limits on the length scales of scattering using  $Q_i(f)$  styles 5 and 6, and the VPREMOON×1.5 and Q9000  $Q_i(z)$  profiles.

## 4.6 Conclusions

The main objective of this analysis was to identify a suite of lunar interior models that produce synthetic seismograms that share the decay properties of the scattered seismic signals in the APSE dataset. I have first demonstrated that the ubiquitous seismic noise in the lunar data, along with the bit-limited nature of the APSE instruments, did not significantly affect the decay times for lunar seismic signals with a SNR greater than 1. As such, I conclude that the decay measurements presented in Chapter 2 are representative of the lunar interior structures and can be used as constraints for the modeling work.

The combination of a thin shallow regolith, a crust, and a scattering layer generates a very highly scattering environment on the Moon. In such a context, the scattered coda decay times are mostly controlled by the intrinsic attenuation levels  $Q_i(f, z)$ , and not by the length scales of scattering. Consequently, the median  $\tau_d$  values are not sufficient to identify the lunar scattering structure. This could

#### 4.6. Conclusions

---

be achieved by investigating the variations in the  $d\tau_d/d\Delta$  slopes. However, the median decay times can provide some constraints on intrinsic attenuation levels. I have observed in the modeling a need for higher  $Q_i$  than proposed in Garcia et al. [2011], as well other published  $Q_i$  values based on amplitude decay with travel time and distance (e.g. Nakamura and Koyama [1982] and references therein). Models with a 50% increase in  $Q_i$  values from the VPREMOMON models, or with a constant  $Q_i(z) = 9000$  at 1 Hz, combined with an increasing  $Q_i(f)$  with increasing frequencies, produce scattered synthetics with similar decay times to those observed in the APSE data.

More modeling work is needed to systematically investigate the parameter space of plausible intrinsic attenuation and scattering structures compatible with the APSE coda decay times. I need to test the effect of varying the scattering properties in higher  $Q_i$  scenarios, and to test different velocity profiles to see if the decay times then vary or if they remain within the range of values measured with the APSE data. Further work will also investigate whether the slopes of the  $\tau_d$  as a function of epicentral distance are a better tool to assess the length scales of scattering.

# **Chapter 5**

## **Effects of Lateral Variations in Megaregolith Thickness on Recorded Seismic Signals**

### **5.1 Introduction**

Seismic signals recorded during the Apollo Passive Seismic Experiment (APSE) were strongly affected by the scattering of seismic energy in the Moon’s interior, mainly within the near-surface megaregolith layer (e.g., Latham et al. [1970a]; Blanchette-Guertin et al. [2012]). A consequence of the scattering is that secondary seismic phases, which could be used to detect major compositional and phase boundaries within the Moon, are almost entirely obscured in the APSE data set. In this work, I use a synthetic seismogram phonon method (Shearer and Earle [2004] and Chapter 3) to investigate the effects of laterally varying megaregolith thickness on the propagation of seismic energy, and on the resulting seismic signals recorded at various epicentral distances from the moonquake or impact source. A major objective of this study is to identify conditions under which seismograms recorded at the surface are less likely to be affected by high levels of scattering, and for which secondary arrivals containing important information about interior structure can be more readily identified. Such studies will help optimize the design of future non-terrestrial seismic surveys to maximize scientific return.

Several past studies investigated the distribution of large basin ejecta on the lunar surface (e.g., Short and Forman [1970]; McGetchin et al. [1973]; Pike [1974]; Petro and Pieters [2008]). Ejecta from major impact events is one of the major components of the megaregolith layer, along with the underlying fractured crust

### 5.1. Introduction

---

[Hörz, 1991]. Estimates of megaregolith thicknesses resulting from the different ejecta models presented in these studies vary from hundreds of meters to several kilometers. However, all studies agree that the thickness of the megaregolith will vary geographically, from thicker near the edges of the basins, to thinner at locations far from the impact structures. Other studies using Earth-based radar imagery showed variations in megaregolith thickness between regions in the northern and southern hemisphere on the near side [Thompson et al., 2009], and a systematic difference in the depth to the base of the megaregolith between the highlands and the large mare basins [Thompson et al., 1979], the latter having substantially thinner megaregolith. It is assumed that the megaregolith will be thinner beneath the basins themselves, due to ejection of material radially outward from the impact site. In addition, the megaregolith beneath younger basins is expected to be thinner because of less cumulative ejecta from subsequent large impacts in the surrounding regions. The APSE stations were located on highlands near the edges of large basins (station 16), or within old basin structures, very close to the basin edge (station 15), or near surface topography with high scattering potential (stations 12 and 14). All seismic signals recorded at these locations were affected by similarly high levels of scattering [Blanchette-Guertin et al., 2012].

Using the phonon method developed in Chapter 3 I assess the effects of laterally varying megaregolith thicknesses, occurring in association with impact basins, on the seismic signals recorded at various locations along the surface. I investigate here two simple basin models: A)  $4^\circ$ -diameter ( $\sim 120$  km) basins, centered at epicentral distances,  $\Delta$ , of  $20^\circ$  and  $40^\circ$ ; and B) a  $40^\circ$ -diameter ( $\sim 1200$  km) basin centered at  $\Delta$  equal to  $60^\circ$ . I have tested several megaregolith thickness models, where the impact structures are surrounded by a 30 or 60 km thick megaregolith, and underlain by either no megaregolith or by a 5 km thick megaregolith. These scenarios are intended as proxies for younger impact basins with less subsequent impact resurfacing and megaregolith production than in the older surrounding terrain. I have computed synthetics for surface events (impacting on top of the megaregolith) as well as for 1000 km deep events (analogous to lunar deep quakes). In all cases, I used a modified VPREMOON velocity model [Garcia et al., 2011] to which I have added the velocities for the lunar core from Weber et al. [2011]. In this chapter, I use the term *basin* to refer to both the smaller and the larger structures. Typically,

## 5.2. Methodology

---

*basin* refers to impact structures on the Moon that are 300 km or larger in diameter [Wilhelms, 1987].

## 5.2 Methodology

The phonon method used here is detailed in Chapter 3. The approach tracks a large number of seismic wavelets as they travel through a planetary interior from a source located at  $\Delta = 0^\circ$ , and it records the associated ground deformation each time a phonon packet hits the surface near a given receiver. In the megaregolith layer the phonons encounter randomly oriented scatterers every  $\delta_{sc}$  m, where  $\delta_{sc}$  is randomly sampled from a power-law distribution that has many more small-scale scatterers than large ones. The phonons are stochastically scattered, or not, based on the scattering probability and on the velocity and density perturbations associated with the scatterer. These perturbations are picked randomly and were on average  $\pm 35\%$  of the background values for the models presented here. This favors forward scattering of the phonons vs. backscattering. The energy partitioning ratio at the source is 1:10:10 (P:SV:SH) in the case of deep event, and 1:0:0 for the surface impacts.

## 5.3 Results

Figures 5.1 and 5.2 present synthetic seismograms for 5 models comprising three distinct megaregolith structures and two different basin diameters. The basin diameters and megaregolith structures are shown in the schematics at the top of each set of seismograms. The thickness of the megaregolith surrounding the impact basin ( $T_{SL}$ ) and the thickness of the megaregolith beneath the basin itself ( $T_B$ ) are indicated for each model. Figure 5.1A shows signals derived from a surface impact event (source depth of 0 km). All other models shown (Figure 5.1B and Figure 5.2) are for signals from deep sources (source depth of 1000 km). For all models the epicentral distance between each receivers is  $0.5^\circ$ , or about 15 km, on the lunar surface. The seismic traces shown beneath the receivers correspond to the ground deformations recorded on the vertical channel at the receiver locations. The amplitudes in each trace have been normalized such that the root mean square

### 5.3. Results

---

amplitudes of all traces are equal. In Figure 1 I compare synthetic signals recorded for an impact and a deep event across a 120 km diameter basin, with  $T_{SL} = 30$  km and  $T_{SL} = 0$  km. In Figure 2 I show synthetic signals for a deep event and different megaregolith structures and basin diameters.

All impact-derived signals shown in Figure 5.1A exhibit strongly scattered codas, including those recorded at stations in the basin even with no megaregolith ( $T_B = 0$  km). This makes it difficult to identify wave arrivals, even for the initial P-wave which is very emergent. This is mainly because all the energy is first scattered near the source. Other results, not shown here, indicate that signals recorded in basins with a thin to no megaregolith are much cleaner for all types of events for which there was no source-side scattering. These could be events near the surface but beneath the megaregolith (perhaps analogous to lunar shallow quakes) or impacts into a region with a very thin megaregolith. Synthetics are thus much cleaner in the case of deep events (Figure 5.1B and Figure 5.2), where most of the energy is allowed to first travel with minimal scattering in the mantle before reaching the receivers. As a consequence, I now focus the investigations on deep events.

In Figure 5.1B, I show signals derived from a deep source for the same megaregolith structure as in Figure 5.1A. In this case, both the P and S-wave arrivals are identifiable, although the S-wave is more impulsive for signals recorded in the basin than for those recorded at stations in the surrounding region where  $T_{SL} = 30$  km. Importantly, the ScS core reflected phase is visible in the basin signals. Other core phases, which would have lower amplitudes, are lost in the coda generated by the near-surface very low-velocity layer and in the seismic noise caused by the energy leaked from the surrounding megaregolith.

The deep event signals shown in Figure 5.2A demonstrate the effect of adding a megaregolith layer in the impact basin that is thin ( $T_B = 5$  km) compared with beneath the surrounding terrain ( $T_{SL} = 30$  km). In this case, all signals exhibit strong scattering. It is still possible to pick the P- and S-wave arrivals, however all secondary phases are obscured by the coda.

In Figure 5.2B, I investigate the effect of a thicker surrounding megaregolith ( $T_{SL} = 60$  km) on the seismic signals recorded near the basin edges. In Figure 5.1B seismograms recorded at stations in the basin, but only 15 km from the basin edge, show much less scattering than the signals recorded on top of the megare-

### 5.3. Results

---

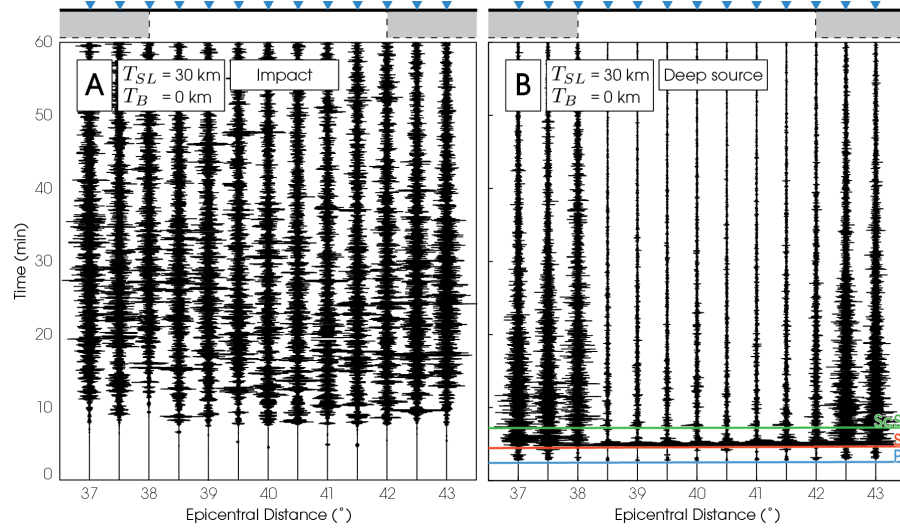


Figure 5.1: (A) Vertical component of synthetic seismograms for a surface impact event, and (B) a 1000 km depth event, recorded across the simplified structure representing a 120 km diameter basin. Note that I refer to both the large and small impact structures as basins for brevity in this chapter – see main text. The blue triangles in the top schematic represent the seismic receivers at which the synthetic signals shown below were recorded. Shaded regions under the stations represent the megaregolith layer. For these two events, the megaregolith thickness surrounding the basin is 30 km ( $T_{SL} = 30 \text{ km}$ ), and the megaregolith thickness beneath the basin is 0 km ( $T_B = 0 \text{ km}$ ). The distance between each station is  $0.5^\circ$  (15 km). The time is relative to the source origin time. Theoretical P (blue), S (red), and ScS (green) arrivals are plotted on B. The lines are slightly offset for better viewing of the arrivals.

### 5.3. Results

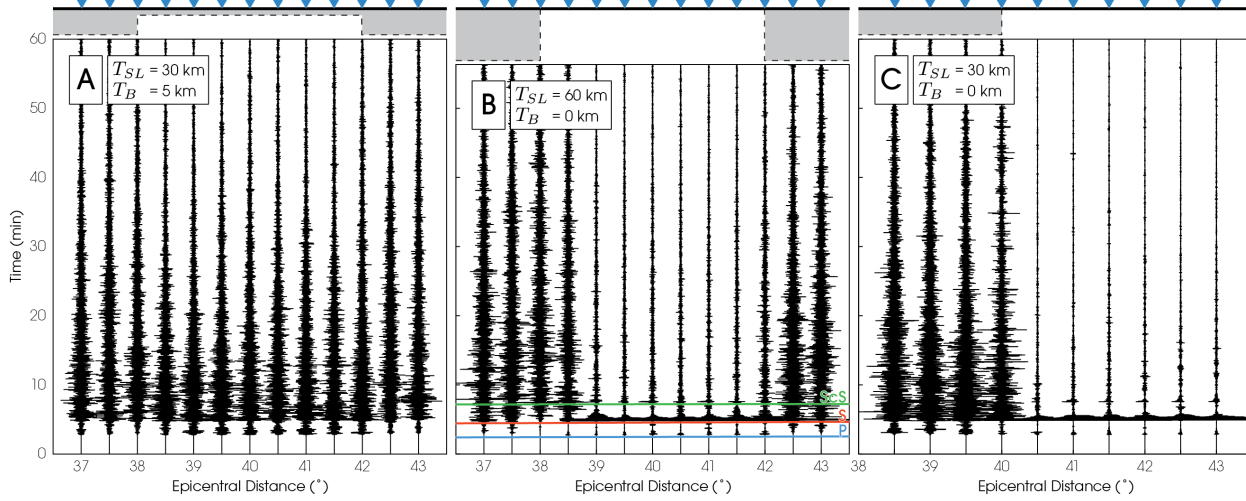


Figure 5.2: Synthetic seismograms recorded for a deep source and three different megaregolith structures: (A) 120 km basin with  $T_{SL} = 30 \text{ km}$  and  $T_B = 5 \text{ km}$ , (B) 120 km basin with  $T_{SL} = 60 \text{ km}$  and  $T_B = 0 \text{ km}$ , and (C) 1200 km basin (only showing the edge) with  $T_{SL} = 30 \text{ km}$  and  $T_B = 0 \text{ km}$ , where  $T_{SL}$  is the thickness of the megaregolith layer surrounding the impact structure, and  $T_B$  the thickness of the megaregolith in the structure itself. Figure format as in Figure 5.1. Theoretical P (blue), S (red), and ScS (green) arrivals are plotted on B.

#### *5.4. Discussion and Conclusions*

---

golith. In contrast, the signals shown in Figure 5.2B indicate that to record coda with substantially reduced scattering we now have to move at least 30 km, or half the scattering layer thickness ( $T_{SL}/2$ ) away from the basin edge, toward the basin center. At stations beyond that distance, the P- and S-wave arrivals, as well as the ScS core phase, are identifiable.

For larger basins such as that shown in Figure 5.2C the records of deep events at stations in the basin interior are cleaner than those for the same megaregolith structure but smaller basin diameter (Figure 5.1B). Note that only one edge of the basin is shown in Figure 5.2C. In particular, the basin is now large enough that the effects of leaked energy seen near the basin edges, and resulting from the surrounding thick megaregolith diminish significantly toward the center of the basin.

## **5.4 Discussion and Conclusions**

The results indicate that the total scattering observed in the recorded signals is minimized for seismic sources located beneath the megaregolith. Seismic energy from such sources does not undergo the source-side scattering that affects impact events and any lunar quakes occurring within the scattering layer. Deep moonquakes are known to occur in the lower lunar mantle, and occur repeatedly, with tidal periodicities at distinct locations [Lammlein et al., 1974; Nakamura, 2005; Bulow et al., 2005, 2007]. They are thus ideal sources for better characterization of the lunar interior in future lunar seismic experiments. In addition some of the shallow moonquakes observed in the APSE data may occur beneath the scattering layer, either in the lowermost crust or in the upper mantle [Nakamura et al., 1979]. These events are rare, only 28 shallow quakes were recorded over the 7 year APSE duration, however a few were of large magnitude and thus it would be desirable to record such types of events during any new lunar seismic survey.

Basins with a much thinner megaregolith layer than the surrounding region ( $T_B \ll T_{SL}$ ) can yield seismograms at stations located in the basin that have significantly less scattered energy than signals recorded at stations on the surrounding terrain. Furthermore, the results indicate that the effect of leaked energy from the surrounding thick megaregolith is greatly reduced for receivers located at a distance

#### *5.4. Discussion and Conclusions*

---

away from the basin edge (toward the basin center) of at least half the thickness of the surrounding megaregolith,  $T_{SL}/2$ . As a result, even small basins could allow identification of direct wave arrivals, and potentially of secondary wave arrivals as long as the megaregolith layer beneath the basin itself is thin. I note that in my simulations I did not change the size-frequency distribution of scatterers, or their overall number density for the case of a thin megaregolith layer beneath the basin (Figure 5.2A). In reality both of these properties will be different in this layer, especially for young basins where we would expect a thin megaregolith with a lower scatterer number density overall. This effect will further act to reduce the scattering recorded at stations located in the basin. However, large basins will be better suited to detect primary and secondary wave arrivals as it is easier to locate stations away from the basin edge yielding seismograms less affected by leaked, scattered energy.

In my models, the effects of the dominantly forward-scattering vs. back-scattering are seen for stations recorded around the edges of a smaller basin (as seen in Figure 5.1B and Figure 5.2B). The receivers located at epicentral distances of  $38^\circ$  and  $42^\circ$  both sit on the edge of the basin, however, the seismogram at  $38^\circ$  is more affected by forward-scattered energy from the edge of the basin (from energy traveling away from the source located at  $0^\circ$ ). In contrast the seismogram at the receiver at  $42^\circ$  is less scattered because there is less back-scattered energy from that edge of the basin. As noted earlier, in my models the average impedance contrast of the scatterers of  $\pm 35\%$  of the background values favors forward scattering and is a value likely representative of that for annealed fractures or boundaries between different lithologies. Impedance contrasts representative of voids (corresponding to the high porosity inferred from GRAIL data for at least the uppermost megaregolith [Wieczorek et al., 2013; Besserer et al., 2013]) are larger, so the scattering is more isotropic and the seismogram recorded at  $42^\circ$  would show more scattering than that seen in Figures 5.1B and 5.2B.

The following effects were neglected in my models to minimize computational requirements, but they could have important effects on the scattering characteristics of the recorded signals: (1) Surface topography. This could intensify or decrease scattering, especially near basin edges or near the seismic receivers (e.g., Schmerr et al. [2011]). (2) Lateral variations in seismic velocities and densities. Large

#### *5.4. Discussion and Conclusions*

---

impacts can affect the velocity profile beneath the impact site (e.g., crustal thinning, mantle uplifting, petrological evolution of melt material [Melosh, 1996; Ivanov et al., 2010]). These lateral impedance contrasts with the region surrounding the structure could focus or scatter seismic energy into or out of the basins. (3) Noise (instrumental or seismic). The presence of background seismic noise could hinder the identification of the emergent body wave arrivals as is the case with the APSE data (e.g., Lognonné et al. [2003]).

In conclusion, younger impact events, if large enough, can redistribute ejecta and reduce the thickness of the megaregolith at the site of impact. Seismic signals recorded at stations located in the basin from deep moonquake sources or from shallow moonquakes located beneath the megaregolith show substantially reduced scattering relative to signals recorded at stations outside the basin. The seismograms show clearer P and S-wave arrivals and can allow identification of secondary phases. Consequently, these impact sites should be considered as potential seismometer locations in future seismic surveys of the lunar interior. One such ideal location for future lunar seismic surveys would be the far-side Schrödinger basin. This basin is one of the youngest basins, only older than Orientale basin [Wilhelms, 1987], suggesting a minimal accumulation of ejecta material from subsequent large impacts. It has also already been identified as a high priority target for addressing several other aspects of lunar science such as lower crust and upper mantle compositions, impact chronology, etc. (e.g. Kohout et al. [2009]; Flahaut et al. [2012]).

# Chapter 6

## Conclusions

The Apollo Passive Seismic Experiment was the first seismic survey installed on the surface of a planetary body other than the Earth. It recorded more than seven years of continuous data, from which over 12,000 individual seismic events were identified. One of the prominent features shared by the seismic signals generated by these events is the very long-duration scattered coda train that obscures most wave arrivals except for some of the higher amplitude P- and S-waves. Although more than 40 years of analysis of this dataset has provided us with fundamental understanding of the constitution and structure of the lunar interior, no study has systematically looked at the information stored in these scattered codas. The work presented in this thesis aimed at addressing this gap in analysis of the APSE data, as well as developing a new understanding of seismic energy propagation in highly scattering bodies like the Moon, and potentially other terrestrial planets, moons and asteroids.

The combined conclusions of the four studies comprising this thesis show that the coda of scattered seismic signals can yield important information regarding the scattering and attenuation properties of highly scattering planetary bodies, and that coda investigations should be included in future analyses of scattered seismic data. The modeling method I have developed can be used to assess the effects of internal structures on the seismic coda and to model synthetics seismograms for various surface environments. In this chapter, I summarize my research work and the resulting conclusions (section 6.1). I then briefly review and address the main science questions I aimed to answer with this work (section 6.2). I conclude with a short discussion of potential future research avenues that could build on the work presented in this thesis (section 6.3).

### *6.1. Summary*

---

## **6.1 Summary**

Chapter 2 presents the first comprehensive analysis of scattering in the lunar seismic data. Whereas previous studies analyzed the amplitude decay of single impact events (e.g. Latham et al. [1970b]), my work systematically looked at the decay properties of all seismic event types (impacts and moonquakes), in several frequency bands, to more fully characterize scattering on the Moon as a function of source depth, frequency and epicentral distance. The results support the idea that scattering dominantly occurs in the near surface megaregolith layer. I also showed that all frequencies sampled by the APSE instruments are affected by high levels of scattering, but that the observed scattering intensity increases with increasing frequencies. This suggests that the megaregolith is composed of scatterers over a wide range of scale lengths, with many more small scale scatterers than large scale ones. The study also underlines the importance of local structure on the recorded signals for events with short epicentral distances. Station 16, which sits on top of a thick crust with an assumed thicker megaregolith recorded signals with longer decay times (i.e. more scattered signals) than station 15 for example, which is located in a basin with a thinner crust and megaregolith. The results from this study will be useful for the development of future seismic surveys, which should focus the instrument sensitivity on lower frequencies that are potentially less affected by scattering. The coda decay times measured in this study are also important constraints for studies attempting to model lunar interior structures, as was done in the study presented in Chapter 4.

Chapter 3 details the numerical method I have developed to model the transmission of seismic energy in highly scattering environments (the PHONON1D method). This method is based on the phonon method of Shearer and Earle [2004], which I have adapted to the lunar context and refined by implementing isotropic scattering, user-defined scatterer scale-length distributions, as well as frequency-dependent and phase-dependent intrinsic attenuation. This chapter also presents the first study investigating the effects of large scale velocity, scattering and attenuation structures on the generation and decay properties of scattered seismic coda. Using the PHONON1D method, I have generated synthetic traces for a range of planetary interiors with varying seismic velocity, scattering and attenuation struc-

## 6.1. Summary

---

tures. Results show that the main controls on the coda decay times are the seismic velocity profiles (i.e. substantially increased decay times when a crust and a thin low-velocity regolith are present), the event source depth (larger decay times for shallower events), as well as the intrinsic attenuation as a function of depth and frequency.

In Chapter 4 I used the coda decay constraints from Chapter 2, along with the PHONON1D method detailed in Chapter 3, to identify a suite of lunar interior models that generate synthetic seismic signals that share the decay properties of the APSE data. I first modeled the APSE instrument effects (narrow frequency bands and 10-bit digitization), and the 1-bit lunar seismic noise in the data. By comparing decay times measured with noise-free signals with those measured on the APSE-corrected signals I demonstrated that APSE instrument effects did not significantly alter the decay times. Consequently, the decay times from Chapter 2 are representative of the lunar interior structures and can be used as constraints for modeling work. No other work to date has investigated the effect of 10-bit digitization and of the 1-bit noise on the lunar seismograms relative to the signals that could be recorded by modern broadband 32-bit instrumentation (to which our clean synthetic signals are equivalent). I then generated synthetic signals for 32 distinct lunar interior models, all of which used a seismic velocity profile with a crust and a thin regolith, that focuses the scattered energy back towards the surface and into the scattering layer. This creates a very highly scattering environment which generates decay times on the order of the ones measured in the APSE data. Results indicate that in such a very highly scattering environment, first order changes in the scattering length scales do not produce an effect on the median decay time values. Thus, median  $\tau_d$  values are not the best tool for identifying the lunar scattering structure length scales, but this could be best achieved by investigating the variations in the  $d\tau_d/d\Delta$  slopes. In such environments, the main control on decay times appears to be the intrinsic attenuation levels. Results show that only intrinsic attenuation values larger than the ones previously published could yield decay times that matched the APSE decay times. However, a more systematic exploration of the parameter space is needed to constrain lunar attenuation and scattering structures compatible with the APSE data.

In Chapter 5, I have tested the effects of a laterally varying megaregolith thick-

## 6.2. *The Science Questions Answered*

---

ness on the recorded seismic signals. The aim of this study was to identify locations on the lunar surface that minimize the scattering observed in the data, and maximize the science returns of future lunar seismic surveys. Based on the results, I propose that the ideal receiver locations are in younger impact events, that have less accumulated ejecta, a thinner megaregolith and likely thinned crust (as a result of the impact process). Receivers should be placed at a distance away from the basin edge that is at least half of the thickness of the megaregolith surrounding the basin. Synthetic seismograms showed much cleaner signals for seismic source depths located beneath the megaregolith layer (deep moonquakes, and potentially some shallow moonquakes). Such events do not experience the same intensive source-side scattering that affects surface impacts. In these cases, the P- and S-wave arrivals are much more impulsive and easier to pick, and useful secondary phases (e.g. core phases) have a higher chance of being identified.

## 6.2 The Science Questions Answered

**Q1:** What constraints on the interior structure of the Moon or of other highly scattering bodies can we infer from analyzing the scattered coda of recorded seismic signals?

From the analysis of the APSE scattered codas, we can confirm that the scattering of seismic energy dominantly occurs in a near-surface global layer (i.e. the megaregolith). Results suggest that this layer has a size-distribution of ejecta blocks that has many more small scale than large scale scatterers. Using the decay properties of the APSE codas as constraint for models of seismic energy propagation in highly scattering media, we can also show that intrinsic attenuation levels in shallow lunar layers are probably lower than what has been suggested in past literature. As such, the analysis of scattered coda of recorded seismic signals provide valuable information pertaining to shallow scattering and intrinsic attenuation structures of highly scattering bodies.

**Q2:** What are the effects of seismic velocity, intrinsic attenuation and scattering structures on the scattered coda of seismic signals?

### *6.3. Future Work*

---

Velocity structures that tend to focus seismic energy near the surface and into the scattering layer, will dramatically increase the intensity of the observed scattering (i.e. increased coda decay times). Such structures can be near-surface low velocity layers (e.g. thin regolith and/or crust), as well as positive gradients of seismic velocities with depth. When such structures are present, we found that the main control on the coda decay properties is the intrinsic attenuation levels at shallow depths. Lower intrinsic attenuation will lead to longer decay times, whereas higher attenuation will lead to shorter decay times. Where no such structures are found (e.g. large undifferentiated asteroid), the thickness of the scattering layer, as well as the number density of scatterers will also affect the coda. A thick scattering layer and a high number density lead to longer decay times.

- Q3:** Are there locations on the lunar surface that could minimize the intensity of scattering in recorded signals, and maximize science returns of future seismic surveys?

Yes. Locations away from the edges of large impact structures, with a thin crust and a thin megaregolith, are ideal for seismic receivers. Younger impact structures are better suited candidates because less ejecta material from subsequent impacts has accumulated, leading to a thinner megaregolith layer in the structure. Modeling work shows that moving away from the basin edges by a distance that is equivalent to half the thickness of the surrounding megaregolith is enough to minimize the effects due to leaked scattered energy from the surrounding megaregolith. An example of such a location on the Moon would be inside the far-side Schrödinger basin.

## **6.3 Future Work**

Study of seismic scattering is not new, and a wide range of past studies have developed theoretical approaches and methods to better understand scattering of seismic energy in a terrestrial context. However no such study has investigated seismic scattering on a global level in environments where scattering processes dominate, as on the Moon. As such, my work provides a stepping stone for future studies

### 6.3. Future Work

---

of highly scattered seismic data, and for further investigations to better understand the relationship between surface and internal structures and seismic coda.

For example, large impacts on the lunar surface can result in important subsurface structure modifications (e.g. crustal thinning, mantle uplift, lithological phase changes). The development of numerical models integrating surface topography and radial and lateral variations in seismic velocities (2-D velocity profiles) could test the effects of these lateral structures on seismic coda and assess whether these structures are reflected in the recorded signals.

Furthermore, a fully 3-D numerical model could be used to investigate seismic energy propagation in smaller, non-spherical bodies (e.g. asteroids). An understanding of scattering on such bodies will allow us to use future seismic studies to better image and understand their interior structures. Methods already exist that simulate seismic energy transmission in 3-D media. However, similarly to the 1-D case, computation costs and time for methods calculating the solution to the wave equation (e.g. SPECFEM3D) at the short length-scales (down to meter length-scales) and frequencies (10s of Hz) required to appropriately model the lunar context are still too high today (at least on the kind of computing tools used for this thesis work). However, some ray tracing methods in a 3-D media do exist (e.g. Gjøystdal et al. [2002]) that are mostly used nowadays to image seismic data in oil and mineral exploration studies on local and regional scales. These methods could be adapted to model seismic energy propagation in highly scattering environments using a similar approach to the one presented here.

Finally, questions still remain about the full relationship between intrinsic attenuation ( $Q_i$ ), the scattering processes (often expressed as  $Q_s$ ), the resulting wave amplitudes, and coda decay times ( $Q_c$ ), either in low or high scattering environments. For example, studies that assessed the levels of intrinsic attenuation on the Moon mostly looked at the changes in the signals' amplitude (or power) as a function of distance and frequency (e.g. Nakamura et al. [1976]; Nakamura and Koyama [1982]). The main assumption was that variations in amplitude are caused by intrinsic attenuation processes and geometrical spreading. However, I observed in my modeling work that signal amplitude as a function of epicentral distance could vary greatly for models with similar velocity and intrinsic attenuation profiles, but with different scattering properties. This strongly suggests that

### *6.3. Future Work*

---

to properly measure intrinsic attenuations levels with seismic data in a lunar-like environment, one must understand how scattering also affects the signals' amplitudes. This might explain why lower attenuation values than those proposed in the literature were needed in my modeling to achieve decay times that are comparable to those observed in the lunar data. Consequently, more modeling work using the PHONON1D code could shed light on this issue and expand our understanding of seismic scattering.

# Bibliography

- K. Aki. Analysis of the seismic coda of local earthquakes as scattered waves. *J. Geophys. Res.*, 74(2):615–631, 1969.
- K. Aki and B. Chouet. Origin of coda waves: source, attenuation, and scattering effects. *J. Geophys. Res.*, 80(23):3322–3342, 1975.
- K. Aki and P. G. Richards. *Quantitative Seismology*. University Science Books, 2nd edition, 2002.
- A. Ben-Menahem and S. J. Singh. *Seismic Waves and Sources*. Courier Dover Publications, 2nd edition, 2000.
- J. Besserer, F. Nimmo, M. Wieczorek, W. Kiefer, J. Andrews-Hanna, and M. Zuber. Theoretical and observational constraints on lunar mega-regolith thickness. *44th Lunar and Planetary Science Conference*, (2463), 2013.
- S. Bhattacharya. Exact solutions of the equation for the free torsional oscillations of an inhomogeneous sphere. *Bull. Seismol. Soc. Am.*, 62(31-38), 1972.
- S. Bhattacharya. Earth flattening transformation for P-SV waves. *Bull. Seismo. Soc. Am.*, 86:1979–1982, 1996.
- S. Bhattacharya. Synthetic seismograms in a spherical Earth using exact flattening transformation. *Geophys. Res. Lett.*, 32(L21303), 2005. doi: 10.1029/2005GL024152.
- J.-F. Blanchette-Guertin, C. L. Johnson, and J. F. Lawrence. Investigation of scattering in lunar seismic coda. *J. Geophys. Res.*, 117(E06003), 2012. doi: 10.1029/2011JE004042.

## Bibliography

---

- J. Boatwright and J. Fletcher. The partition of radiated energy between P and S waves. *Bull. Seismol. Soc. Am.*, 74(2):361–376, 1984.
- R. C. Bulow, C. L. Johnson, and P. M. Shearer. New events discovered in the Apollo lunar seismic data. *J. Geophys. Res.*, 110(E10003), 2005. doi: 10.1029/2005JE002414.
- R. C. Bulow, C. L. Johnson, B. G. Bills, and P. M. Shearer. Temporal and spatial properties of some deep moonquake clusters. *J. Geophys. Res.*, 112:E09003, 2007. doi: 10.1029/2006JE002847.
- F. Dahlen. Finite-frequency sensitivity kernels for boundary topography perturbations. *Geophysical Journal International*, 162(2):525–540, 2005.
- A. M. Dainty, M. N. Toksöz, K. R. Anderson, P. Pines, Y. Nakamura, and G. V. Latham. Seismic scattering and shallow structure of the Moon in Oceanus Procellarum. *The Moon*, 9:11–29, 1974.
- J. Dorman, S. Evans, Y. Nakamura, and G. Latham. On the time-varying properties of the lunar seismic meteoroid population. *Proc. Lunar Planet. Sci. Conf. 9th*, pages 3615–3626, 1978.
- P. S. Earle and P. M. Shearer. Distribution of fine-scale mantle heterogeneity from observations of Pdiff coda. *Bull. Seismol. Soc. Am.*, 91(6):1875–1881, 2001.
- J. Flahaut, J. F. Blanchette-Guertin, C. Jilly, P. Sharma, A. Souchon, W. van Westrenen, and D. A. Kring. Identification and characterization of science-rich landing sites for lunar lander missions using integrated remote sensing observations. *Advances in Space Research*, 50(12):1647–1665, Dec 2012. doi: 10.1016/j.asr.2012.05.020.
- K. Fuchs. The reflection of spherical waves from transitions zones with arbitrary depth-dependent elastic moduli and density. *Journal of Physics of the Earth*, 16 (Special Issue):27–41, 1968.
- K. Fuchs and G. Müller. Computation of synthetic seismograms with the reflectivity method and comparison with observations. *Geophysical Journal of the Royal Astronomical Society*, 23(4):417–433, 1971.

## Bibliography

---

- J. Gagnepain-Beyneix, P. Lognonné, H. Chenet, D. Lombardi, and T. Spohn. A seismic model of the lunar mantle and constraints on temperature and mineralogy. *Phys. Earth Planet. Inter.*, 159:140–166, 2006.
- R. F. Garcia, J. Gagnepain-Beyneix, S. Chevrot, and P. Lognonné. Very preliminary reference Moon model. *Phys. Earth Planet. Inter.*, 188:96–113, 2011. doi: 10.1016/j.pepi.2011.06.015.
- H. Gjøystdal, E. Iversen, R. Laurain, I. Lecomte, V. Vinje, and K. Åstebøl. Review of ray theory applications in modelling and imaging of seismic data. *Studia geophysica et geodaetica*, 46(2):113–164, 2002.
- P. Goldstein and A. Snoke. SAC Availability for the IRIS Community. *Incorporated Institutions for Seismology Data Management Center Electronic Newsletter*, 2005.
- P. Goldstein, D. Dodge, M. Firpo, and L. Minner. SAC2000: Signal processing and analysis tools for seismologists and engineers. *Invited contribution to “The IASPEI International Handbook of Earthquake and Engineering Seismology”*, 2003.
- A. Gusev and I. Abubakirov. Monte-Carlo simulation of record envelope of a near earthquake. *Phys. Earth Planet. Inter.*, (49):30–36, 1987.
- W. K. Hartmann. Ancient lunar mega-regolith and subsurface structure. *Icarus*, 18 (4):634–636, 1974.
- L. L. Hood, A. Zakharian, J. Halekas, D. L. Mitchell, R. P. Lin, M. H. Acuna, and A. B. Binder. Initial mapping and interpretation of lunar crustal magnetic anomalies using Lunar Prospector magnetometer data. *J. Geophys. Res.*, 106 (E11):27825–27839, 2001.
- P. Horvath, G. V. Latham, Y. Nakamura, and H. Dorman. Lunar near-surface shear wave velocities at the Apollo landing sites as inferred from spectral amplitude ratios. *J. Geophys. Res.*, 85(B11):6572–6578, 1980.
- F. Hörz. Lunar surface processes. *The Lunar Sourcebook*, pages 62–120, 1991.

## Bibliography

---

- M. Hoshiba. Simulation of coda wave envelope in depth dependent scattering and absorption structure. *Geophys. Res. Lett.*, 21(25):2853–2856, 1994.
- K. Housen and R. M. Schmidt. Laboratory simulations of large scale fragmentation events. *Icarus*, 94:180–190, 1991.
- K. R. Housen, R. M. Schmidt, and K. A. Holsapple. Crater ejecta scaling laws: Fundamental forms based on dimensional analysis. *J. Geophys. Res.*, 88(B3): 2485–2499, 1983.
- B. Ivanov, H. Melosh, and E. Pierazzo. Basin-forming impacts: Reconnaissance modeling. *Geological Society of America Special Papers*, 465:29–49, 2010.
- A. Jin and K. Aki. Spatial and temporal correlation between coda Q and seismicity in China. *Bull. Seismol. Soc. Am.*, 78(2):741–769, 1988.
- B. Jolliff, J. Gillis, L. Haskin, R. Korotev, and M. A. Wieczorek. Major lunar crustal terranes: Surface expressions and crust-mantle origins. *J. Geophys. Res.*, 105(E2):4197–4216, 2000.
- A. Khan and K. Mosegaard. An inquiry into the lunar interior: A nonlinear inversion of the Apollo lunar seismic data. *J. Geophys. Res.*, 107(E6):19–44, 2002.
- A. Khan, K. Mosegaard, and K. Rasmussen. A new seismic velocity model for the Moon from a Monte Carlo inversion of the Apollo lunar seismic data. *Geophys. Res. Lett.*, 27(11):1591–1594, 2000.
- R. L. Klima, C. M. Pieters, J. W. Boardman, R. O. Green, J. W. Head, P. J. Isaacson, J. F. Mustard, J. W. Nettles, N. E. Petro, M. I. Staid, J. M. Sunshine, L. A. Taylor, and S. Tompkins. New insights into lunar petrology: Distribution and composition of prominent low-Ca pyroxene exposures as observed by the Moon Mineralogy Mapper (m3). *J. Geophys. Res.*, 116(E00G06), 2011. doi: 10.1029/2010JE003719.
- M. Knapmeyer. TTBox: A Matlab toolbox for the computation of 1D teleseismic travel times. *Seismological Research Letters*, 75(6):726–733, 2004.

## Bibliography

---

- T. Kohout, K. OSullivan, A. Losiak, K. G. Thaisen, S. Weider, and D. A. Kring. Scientific opportunities for human exploration of the Moon’s Schrödinger basin. *40th Lunar and Planetary Science Conference*, (1572), Jan 2009.
- R. L. Kovach, J. S. Watkins, and T. Landers. Active Seismic Experiment. *Apollo 14 Preliminary Science Report*, (NASA SP-272):163–174, 1971.
- R. L. Kovach, J. S. Watkins, and P. Talwani. Active Seismic Experiment. *Apollo 16 Preliminary Science Report*, (NASA SP-315), 1972.
- O. Kuskov, V. Kronrod, and L. Hood. Geochemical constraints on the seismic properties of the lunar mantle. *Phys. Earth Planet. Inter.*, 134(3):175–190, 2002. doi: 10.1016/S0031-9201(02)00156-5.
- D. R. Lammlein, G. V. Latham, J. Dorman, Y. Nakamura, and M. Ewing. Lunar seismicity, structure, and tectonics. *Reviews of Geophysics and Space Physics*, 12(1):1–21, 1974.
- G. V. Latham, M. Ewing, F. Press, G. Sutton, J. Dorman, Y. Nakamura, M. N. Toksöz, R. Wiggins, J. Derr, and F. Duennbier. Passive Seismic Experiment. *Apollo 12 Preliminary Science Report*, (NASA SP-235):39–54, 1970a.
- G. V. Latham, M. Ewing, F. Press, G. Sutton, J. Dorman, Y. Nakamura, M. N. Toksöz, R. Wiggins, J. Derr, and F. Duennbier. Passive seismic experiment. *Science*, 167(3918):455–457, 1970b.
- G. V. Latham, M. Ewing, J. Dorman, D. Lammlein, F. Press, M. N. Toksöz, G. Sutton, F. Duennbier, and Y. Nakamura. Moonquakes. *Science*, 174(4010):687–692, 1971.
- G. V. Latham, J. Dorman, F. Duennbier, M. Ewing, D. Lammlein, and Y. Nakamura. Moonquakes, meteroids, and the state of the lunar interior. *Geochemica et Cosmochimica Acta*, 3(Supp. 4):2515–2527, 1973.
- P. Lognonné, J. Gagnepain-Beyneix, and H. Chenet. A new seismic model of the Moon: implications for structure, thermal evolution and formation of the Moon. *Earth Planet. Sci. Lett.*, 211(1-2):27–44, 2003.

## Bibliography

---

- P. Lognonné, M. Le Feuvre, C. Johnson, and R. Weber. Moon meteoritic seismic hum: Steady state prediction. *J. Geophys. Res.*, 114(E12003), 2009. doi: doi:10.1029/2008JE003294.
- L. Margerin, M. Campillo, and B. van Tiggelen. Radiative transfer and diffusion of waves in a layered medium: new insight into coda Q. *Geophys. J. Int.*, 134: 596–612, 1998.
- L. Margerin, M. Campillo, N. M. Shapiro, and B. van Tiggelen. Residence time of diffuse waves in the crust as a physical interpretation of coda Q: application to seismograms recorded in Mexico. *Geophys. J. Int.*, 138:343–352, 1999.
- L. Margerin, M. Campillo, and B. V. Tiggelen. Monte Carlo simulation of multiple scattering of elastic waves. *J. Geophys. Res.*, 105(B4):7873–7892, 2000.
- T. R. McGetchin, M. Settle, and J. W. Head. Radial thickness variation in impact crater ejecta: implications for lunar basin deposits. *Earth Planet. Sci. Lett.*, 20 (2):226–236, 1973.
- H. J. Melosh. *Impact Cratering: A Geologic Process*. Oxford University Press, 1996.
- B. Mitchell. Anelastic structure and evolution of the continental crust and upper mantle from seismic surface wave attenuation. *Rev. Geophys.*, 33(4):441–462, 1995.
- Y. Nakamura. Seismic energy transmission in an intensively scattering environment. *J. Geophys.*, 43:389–399, 1977.
- Y. Nakamura. Seismic velocity structure of the lunar mantle. *J. Geophys. Res.*, 88 (B1):677–686, 1983.
- Y. Nakamura. Catalog of lunar seismic data from Apollo Passive Seismic Experiment on 8-mm video cassette (exabyte) tapes. *UTIG Technical Report No. 118*, 1992.
- Y. Nakamura. Farside deep moonquakes and deep interior of the Moon. *J. Geophys. Res.*, 110(E01001), 2005. doi: 10.1029/2004JE002332.

## Bibliography

---

- Y. Nakamura and J. Koyama. Seismic Q of the Lunar Upper Mantle. *J. Geophys. Res.*, 87(B6):4855–4861, 1982.
- Y. Nakamura, J. Dorman, F. Duennebier, M. Ewing, D. R. Lammlein, and G. V. Latham. High-frequency lunar teleseismic events. *Proceedings of the Fifth Lunar Conference*, 3:2883–2890, 1974.
- Y. Nakamura, J. Dorman, F. Duennebier, D. R. Lammlein, and G. V. Latham. Shallow lunar structure determined from the Passive Seismic Experiment. *The Moon*, 13:57–66, 1975.
- Y. Nakamura, F. K. Duennebier, G. V. Latham, and H. J. Dorman. Structure of the lunar mantle. *J. Geophys. Res.*, 81(26):4818–4824, 1976.
- Y. Nakamura, G. V. Latham, H. J. Dorman, A.-B. K. Ibrahim, J. Koyama, and P. Horvath. Shallow moonquakes: Depth, distribution and implications as to the present state of the lunar interior. *Proc. Lunar Planet. Sci. Conf. 10th*, pages 2299–2309, 1979.
- Y. Nakamura, G. Latham, and H. Dorman. How we processed Apollo lunar seismic data. *Phys. Earth Planet. Inter.*, 21(2):218–224, 1980.
- J. O’Keefe and T. Ahrens. The size distributions of fragments ejected at a given velocity from impact craters. *International Journal of Impact Engineering*, 5(1): 493–499, 1987.
- N. E. Petro and C. M. Pieters. Surviving the heavy bombardment: Ancient material at the surface of South Pole-Aitken Basin. *J. Geophys. Res.*, 109(E06004), 2004. doi: 10.1029/2003JE002182.
- N. E. Petro and C. M. Pieters. The lunar-wide effects of basin ejecta distribution on the early megaregolith. *Meteorit. Planet. Sci.*, 43(8):1517–1529, 2008.
- R. J. Pike. Ejecta from large craters on the Moon: Comments on the geometric model of McGetchin et al. *Earth Planet. Sci. Lett.*, 23(3):265–271, 1974.

## Bibliography

---

- J. Przybilla, U. Wegler, and M. Korn. Estimation of crustal scattering parameters with elastic radiative transfer theory. *Geophysical Journal International*, 178(2):1105–1111, Aug 2009. doi: 10.1111/j.1365-246X.2009.04204.x.
- E. V. Ryan and H. J. Melosh. Impact fragmentation: From the laboratory to asteroids. *Icarus*, 133(1):1–24, 1998.
- H. Sato and M. C. Fehler. *Seismic wave propagation and scattering in the heterogeneous Earth*. Springer, 1st edition, 1998.
- N. C. Schmerr, E. Matzel, and S. R. Ford. The effect of free-surface topography on seismic waves in the Moon. *42nd Lunar and Planetary Science Conference*, (1961), 2011.
- P. Schultz and W. Mendell. Orbital infrared observations of lunar craters and possible implications for impact ejecta emplacement. *Proc. Lunar Planet. Sci. Conf. 9th*, pages 2857–2883, 1978.
- C. Sens-Schönfelder and E. Larose. Lunar noise correlation, imaging and monitoring. *Earthq Sci*, 23(5):519–530, 2010. doi: 10.1007/s11589-010-0750-6.
- P. Shearer. Deep Earth structure – Seismic scattering in the deep Earth. *Treatise on geophysics*, 1:695–729, 2007.
- P. M. Shearer and P. S. Earle. The global short-period wavefield modelled with a Monte Carlo seismic phonon method. *Geophys. J. Int.*, 158(3):1103–1117, 2004. doi: 10.1111/j.1365-246X.2004.02378.x.
- Y. Shkuratov and N. Bondarenko. Regolith layer thickness mapping of the Moon by radar and optical data. *Icarus*, 149(2):329–338, 2001. doi: doi:10.1006/icar.2000.6545.
- N. M. Short and M. L. Forman. Thickness of impact crater ejecta on the lunar surface. *NASA Technical Memorandum*, 1970.
- D. E. Smith, M. T. Zuber, G. A. Neumann, F. G. Lemoine, E. Mazarico, M. H. Torrence, J. F. McGarry, D. D. Rowlands, J. W. Head, T. H. Duxbury, O. Aharonson, P. G. Lucey, M. S. Robinson, O. S. Barnouin, J. F. Cavanaugh, X. Sun, P. Liiva,

## Bibliography

---

- D.-D. Mao, J. C. Smith, and A. E. Bartels. Initial observations from the Lunar Orbiter Laser Altimeter (LOLA). *Geophys. Res. Lett.*, 37(L18204), 2010. doi: 10.1029/2010GL043751.
- T. Thompson, W. Roberts, W. Hartmann, R. Shorthill, and S. Zisk. Blocky craters: Implications about the lunar megaregolith. *The moon and the planets*, 21(3): 319–342, 1979.
- T. W. Thompson, B. A. Campbell, R. R. Ghent, and B. R. Hawke. Rugged crater ejecta as a guide to megaregolith thickness in the southern nearside of the Moon. *Geology*, 37(7):655–658, 2009. doi: 10.1130/G25565A.1.
- M. N. Toksöz, F. Press, K. Anderson, A. Dainty, G. Latham, M. Ewing, J. Dorman, D. Lammlein, Y. Nakamura, G. Sutton, and F. Duennebier. Velocity structure and properties of the lunar crust. *Proceedings of the Conference on Lunar Geophysics*, pages 490–504, 1971.
- M. N. Toksöz, A. M. Dainty, S. C. Solomon, and K. R. Anderson. Velocity structure and evolution of the Moon. *Proceedings of the Fourth Lunar Science Conference*, 3:2529–2547, 1973.
- M. Tsujiura. Spectral analysis of the coda waves from local earthquakes. *Bulletin of the Earthquake Research Institute*, 53:1–48, 1978.
- L. P. Vinnik, H. Chenet, J. Gagnepain-Beyneix, and P. Lognonné. First seismic receiver functions on the Moon. *Geophys. Res. Lett.*, 28(15):3031–3034, 2001.
- R. Weber, P.-Y. Lin, E. Garnero, Q. Williams, and P. Lognonné. Seismic detection of the lunar core. *Science*, 331(6015):309–312, 2011.
- M. A. Wieczorek. The interior structure of the Moon: What does geophysics have to say? *Elements*, 5(1):35–40, 2009. doi: 10.2113/gselements.5.1.35.
- M. A. Wieczorek, G. A. Neumann, F. Nimmo, W. S. Kiefer, G. J. Taylor, H. J. Melosh, R. J. Phillips, S. C. Solomon, J. C. Andrews-Hanna, S. W. Asmar, A. S. Konopliv, F. G. Lemoine, D. E. Smith, M. M. Watkins, J. G. Williams, and M. T. Zuber. The crust of the Moon as seen by GRAIL. *Science*, 339(6120):671–675, 2013. doi: 10.1126/science.1231530.

- D. E. Wilhelms. *The geologic history of the Moon*. USGS, 1987.
- K. Yoshimoto. Monte Carlo simulation of seismogram envelopes in scattering media. *J. geophys. Res.*, 105(B3):6153–6161, 2000.
- K. Yoshimoto and A. Jin. Coda Energy Distribution and Attenuation. *Advances in Geophysics: Earth Heterogeneity and Scattering Effects on Seismic Waves*, 50: 265–299, 2008. doi: 10.1016/S0065-2687(08)00010-1.

## Appendix A

# Coefficients for Solid-Solid, Free Surface and Solid-Liquid Interfaces

The equations used in the calculation of the amplitude reflection and transmission coefficients at the free surface and at solid-liquid interfaces are from Ben-Menahem and Singh [2000]. Equations for coefficients at solid-solid interfaces are from Aki and Richards [2002].

In all equations, the first letter ( $\acute{P}$  or  $\acute{S}$ ) indicates the incident ray. An acute accent on the second letter ( $\acute{P}$  or  $\acute{S}$ ) indicates a transmitted ray, whereas a grave accent ( $\grave{P}$  or  $\grave{S}$ ) indicates a reflected ray. The letter ( $P$  or  $S$ ) represents the polarities of the incident, transmitted and reflected rays (Figure A.1). Note that we keep the same formulation for upward- and downward-incident rays.

### A.1 P-SV at Free Surface

From Ben-Menahem and Singh [2000]:

$$D_1 = \left( \frac{\beta_1}{\alpha_1} \right) \sin 2i_1 \sin 2j_1 + \cos^2 2j_1$$

### A.1. P-SV at Free Surface

---

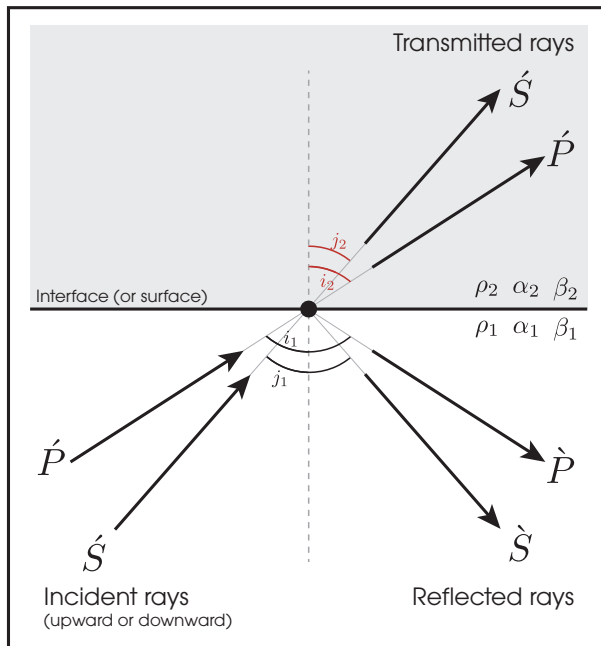


Figure A.1: Notations used in the transmission and reflection coefficient equations. Upward- and downward-incident rays are indicated with a first  $\acute{P}$  or  $\acute{S}$ , depending on the initial polarization. The second letter indicates transmitted rays ( $\acute{\grave{P}}$  or  $\acute{\grave{S}}$ ) or reflected rays ( $\grave{P}$  or  $\grave{S}$ ).

$$\dot{P}\dot{P} = D_1^{-1} \left[ \left( \frac{\beta_1}{\alpha_1} \right)^2 \sin 2i_1 \sin 2j_1 - \cos^2 2j_1 \right] \quad (\text{A.1})$$

$$\dot{P}\dot{S} = D_1^{-1} \left[ -2 \left( \frac{\beta_1}{\alpha_1} \right) \sin 2i_1 \cos 2j_1 \right] \quad (\text{A.2})$$

$$\dot{S}\dot{P} = D_1^{-1} \left[ \left( \frac{\beta_1}{\alpha_1} \right) \sin 4j_1 \right] \quad (\text{A.3})$$

$$\dot{S}\dot{S} = \dot{P}\dot{P} = D_1^{-1} \left[ \left( \frac{\beta_1}{\alpha_1} \right)^2 \sin 2i_1 \sin 2j_1 - \cos^2 2j_1 \right] \quad (\text{A.4})$$

## A.2 Solid-Solid Interfaces

From Aki and Richards [2002]:

### P-SV Waves

$$\begin{aligned} a &= \rho_2(1 - 2\beta_2^2 p^2) - \rho_1(1 - 2\beta_1^2 p^2), & b &= \rho_2(1 - 2\beta_2^2 p^2) + 2\rho_1\beta_1^2 p^2, \\ c &= \rho_1(1 - 2\beta_1^2 p^2) + 2\rho_2\beta_2^2 p^2, & d &= 2(\rho_2\beta_2^2 - \rho_1\beta_1^2), \end{aligned}$$

$$\begin{aligned} E &= b \frac{\cos i_1}{\alpha_1} + c \frac{\cos i_2}{\alpha_2}, \\ F &= b \frac{\cos j_1}{\beta_1} + c \frac{\cos j_2}{\beta_2}, \\ G &= a - d \frac{\cos i_1}{\alpha_1} \frac{\cos j_2}{\beta_2}, \\ H &= a - d \frac{\cos i_2}{\alpha_2} \frac{\cos j_1}{\beta_1}, \\ D &= EF + GH p^2 \end{aligned}$$

$$\dot{P}\dot{P} = \left[ \left( b \frac{\cos i_1}{\alpha_1} - c \frac{\cos i_2}{\alpha_2} \right) F - \left( a + d \frac{\cos i_1 \cos i_1}{\alpha_1 \beta_2} \right) H p^2 \right] / D \quad (\text{A.5})$$

$$\dot{P}\dot{S} = -2 \frac{\cos i_1}{\alpha_1} \left( ab + cd \frac{\cos i_2 \cos j_2}{\alpha_2 \beta_2} \right) p \alpha_1 / (\beta_1 D) \quad (\text{A.6})$$

$$\dot{P}\dot{P} = 2\rho_1 \frac{\cos i_1}{\alpha_1} F \alpha_1 / (\alpha_2 D) \quad (\text{A.7})$$

$$\dot{P}\dot{S} = 2\rho_1 \frac{\cos i_1}{\alpha_1} H p \alpha_1 / (\beta_2 D) \quad (\text{A.8})$$

$$\dot{S}\dot{P} = -2 \frac{\cos j_1}{\beta_1} \left( ab + cd \frac{\cos i_2 \cos j_2}{\alpha_2 \beta_2} \right) p \beta_1 / (\alpha_1 D) \quad (\text{A.9})$$

$$\dot{S}\dot{S} = \left[ \left( b \frac{\cos j_1}{\beta_1} - c \frac{\cos j_2}{\beta_2} \right) E - \left( a + d \frac{\cos i_2 \cos j_1}{\alpha_2 \beta_1} \right) G p^2 \right] / D \quad (\text{A.10})$$

$$\dot{S}\dot{P} = -2\rho_1 \frac{\cos j_1}{\beta_1} G p \beta_1 / (\alpha_2 D) \quad (\text{A.11})$$

$$\dot{S}\dot{S} = 2\rho_1 \frac{\cos j_1}{\beta_1} E \beta_1 / (\beta_2 D) \quad (\text{A.12})$$

### SH Waves

$$\Delta = \rho_1 \beta_1 \cos j_1 + \rho_2 \beta_2 \cos j_2$$

$$\dot{S}\dot{S} = \frac{\rho_1 \beta_1 \cos j_1 - \rho_2 \beta_2 \cos j_2}{\Delta} \quad (\text{A.13})$$

$$\dot{S}\dot{S} = \frac{2\rho_1 \beta_1 \cos j_1}{\Delta} \quad (\text{A.14})$$

## A.3 Solid-Liquid Interfaces

From Ben-Menahem and Singh [2000]:

$$D = \left( \frac{\beta}{\alpha} \right) \sin 2i_s \sin 2j_s \cos i_f + \epsilon \left( \frac{\alpha_f}{\alpha_s} \right) \cos i_s + \cos^2 2j_s \cos i_f$$

$$\epsilon = \frac{\rho_f}{\rho_s}$$

### Solid to Liquid Interface

$$\dot{P}\grave{P} = D^{-1} \left[ \left( \frac{\beta}{\alpha_s} \right)^2 \sin 2i_s \sin 2j_s \cos i_f + \epsilon \left( \frac{\alpha_f}{\alpha_s} \right) \cos i_s - \cos^2 2j_s \cos i_f \right] \quad (\text{A.15})$$

$$\dot{P}\grave{S} = D^{-1} \left[ -2 \left( \frac{\beta}{\alpha_s} \right) \sin 2i_s \cos 2j_s \cos 1_f \right] \quad (\text{A.16})$$

$$\dot{P}\grave{P} = D^{-1} [2 \cos i_s \cos 2j_f] \quad (\text{A.17})$$

$$\dot{S}\grave{P} = D^{-1} \left[ \left( \frac{\beta}{\alpha_s} \right) \sin 4j_s \cos i_f \right] \quad (\text{A.18})$$

$$\dot{S}\grave{S} = D^{-1} \left[ \left( \frac{\beta}{\alpha_s} \right)^2 \sin 2i_s \sin 2j_s \cos i_f - \epsilon \left( \frac{\alpha_f}{\alpha_s} \right) \cos i_s - \cos^2 2j_s \cos i_f \right] \quad (\text{A.19})$$

$$\dot{S}\grave{P} = D^{-1} \left[ -2 \left( \frac{\beta}{\alpha_s} \right) \cos i_s \sin 2j_s \cos i_f \right] \quad (\text{A.20})$$

### Liquid to Solid Interface

$$\dot{P}\grave{P} = D^{-1} \left[ \left( \frac{\beta}{\alpha_s} \right)^2 \sin 2i_s \sin 2j_s \cos i_f + \epsilon \left( \frac{\alpha_f}{\alpha_s} \right) \cos i_s - \cos^2 2j_s \cos i_f \right] \quad (\text{A.21})$$

$$\dot{P}\grave{P} = D^{-1} \left[ 2\epsilon \left( \frac{\alpha_f}{\alpha_s} \right) \cos 2j_s \cos i_f \right] \quad (\text{A.22})$$

$$\dot{P}\grave{S} = D^{-1} \left[ -4\epsilon \left( \frac{\alpha_f}{\alpha_s} \right) \cos i_s \sin j_s \cos i_f \right] \quad (\text{A.23})$$